DIPARTIMENTO
DI INGEGNERIA
DELL'INFORMAZIONE

UNIVERSITÀ
DEGLI STUDI
DI PADOVA

DIPARTIMENTO DI INGEGNERIA DELL'INFORMAZIONE
CORSO DI LAUREA IN BIOINGEGNERIA

'COLORECTAL CANCER AND GREEN TEA EXTRACT: EVALUATION OF TREATMENT EFFICACY USING *IN VITRO* AND *IN VIVO* IMAGING METHODS'

Supervisor:
MATTIA VERONESE

Co-supervisor:
ANA CRISTINA SANTOS

Candidate: BENEDETTA MARIN

ACADEMIC YEAR 2023-2024
16th April 2024

This work was developed in collaboration with:

Università degli Studi di Padova

Dipartimento di Ingegneria dell'Informazione

Universidade de Coimbra

Faculdade de Ciências e Tecnologia Universidade de Coimbra

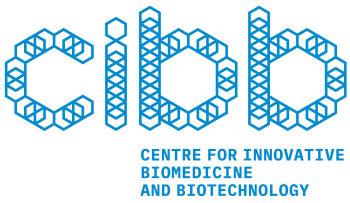

Centre for Innovative Biomedicine and Biotechnology

CHUC Centro Hospitalar e Universitário de Coimbra

CENIMAT Centro de Investigação de Materiais — i3N Instituto de Nanoestruturas, Nanomodelação e Nanofabricação

universidade de aveiro

RI.TE Radiation Imaging Technologies, LDA

Centro 2020 — Portugal 2020 — União Europeia Fundos Europeus Estruturais e de Investimento

All the experimental activities have been performed at Biophysics Institute-FMUC-iCBR-cibb, under the supervision of professor Ana Cristina Aguiar dos Santos.

A cup of tea
is always a good idea.

Abstract (EN)

This study explored the therapeutic potential of green tea extract (GTE) combined with chemotherapy for colorectal cancer (CRC) through both *in vitro* and *in vivo* experiments. Positron Emission Tomography (PET) imaging tailored to animal size with the innovative easyPET.3D technology was used to assess the *in vivo* effect of the tested treatments (chemotherapy protocols with and without GTE) on a non-orthotopic animal model throughout the experimental period.

The WiDr cell line was used for both *in vitro* and *in vivo* studies. Three chemotherapy protocols were tested: Cyclophosphamide (CFA) + 5-Fluorouracil (5-FU), Irinotecan (IRI), and the FOLFIRI regimen (5-FU + IRI + Leucovorin). *In vitro* studies assessed GTE's impact on cell viability across different concentrations of GTE powder (0.5-5-10 $\mu g/mL$) using the MTT assay. *In vivo* experiments involved ten animals divided into chemotherapy-only and GTE+chemotherapy groups, evaluating various parameters: tumour volume, body weight, and PET imaging with [^{18}F]-FDG as radiotracer. The tumour metabolic activity was quantified using the SUV_{mean} (mean Standard Uptake Value), calculated on manually drawn Regions of Interest (ROIs).

In vitro results showed slighted reduced cytotoxicity with GTE as compared to controls, with no statistical differences between the tested GTE powder concentrations. However, GTE did not interfere with drugs' efficacy, inducing cell death in over 50% of cases. Higher chemotherapy doses were less effective. *In vivo*, GTE+chemotherapy-treated animals showed longer survival and slower tumour growth, with the CFA + 5-FU (600 mg/m^2) protocol showing the poorest outcomes. Preliminary assessment of easyPET.3D spatial resolution indicated clear detection of 2 *mm* tumour details. Notably, only GTE-treated animals showed increased tumour volume corresponding to decreasing SUV_{mean}, suggesting a reduced tumour metabolic activity. Ongoing histopathological studies may help elucidating the tumour behaviour under these conditions, aiding in explaining the decrease in SUV*mean*.

Future research directions include further *in vitro* studies on cell cycle dynamics and increased sample sizes for more robust *in vivo* results. Additionally, improvements to the easyPET.3D system, such as coupling with Computed Tomography (CT) and integrating sensors to monitor heart rate, blood oxygen levels, and body temperature of the animals, could enhance imaging performance and image interpretation. Utilizing automatic segmentation methods to standardize SUV measurements is also suggested.

Overall, this study lays the groundwork for exploring the potential therapeutic benefits of combining GTE with conventional chemotherapy. Furthermore, it underscores the capabilities and potential for further development of innovative microPET technology in similar research studies.

Keywords: colorectal cancer, WiDr, green tea extract, chemotherapeutical agents, [^{18}F]-FDG, easyPET.3D

Abstract (IT)

Questo studio ha esplorato il potenziale terapeutico dell'estratto di tè verde (GTE) combinato con la chemioterapia contro il cancro del colon-retto (CRC) attraverso esperimenti sia *in vitro* che *in vivo*. In particolare, la tomografia ad emissione di positroni (PET), adattata alle dimensioni degli animali con la tecnologia innovativa easyPET.3D, è stata utilizzata, durante il periodo sperimentale, per valutare l'effetto dei trattamenti testati *in vivo* (protocolli chemioterapici con e senza GTE) su un modello animale non ortotopico.

La linea cellulare WiDr è stata scelta sia per gli studi *in vitro* che *in vivo*. Tre protocolli di chemioterapia sono stati testati: Ciclofosfamide (CFA) + 5-Fluorouracile (5-FU), Irinotecan (IRI), e il regime FOLFIRI (5-FU + IRI + Leucovorin). Gli studi *in vitro* hanno valutato l'impatto del GTE sulla vitalità cellulare attraverso diverse concentrazioni di polvere di GTE (0.5-5-10 $\mu g/mL$) utilizzando il test MTT. Gli esperimenti *in vivo* hanno coinvolto dieci animali divisi in due gruppi: sola chemioterapia e GTE + chemioterapia. Sono stati valutati vari parametri: volume del tumore, peso corporeo dell'animale e imaging PET con [^{18}F]-FDG come radiotracciante. L'attività metabolica del tumore è stata quantificata utilizzando il SUV_{mean} (Standard Uptake Value medio), calcolato su Regioni di Interesse (ROIs) segmentate manualmente.

I risultati *in vitro* hanno mostrato un leggero calo della citotossicità con il GTE rispetto al controllo, senza differenze statisticamente significative tra le diverse concentrazioni di polvere di GTE testate. Tuttavia, il GTE non ha interferito con l'efficacia dei farmaci, inducendo la morte cellulare in più del 50% dei casi. Le dosi più elevate di chemioterapia hanno portato i risultati peggiori. *In vivo*, gli animali trattati con GTE+chemioterapia hanno mostrato una sopravvivenza più lunga e una crescita del tumore più lenta, con il protocollo CFA+5-FU (600 mg/m^2) che ha mostrato i risultati più scadenti. Una valutazione preliminare della risoluzione spaziale di easyPET.3D ha indicato una chiara rilevazione di dettagli tumorali di 2 *mm*. Inaspettatamente, solo gli animali trattati con GTE hanno mostrato un aumento del volume del tumore corrispondente a un SUV_{mean} in diminuzione, suggerendo una ridotta attività metabolica della massa maligna. Studi istopatologici in corso potrebbero aiutare a chiarire il comportamento del tumore in queste condizioni, aiutando a spiegare la diminuzione del SUV*mean*.

Futuri sviluppi di questa ricerca includono ulteriori studi *in vitro* sulla dinamica del ciclo cellulare e dimensioni di campione maggiori per risultati *in vivo* più robusti. Inoltre, miglioramenti al sistema easyPET.3D, come l'accoppiamento con la Tomografia Computerizzata (CT) e l'integrazione di sensori per monitorare la frequenza cardiaca, i livelli di ossigeno nel sangue e la temperatura corporea degli animali, potrebbero migliorare le prestazioni dell'imaging e l'interpretazione delle immagini stesse. In ultimo, è suggerito l'utilizzo di metodi automatici di segmentazione dei tumori per standardizzare le misurazioni del SUV.

In generale, questo studio pone le fondamenta per esplorare i potenziali benefici terapeutici della combinazione di GTE con agenti chemioterapici convenzionali. Inoltre, sottolinea le capacità e il potenziale innovativo per ulteriori sviluppi della tecnologia microPET in studi di ricerca simili.

Parole chiave: cancro del colon-retto, WiDr, estratto di tè verde, agenti chemioterapici, [^{18}F]-FDG, easyPET.3D

Acronyms and abbreviations

%STD percentage standard deviation

^{18}F Fluorine-18

5-FU 5-Fluorouracil

ALARA As Low As Reasonably Achievable

ANOVA one-way analysis of variance

APC adenomatous polyposis coli

ATTC® American Type Culture Collection®

BSA body surface area

CDX cell line-derived xenograft

CFA Cyclophosphamide

CI confidence interval

CIMP CpG Island Methylator Phenotype

CIN chromosomal instability

CPOM contrast phase optical microscope

CRC colorectal cancer

CT Computed Tomography

DHFU dihydrofluorouracil

DMEM Dulbecco's Modified Eagle Medium

DMSO dimethyl sulfoxide

DPD dihydropyrimidine dehydrogenase

ECICC European Commission Initiative on Colorectal Cancer

ECIS European Cancer Information System

EGCG epigallocatechin-3-gallate

EMEM Eagle's Minimum Essential Medium

EMT epithelial mesenchymal transition

FAP familial adenomatous polyposis

FBS foetal bovine serum

[^{18}F]-FDG [^{18}F]-FDG fluorodeoxyglucose

FdUMP 5-fluoro-2'-deoxyuridine-5'-monophosphate

FdUTP 5-fluoro-2'-deoxyuridine-5'-triphosphate

FOLFIRI 5-Fluorouracil + Irinotecan + Leucovorin

FoV field-of-view

FUTP 5-fluorouridine-5'-triphosphate

GPU graphics processing unit

GT green tea

GTE green tea extract

GTE po green tea extract powder

HNPCC hereditary nonpolyposis colorectal cancer

HPLC High Performance Liquid Chromatography

HR hazard ratio

i.p. intraperitoneal

IBD inflammatory bowel disease

iCBR Institute of Clinical and Biomedical Research

IDO indoleamine 2,3-dioxygenase

IQ Image Quality

IRI Irinotecan

KRAS Kirsten rat sarcoma viral oncogene homolog

LM list-mode

LM-MLEM list-mode maximum-likelihood expectation-maximization

LoR line of response

LV Leucovorin

LYSO lutetium-yttrium oxyorthosilicate

MDR multidrugresistance

MLEM maximum-likelihood expectation-maximization

MSI microsatellite instability

MTT 3-(4, 5-dimethylthiazolyl-2)-2, 5-diphenyltetrazolium bromide

NEMA National Electrical Manufacturers Association

NMDA N-methyl D-aspartic acid

o.g. oral gavage

OD optical density

PBS phosphate-buffered saline

Pen/Strep penicillin/streptomycin

PET Positron Emission Tomography

PM phosphoramide mustard

PM$_{prot}$ protonated phosphoramide mustard

PMMA polymethylmethacrylate

RC recovery coefficient

ROI region of interest

ROS reactive oxygen species

rpm rotations per minute

RR risk ratio

s.c. subcutaneous

SiPM silicon photomultiplier

SN-38 7-ethyl-10-hydroxy-camptothecin

SN-38G SN-38 glucuronide

SOR spill-over ratio

SUV standard uptake value

SUV$_{max}$ maximum standard uptake value

SUV$_{mean}$ mean standard uptake value

TP53 tumour protein p53

TS thymidylate synthase

VEGF vascular endothelial growth factor

VEGFR vascular endothelial growth factor receptors

VoI volume of interest

List of Figures

List of Tables

Contents

1 Introduction

1.1. Contextualization

Cancer is often referred as the "Pathology of the century" [1]: the Global Cancer Observatory estimates that in 2022, the worldwide number of deaths caused by this malignancy was 9,743,832 [2]. Nowadays, cancer is one of the deadliest diseases in human history, with an extremely poor prognosis [3]. Fake news led to the diffusion of several false myths about cancer and about its traditional treatments too (i.e. surgical resection, chemotherapy, radiotherapy and immunotherapy). For instance, some are convinced that conventional anticancer therapies are even more dangerous than the illness itself: many patients are scared of the side effects caused by chemotherapy. Consequently, these patients who are reluctant towards conventional cancer treatments may decide to replace them by alternative medicine, showing a favourable attitude towards natural products rather than synthetic ones [4]. This phenomenon addressed as 'natural preference' is becoming a new sort of health "epidemic": there are patients who try using plants and natural compounds to achieve a cure that oncologists have not discovered yet [5]. Unfortunately, avoiding conventional medicine and using only natural methods is not the best treatment option in oncology: an observational study showed that the use of alternative medicine compared to conventional treatments, is associated to a higher risk of death (hazard ratio (HR) = 2.50, 95% confidence interval (CI) = 1.88 to 3.27) [6]. Literature evidence suggests that natural and traditional medicine should not be enemies, but accomplices; hence, the best option could be their synergistic use. In fact, conventional medicine and the use of natural compounds are not mutually exclusive: more than 60% of the currently used drugs are of plant origin. Nevertheless there is more: it is well known that substances gifted by nature and, in particular, pythochemicals (i.e. biologically active chemical compounds produced by plants) have been used in medical therapies since ancient history [7]. Lately, novel biology gained a deeper awareness of mechanisms and targets involved in the disease process, and most anticancer drugs used today thanks to natural products. In addition, some chemotherapeutic agents (*e.g.* taxanes) have a herbal origin [8].

1.1.1. Colorectal Cancer

One of the most diagnosed cancers worldwide is colorectal cancer (CRC), which affects the digestive tract and, in particular, the large intestine. Since it is a common malignancy, routine CRC screening is strongly suggested for people with average risk[1] starting at age 45 [10]. Colorectal cancer is a complex, heterogeneous and multistep disease, more spread among males. It can arise through three molecular pathways: the chromosomal instability (CIN), the microsatellite instability (MSI), and the CpG Island Methylator Phenotype (CIMP). These pathways are not mutually exclusive, with some tumors exhibiting features of multiple pathways [11]. The most common one is called 'adenoma-carcinoma sequence' [12] and will be described in subsection 2.1.2 . Chemotherapy is still the backbone treatment for this disease, however it entails several drawbacks, which will be explored in subsection 2.2.1.

1.1.2. Green Tea as a possible therapy for CRC

Natural compounds can be viewed as an aid for chemotherapy: in particular, Green Tea (GT) is being studied in many trials, since there is evidence showing its adjuvant role towards CRC [13]. GT is the most popular beverage in the world after water [14]. It is produced and extracted from the leaves of *Camelia sinensis* (**Figure 1.1**), a plant native to Southeast Asia, East Asia, and the Indian subcontinent [15]. Previous studies showed the pleiotropic effects of green tea towards cancer in general: it is both chemopreventive, i.e. it abrogates or delays the onset of the malignancy, and chemotherapeutical, i.e. it helps to eliminate cancer after its onset [16]. The benefits of this beverage have been primarily attributed to its polyphenolic content [14].

Figure 1.1: Leaves of *Camelia sinensis*, from which green tea is extracted (retrieved from [17]).

1.1.3. CRC study models

Several models can be used to study CRC, each offering unique advantages as no single model perfectly replicates human CRC. Researchers strategically use a combination of models to gain a comprehensive understanding of CRC. There are two main categories.

[1]Average risk is considered in absence of: a personal history of CRC or certain types of polyps, a family history of CRC, a personal history of inflammatory bowel disease, a confirmed or suspected hereditary colorectal cancer syndrome, personal history of getting radiation to the abdomen or pelvic area to treat a prior cancer [9].

- Cell lines (*in vitro* models): established and readily available human CRC cell lines offer easy access and genetic control, allowing researchers to examine specific aspects of the disease, such as gene mutations and drug responses.
- animal models (*in vivo*) provide a more complex environment, being a closer representation but more expensive and time-consuming. Researchers strategically use a combination of models to gain a comprehensive understanding of CRC.

The WiDr cell line is readily available from cell line repositories, making it a convenient choice for researchers. WiDr cells have been used for decades in CRC research, hence there is a wealth of data and established protocols for using them. WiDr cells are known to be aggressive: this can be useful for studying certain aspects of this disease, like metastasis [18, 19].

1.2. Study aim

This investigation will avail the role of green tea in an adjuvant therapy regimen, trying to reduce CRC tumours or even fight them. The tested therapeutic approach consisted in combining an enriched GT extract in powder form (Green Tea Extract Powder = GTE po) with conventional chemodrugs used in the clinics against CRC. In other words, the 'natural product chemotherapy combination therapy' was elicited in order to obtain a cooperative action. If successful, this might help reducing the dose/number of chemotherapy cycles, hence the side effects of anti-cancer drugs in CRC treatment [7]. The experimentation involved *in vitro* procedures, with the following main goals:

- to evaluate the cytotoxicity of a GTE to WiDr cells (a CRC cell line); therefore, the possibility of reducing the therapeutic agents' dose was examined;
- to determine the best concentrations of GTE po both in a monotherapy regimen and in a combination regimen [18].

Furthermore, the same assessment was transposed *in vivo*, using an appropriate animal model. Immunocompromised BALB/c male mice were injected with WiDr cells to achieve a non-orthotopic induction of CRC. This xenograft was used to monitor the tumour evolution and avail the treatment efficacy [20].
Cancer development imaging monitoring was performed using the easyPET.3D system, a novel and experimental PET system, specifically designed for small-sized animals [21]. Moreover, easyPET.3D imaging technology enables an early oncological diagnosis and, therefore, an early implementation of the chosen therapeutic regimen. The *in vivo* experimentation involved the acquisition, reconstruction, processing, and quantification of PET data, together with an external external evaluation (measuerement) of the tumour dimension (as soon as the tumour became visible to the naked eye). To sum up, the achievement of reduced cytotoxic effects and assessment of the relevance of an early diagnosis were performed. Herein, the immediate effect of this study would be on an improvement of patient's quality of life. As a final remark, a

sterile environment, standardized conditions and the respect of well-defined protocols, were the common denominators of all *in vitro* and *in vivo* experiments. These conditions were crucial for two reasons: first they allowed to have more control over external factors; second, a direct consequence was a decrease in the number of individuals needed during *in vivo* studies, therefore respecting the 3R's principle[2], being also more time/cost/resource effective.

1.3. Work structure

This work is organised into five chapters.

Chapter 1: Introduction - this chapter contextualizes the present study and enumerates its main goals. It briefly describes the main concepts addressed during the work and the structure of the experimental design.

Chapter 2: Literature review - this chapter summarizes the results of previously published works on the main topic, and is divided into three sections. The first section is an introduction to the digestive tract structure, followed by an insight into colorectal cancer, its key features, and its main risk factors. The second section briefly takes into consideration the main existing clinical approaches used to treat this malignancy, with a deeper insight into chemotherapy and its side effects. Lastly, the third section begins with a short description of how natural compounds can interplay with chemotherapy, focusing on green tea extracts (GTE) and its main actions towards CRC.

Chapter 3: In vitro studies - This chapter starts with an insight into the tools and protocols used during *in vitro* experimentations: from the description of the cell line, passing through cell culture elements and the description of each manipulation step, until the cell plating. The mechanisms of action of the tested chemotherapeutical agents will be delineated as well. The third and last section will show and discuss the results obtained after the statistical analysis of data.

Chapter 4: In vivo studies - After a brief introduction to the objective of this chapter, the second section presents the whole setting adopted to carry out *in vivo* experimental studies. Then, this chapter will provide a deeper insight into *easyPET.3D*, the imaging system which was used for the assessment of tumour dimensions and activity. Its functioning and calibration will be part of the description. Finally, the last section will show and reason about the results of the tumour monitoring performed on the mice.

Chapter 5: Conclusions and future directions - This chapter summarizes the results of the present work, drawing pertaining conclusions. The main limitations and pitfalls of each step of

[2]The 3Rs (Replacement, Reduction, Refinement), developed by Russell and Burch, are the cornerstone of ethical animal research worldwide, promoting animal welfare [22].

the study (both *in vitro* and *in vivo* models) are also mentioned. The sum of all this information is then used to provide new perspectives and suggestions for future work and analysis, aiming to achieve a deeper understanding of the main topic under discussion.

2 Literature review

2.1. Colorectal cancer

2.1.1. The digestive tract anatomy

The human digestive system is a long, twisting tube called the GI tract. It is made up of hollow organs (like the mouth, esophagus, stomach, and intestines), and aided by solid organs like the liver, pancreas, and gallbladder. The small and large intestines, comprising the majority of the GI tract, specialize in nutrient absorption and waste removal. The small intestine, with its three sections (duodenum, jejunum, and ileum), absorbs most nutrients from food. The large intestine focuses on water absorption and waste elimination. The colon is an U-shaped tube made of muscles and it is the longest part of the large intestine. It is further divided into sections that include the *c*ecum, ascending colon, transverse colon, descending colon, sigmoid, and *rectum*, which is the final segment [23] (**Figure 2.1**). The limit separating the last two subunits (sigmoid and *rectum*) is named 'rectosigmoid junction'. Histologically, colon and *rectum* show a layered structure. The four main layers (from the innermost to the outermost) are: mucosa, submucosa, *muscularis*, and serosa/*adventitia* [3].

2.1.2. Colorectal cancer key features

The term "colorectal cancer" (CRC) addresses both cancers of the colon, cancers of the rectosigmoid junction, and cancers of the *rectum*. They are grouped together firstly as the malignancy often affects all of them, and second because they have many common features such as some clinical symptoms. The typical symptoms of CRC are: rectal bleeding, microcytic anaemia, altered bowel habits, and chronic abdominal pain. The majority of CRC cases are cancers of the colon (approximately 67%), whereas cancers of the rectosigmoid junction and the rectum cover the remaining 33.3% [24].

The benign precursor lesion, from which most CRC start, are polyps, *i.e.* abnormal clumps of cells on the *epithelium* (the inner lining of the mucosa) that protrude into the lumen. Generally, CRC development follows the 'adenoma-carcinoma sequence', which can be described through four subsequent phases [12].

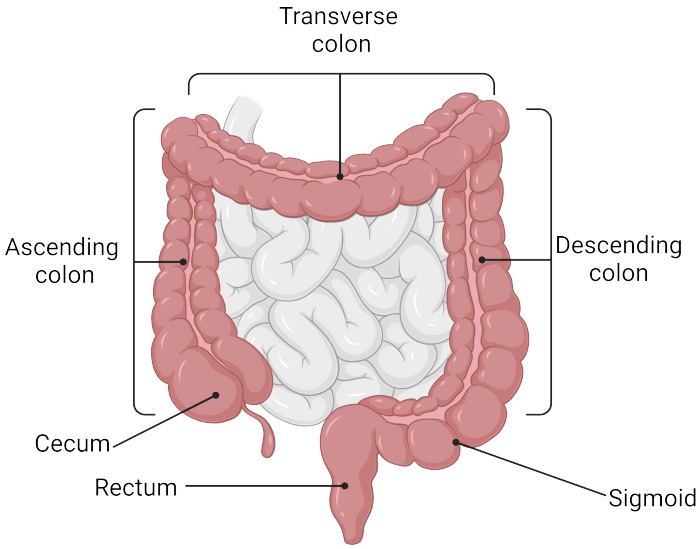

Figure 2.1: Anatomy of the large intestine (created with BioRender.com).

1. **Initiation**: colonic or rectal epithelial cells undergo irreversible genetic and epigenetic damage that accumulate over time. This predisposes their subsequent abnormal growth. Mutations in this phase include the inactivation of the antioncogene adenomatous polyposis coli (APC) that drives uncontrolled cell divisions [25].

2. **Promotion**: the initiated cells start to divide without control, leading to the formation of adenomatous polyps that may proliferate and grow. Herein, the responsible of the accelerated cells division is the Kirsten rat sarcoma viral oncogene homolog (KRAS) hyperactivity [25].

3. **Progression**: further genetic and epigenetic mutations affect aberrant cells, giving them a selective growth advantage; final genetic events involve the suppression of tumour protein p53 (TP53) gene, which causes the inactivation of *p53*, a tumour suppressor protein whose role is important in cell apoptosis regulation [25]. Thus, benign tumour cells may become malignant, acquiring the characteristic aggressive pattern and the potential to metastasize.

4. **Metastasis**: through abnormal proliferation, polyps can invade the bowel wall and the nearby tissues; and even spread to distant parts of the body through the circulatory and lymphatic systems [26]. This occurs because cells lose their epithelial characteristics (polarity and specialized cellular contacts) and acquire a different morphology with a migratory behaviour. This process is called epithelial mesenchymal transition (EMT) [3]. CRC most commonly metastasizes to the liver, then to the lung and bone [27].

However, not all polyps evolve into invasive cancers: some of them may remain benign. The main precursors to most CRCs are two subtypes of polyps: adenomatous polyps (adenomas) and serrated polyps. Most CRCs are called adenocarcinomas because they evolve from adenomas (85-90%), whereas the remaining 10-15% of sporadic CRCs have serrated polyps as precursors [28]. A schematic representation of the fate of an adenomatous polyp and its cellular detail is shown in **Figure 2.2**, depicting the estimated survival rate for each phase.

At a cellular level, the CRC tumour microenvironment is composed of three main cell types with which it closely interacts: cancer-associated fibroblasts, vascular cells and infiltrating immune cells [29]. Another fuel of cancer growth, metastasis, and resistance to therapy in CRC are stem cells [30]. All these players interact in a reciprocal way, making the landscape of CRC extremely complex and mutational.

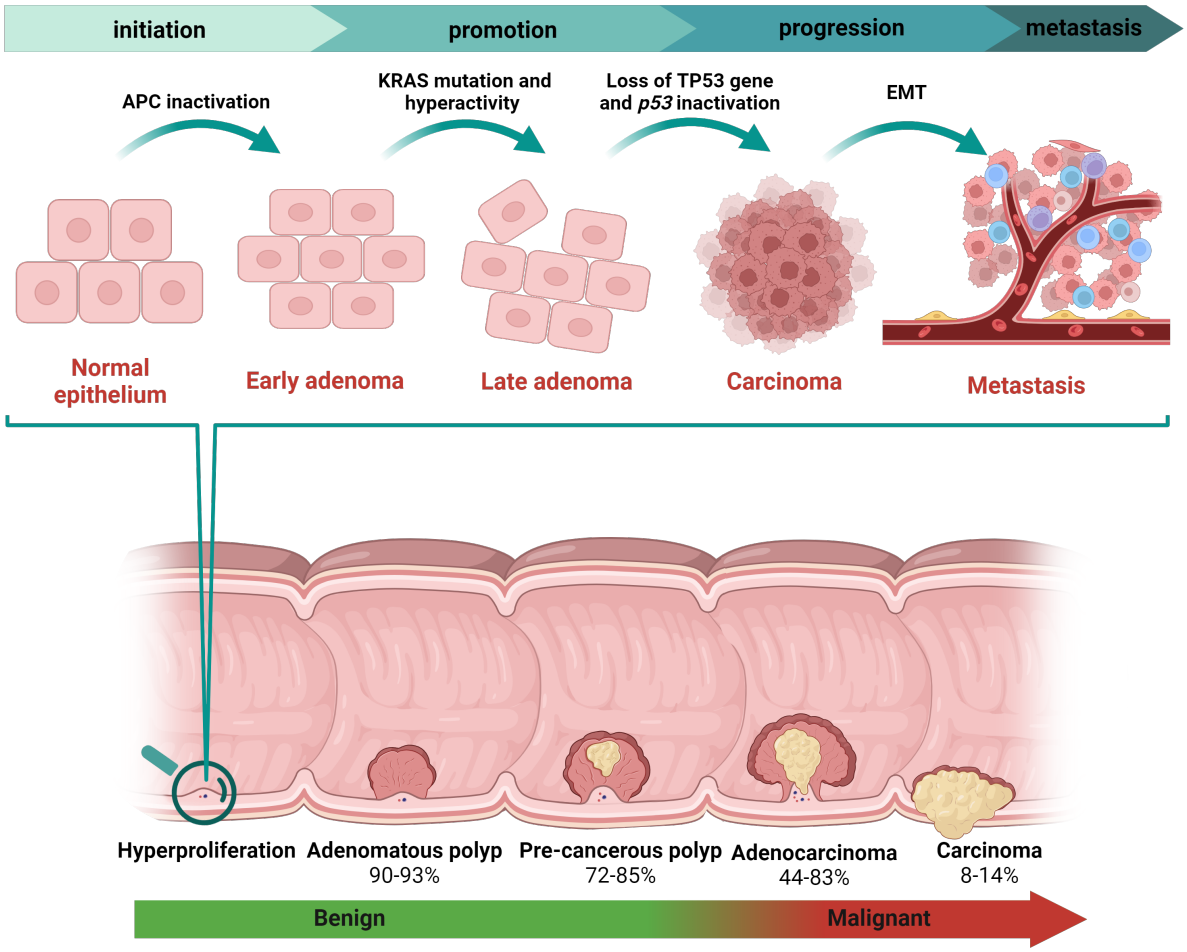

Figure 2.2: The different stages of CRC and the relative survival rates in percentage (adapted from [26, 10]) (created with BioRender.com).

The diagnosis of each cancer is classified by a stage according to its development and how far it has spread. In particular, each stage is described by a code to represent the extent of the disease: it consists of a roman number (from zero to IV) and a letter [31]. A higher number indicates a worse prognosis. If a cancer is assigned stage 0, it means that aberrant cells are only in the mucosa layer, whereas at stage IV, the worst, cancer has already metastasized [3].

2.1.3. Risk factors for CRC

A risk factor is something that increases the chance of developing a disease; the incidence of CRC is related both with non-modifiable risk factors and modifiable risk factors [32]. Nonmodifiable risk factors include age and genetic inheritance from progenitors (*e.g.* specific disease-associated

mutations and family history). On the other hand, modifiable risk factors represent environmental and lifestyle conditions [33].

2.1.3.1. Non-modifiable risk factors

The patient's age is assumed to be the major cause for risk of colorectal cancer. In fact, as age increases, the risk of developing this disease also increases: 9 out of 10 people who develop CRC are older than 50 years. 70 years old is the age corresponding to the incidence peak of this pathology.
Past-inflammatory diseases, chronic inflammatory bowel disease (IBD) like Crohn's disease and ulcerative colitis are un-modifiable risk factors for CRC, with Crohn's disease increasing the risk by 20-fold and ulcerative colitis by 3-fold [34].
Furthermore, people with a family history of certain cancers or genetic risk factors (hereditary cancer syndromes) are significantly more prone to develop the disease over their lifetime [12]. Regarding the medical family history, a meta-analysis of observational studies concluded that individuals with at least one affected first-degree relative (i.e. parents, siblings, or children) had CRC risk increase by 2.24 times (95% CI 2.06–2.43) [35]. The two most common hereditary syndromes causing predisposition to CRC are:

- hereditary nonpolyposis colorectal cancer (HNPCC), which grows predominantly in the first three segments of the colon;
- familial adenomatous polyposis (FAP), which usually grows in the descending colon or in the sigmoid.

Surprisingly, these mutations are characterised by low penetrance, which means that the likelihood that CRC phenotype will occur when a particular genetic mutation is present is low [36]. Consequently, many colon cancers are due to acquired instead of inherited mutations. This fact emphasizes the importance of environmental risk factors in the modulation of the disease risk [12].

2.1.3.2. Modifiable risk factors

Alcohol consumption, smoking, sedentary lifestyle, and counselling on healthy lifestyle are very important. Lifestyle features were mentioned in the European Commission Initiative on Colorectal Cancer (ECICC) guidelines for primary prevention published in 2023.
First, the ECICC minimising alcohol drinking. Evidence supporting this guideline was a systematic review which results include three categories of alcohol intake and its relation to CRC risk [37]. This dose-risk analysis estimated risk ratios (RRs) of 1.82 (95% CI 1.41-2.35), 1.38 (95% CI 1.28-1.50) and 1.07 (95% CI 1.04-1.10) for 100, 50 and 10 g of alcohol/day, respectively [37].
A second strongly recommended behaviour is avoiding or quitting smoking, whatever type of nicotine delivering cigarettes. A systematic review (including a total of 2,247,122 participants) estimated the population risk for both current and former smokers *versus* never smokers. The

pooled RR for former versus never smokers was 1.18 (95% CI 1.14-1.23), whereas the RR for current versus never smokers was 1.20 (95% CI 1.11-1.30) [38].
Third, there is an inverse association between a healthy lifestyle with regular physical activity and CRC risk. Notably, a systematic review provided the HR of colorectal cancer for high and moderate levels of cardiorespiratory fitness: the obtained values were, in the aforementioned order, 0.77 (95% CI 0.62-0.92) and 0.74 (95% CI 0.55-0.93) [39].
Looking at these results, the ECICC strongly encourages lifestyle counselling for individuals in order to increase the awareness on the risks associated to daily bad habits. To sum up:

- alcohol consumption and smoking are recognized risk factors of adenoma, CRC and its recurrence;
- increased physical activity is a recognized protective factor of adenoma, CRC and its recurrence.

Risk factors that emerged from further studies are: obesity and the Western dietary pattern rich in processed and red meat. On the contrary, an additional preventive factor is a prudent dietary pattern rich in fibers and whole grain [12].

2.1.4. Epidemiology

The World Health Organisation's data show that CRC is not only the third most common malignant tumour, but also the second most fatal cancer worldwide [40]. According to the European Cancer Information System (ECIS)'s statistics, the estimated incidence and mortality rates in 2022 were higher for males than females: 92.7 (males) *versus* 58.2 (females) for incidence (**Figure 2.3**) and 98.7 (males) versus 42.8 (females) for mortality. Hence, men are clearly more prone to colorectal cancer. For many years lifestyle has been considered responsible for this bias: for instance, smoking and alcohol consumption are more observed in men's routine. A study published in June 2023, in Nature, revolutionized this belief, showing that there is much more to it than bad habits: chromosome Y can be the most reliable explanation for the higher frequency of CRC in men [41]. In fact, it was found that a particular Y-chromosome gene in mice raises the risk of metastasis of some CRCs.

2.2. Currently available therapeutic approaches for CRC

Given the aim of the present work, this section will take into consideration only the main and conventional treatment methodologies for the studied malignancy. Novel therapies are currently being evaluated in clinical trials and some of them have already entered the clinical scenario [42].
The choice of the most appropriate treatment for each patient relies on several factors such as the stage assigned to the disease, possible collateral effects, age, sex, and comorbidities. Hence, treatments are usually not used in an isolated way, but can be combined with each other; they can be administered either simultaneously or sequentially in order to increase their efficacy.
Each treatment approach can be classified as local, systemic or a mixture between the two [3].

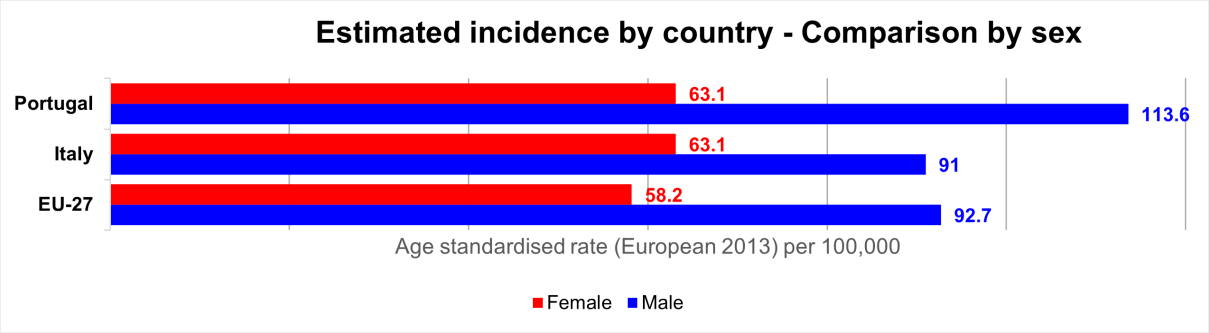

Figure 2.3: Estimated age-standardized incidence rates of CRC in 2022. Data of Portugal, Italy and European Union are displayed. Men (in blue) show higher incidence rates than age-matched women (in red). Incidence represents the number of new cases arising in a given period in a specific population. (This information was collected by cancer registries. Data from *ECIS prevalence estimates page*. `https://ecis.jrc.ec.europa.eu/`)

Local treatments are suitable for earlier-stage cancers, since they address only the tumour and the area close to it without affecting the rest of the body. The most common local treatments suggested for CRC are surgical procedures and post-operative radiotherapy. On the other hand, systemic treatments are so named because they reach cancer cells travelling via the circulatory system. They can be further classified as:

- neoadjuvants (before surgery), whose goal is the reduction/elimination of the cancer and the limitation of further tumour growth;
- adjuvants (post-surgery), whose goals are killing any remaining cancer cell and minimise the chances of recurrence [43].

A brief description of the mentioned treatment options and their hurdles is given in **Table 2.1**.

2.2.1. Chemotherapy: an overview

Nowadays chemotherapy is a well-established treatment, and it is the primary option against metastatic CRC [45]. As reported in **Table 2.1**, its main goal is the inhibition of cellular proliferation and, consequently, the avoidance of the tumour growth and metastasis [46]. The principle shared by chemotherapeutic agents is cytotoxicity, meaning that they interfere with several phases of the cellular cycle and the process of mitosis. The rationale for this application is that cancer cells are more susceptible to these agents since they generally have a faster division rate [47].

Current chemotherapy includes both monotherapy (also called single-agent therapy), which delivers only one chemotherapeutical agent, and combination regimens (also called multiple-agent) delivering chemotherapeutical cocktails [3].

Chemotherapeutic agents can be classified according to their specific mechanism of action. The five main classes are: alkylating agents, antimetabolites, antibiotics, microtubule targeting agents and topoisomerases inhibitors [48]. **Table 2.2** displays a summary of the characteristics of each aforesaid group.

Table 2.1: Available most diffused conventional treatments for CRC (adapted from [31, 42, 44]).

TREATMENT	DESCRIPTION	MAIN DRAWBACKS
Surgical resection	Adapted to well-defined tumours. It involves the excision of part of the colon or the *rectum* and, eventually, of nearby limph nodes.	Pain, constipation, diarrhea, risk of death (due to metastasis and mechanical disruption of tumour integrity).
Radiation therapy	Use of ionizing radiations to bombard and destroy cancer cells.	Side effects (both short and long-term) due to the toxicity of radiations delivered not only to cancer cells, but also to healthy tissues.
Immunotherapy	Use and potentiation of body's autoimmune system: it enhances T-cell activation, increasing the cytotoxic death of cancer cells.	High cost, severe side effects, and eventual short-term efficacy.
Targeted therapy	Use of monoclonal antibodies to target defined genes of tumour cells or defined tissue environment that determines cell proliferation and migration. It stops the cancer diffusion, and, at the same, time it limits damage to healthy cells.	Side effects: rash on the upper body and face.
Chemotherapy	Use of drugs to destroy cancer cells. Its primary aim is stopping the ability of cancer cells to grow and divide.	Side effects due to systemic toxicity, possible multidrug resistance of cancer cells, low tumour-specific selectivity.

2.2.1.1. Chemotherapy disadvantages

The use of chemodrugs brings several hurdles.

First, their administration causes side effects, which are a consequence of their mechanisms of action. Their cytotoxicity, which addresses DNA and proteins expression, is not limited to cancer cells only, but affects normal cells as well, resulting in serious haematological toxicities and damages of the involved tissues [46]. This leads to collateral effects on patients which become a weakening and often observed clinical obstacle in cancer management. In fact, all these symptoms can interfere with a continuous treatment, thus limiting its benefits [50]. Most recurrent side effects reported in literature are: nausea, vomiting and fatigue, decreased appetite, taste alterations, alopecia, damage of oral mucosa, constipation, diarrhoea, numbness or tingling of the hands and/or the feet, skin alterations, fever and flu-like symptoms, allergic reactions, and many others. Moreover, immunosuppression caused by chemodrugs increases the risk of infections.

Another relevant undesirable phenomenon associated with chemotherapy is the appearance of multidrugresistance (MDR), responsible for the death of most patients undergoing this treatment [51]. Cancer is a multifactorial disease involving the alteration of many different pathways: conventional chemodrugs can target only one or few pathways. Hence, higher doses of pharmaceuticals must be delivered; unfortunately, cancer cells are able to adapt to a given drug treatment, and the higher doses help eliciting the establishment of survival alternative pathways which can lead to drug resistance [52].

Hence, it is important to find new solutions in order to relieve chemotherapy-induced effects,

Table 2.2: Classification of chemotherapeutical agents based on their mechanism of action. For each class, examples of drugs for colorectal cancer used in clinical practice are reported. Emphasised chemodrugs are the ones which will be used in the present work. Adapted from [46, 49].

CLASS NAME	MECHANISM OF ACTION	EXAMPLES FOR COLORECTAL CANCER
Alkylating Agents	They yield an unstable alkyl group, R-CH_2^+ which reacts with nucleophilic centers on proteins and nucleic acids. Alkylation of DNA guanine can lead to cell death or apoptosis, resulting from an inability to repair the damage.	**cyclophosphamide**, carboplatin, oxaliplatin
Antimetabolites	They inhibit the synthesis of nucleic acids. They can either blend into nucleic acids or block enzymes needed for DNA and RNA synthesis. Thus, they encourage cells death.	**5-fluorouracil**
Antibiotics	They kill cancer cells by acting on the DNA via four main mechanisms. One of them is the intercalation between bases to inhibit DNA and RNA synthesis.	mitomycin
Microtubule targeting agents	They obstruct mitotic progression and cytoskeletal dynamics.	vincristine
Topoisomerases inhibitors	They obstacle the replication and trascription and, thus, cell division by preventing the unwinding of DNA.	**irinotecan**

improve patients' well-being and prevent chemoresistance. A solving strategy could be the 'combination of natural product therapy with chemotherapy' (see **section 1.2**, page 3).

2.3. Natural substances as anticancer agents

The importance of a healthy diet emerged from the analysis of preventive factors (see **subsection 2.1.3**, page 9). In this context, various dietary agents and natural compounds have been evaluated for their anti-cancer actions. These products can be viewed as a powerful support for chemotherapy: conventional chemotherapeutic drugs address only one specific target (such as nucleic acids, particular proteins, or tumorigenic pathways), whereas natural products typically could act within multiple pathways (including cell proliferation, agiogenesis, metastasis and apopstosis) [52]. There are three main mechanisms through which natural compounds, if coupled with chemotherapy, can cooperate:

1. mitigation of toxicity associated with conventional chemodrugs;
2. reduction of chemoresistance, through the increase of chemodrug within malignant cells and the minimisation of drug efflux;
3. direct intensification of the anticancer potential through the chemosensitization of tumour cells, thus becoming more responsive to standard agents [52].

All these beneficial actions can allow to lower dosages, achieving the same efficacy and, in some

cases, even better pharmacological results. A positive consequence, as already mentioned, of a reduced dose is a concomitant minimization of adverse events [52].

2.3.1. Green Tea

This section will focus on the chemotherapeutical action of Green Tea as an extract (GTE) when coupled with conventional chemodrugs in a combinatory regimen in order to fight CRC. This beverage contains many polyphenolic compounds, which represent 30% of the dry weight of green tea leaves. Most of the polyphenols in GT are flavanols, a subgroup of polyphenols, commonly known as catechins [53]. Until now, 8 different catechins have been extracted from GT; among them, the most abundant are epigallocatechin-3-gallate (EGCG), epigallocatechin, and epicatechin-3-gallate epicatechin (EC) [54] (**Figure 2.4**).

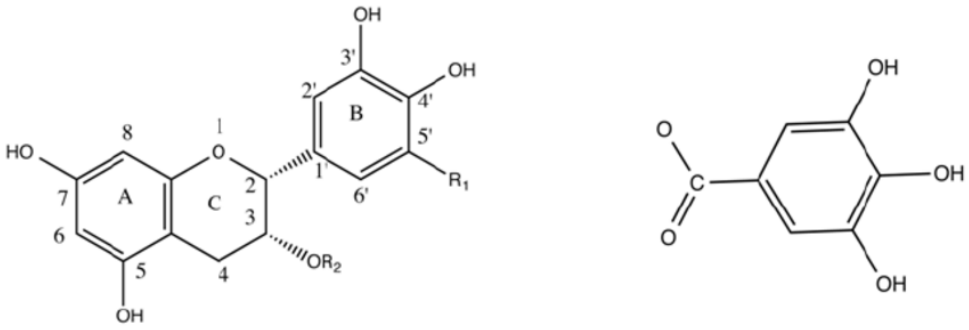

	R1	R2
EC	H	H
EGC	OH	H
ECG	H	Gallate group
EGCG	OH	Gallate group

Figure 2.4: Chemical formula of the major GTE catechins. Their chemical structure shows two aromatic rings (A and B) and a dihydropyran heterocyclic ring (C) (adapted from [55]).

EGCG: chemical composition and molecular structure

EGCG is the predominant catechin found in GT and it is the most effective one [56]. The chemical structure of this catechin is showed in Figure 2.5.

EGCG *[(2R,3R)-5,7-dihydroxy-2-(3,4,5-trihydroxyphenyl)-3,4-dihydro-2H-chromen-3-yl 3,4,5-trihydroxybenzoate]* is a phenolic antioxidant with the molecular formula $C_{22}H_{18}O_{11}$. Its molecular weight is 458.375 g/mol, and its melting point is 140-142° C [56].

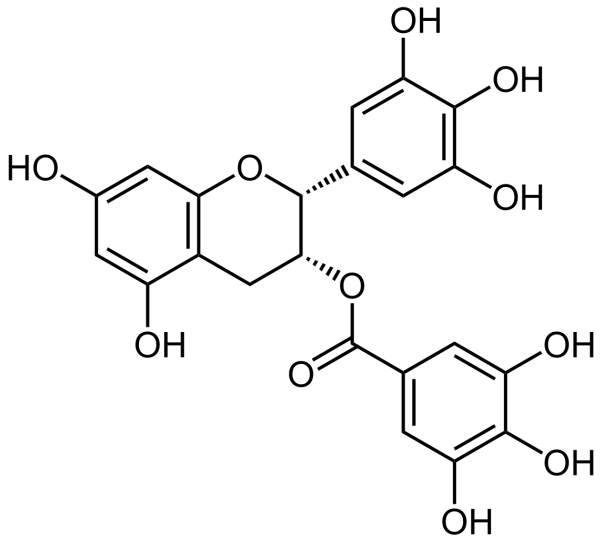

Figure 2.5: Chemical structural formula of epigallocatechin-3-gallate (EGCG) (adapted from [56]).

2.3.2. Green Tea Catechins and their anticancer mechanisms

The anticancer activity of GTE is multitarget and modulates several signalling pathways and biological mechanisms. It is believed that EGCG, being the major polyphenolic constituent, mediates most of anticarcinogenic effects of GT [57]; hence, in this dissertation, the terms Green Tea, Green Tea Extract and EGCG will refer to the same concept. The following paragraphs will schematize the 7 discovered main actions of GT against CRC. Notably, all these mechanisms are not independent from each other but, on the contrary, are correlated. A visual representation is also presented in **Figure 2.6**.

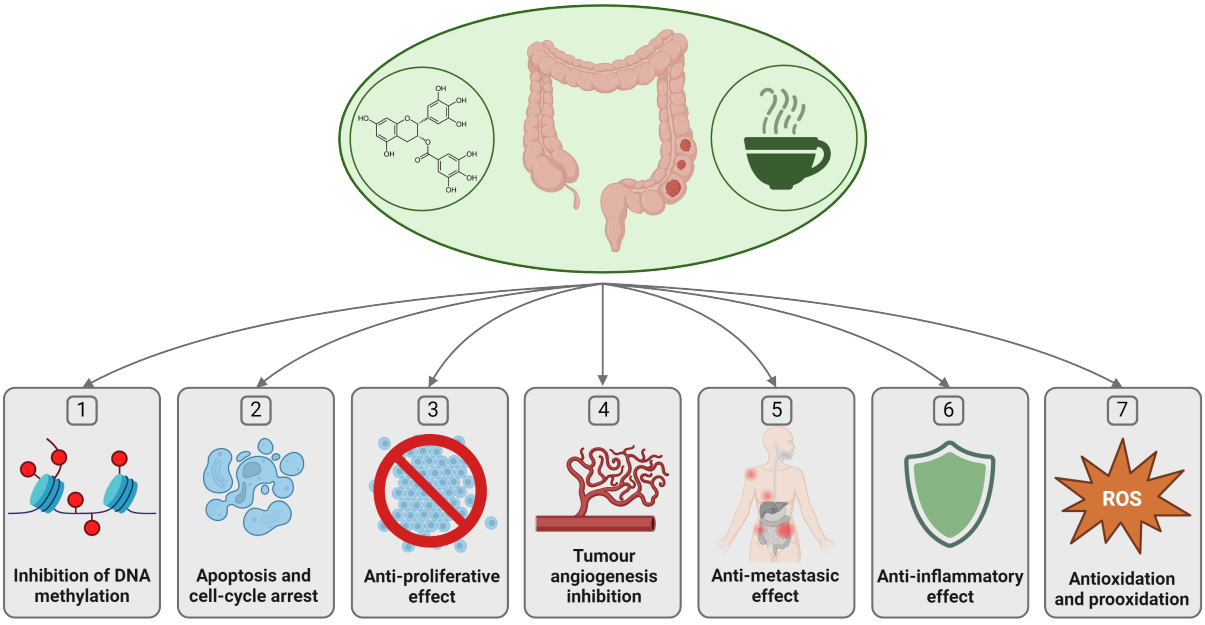

Figure 2.6: The anticarcinogenic mechanisms of GT catechins (adapted from [58]) (created with BioRender.com).

2.3.2.1. Inhibition of DNA methylation

DNA methylation, together with histone deacetylation, is a key epigenetic mechanisms for the silencing of many genes such as tumour-suppressor genes, genes deputed to cell cycle regulation and control, cells programmed death and DNA repair [59]. For instance, if DNA repair gene is methylated, DNA loses its repairing ability. Hence, DNA damages accumulate causing the multiplication of errors and mutations during DNA synthesis, which can lead to cancer. It has been shown that EGCG os able to reduce the expression of two genes which play a fundamental role in epigenetic aberrations (DNA methyltransferases and histone deacetylases) in methylation-sensitive HCT-116 colon cancer cells [59].

2.3.2.2. Apoptosis and cell cycle arrest

Apoptosis is the cells' natural mechanism for programmed death and is fundamental to hinder cancer diffusion. A study performed by Chen et al. reported that EGCG downregulates the hyperactivation of Wnt/β-catenin pathway, a key mechanism in driving colorectal carcinogenesis [60]. According to further scientific evidence, EGCG induces cell apoptosis in colorectal cancer cells through the activation of two more pathways: MAPK (mitogen-activated protein kinase) and Akt (protein kinase B) [15].

2.3.2.3. Anti-proliferative effect

A report documenting the anti-proliferative effect concluded that GT stops the proliferation of malignant cells through the regulation of notch signalling, a mechanism with a pivotal role in regulating the development, renewal, and maturation of tumor stem cells [61].

2.3.2.4. Tumour angiogenesis inhibition

In fact, angiogenesis and cancer proliferation are closely related, as they are the main responsibles for cancer growth. Angiogenesis is the development of new blood vessels from the pre-existing vessels, which supply a cancerous tissue with oxygen and nutrients to promote its growth [62]. The vascular endothelial growth factor (VEGF) is a crucial angiogenic factor for inducing and maintaining neovascularization in malignant sites. VEGF binds to and activates vascular endothelial growth factor receptorss (VEGFRs). A study performed by Shimizu et al. reported that EGCG can suppress the activation of the VEGF/VEGFR axis, as well as of several downstream molecules. Furthermore, a reduction of CRC xenografts in nude mice was observed. These results suggest that GTE may exert an anti-angiogenic and, consequently, a growth inhibitory effect on CRC cells [63, 64].

2.3.2.5. Anti-metastatic effect

The anti-metastatic action of GT can be due to the four aforementioned effects. Literature evidences that GT catechins act to suppress and reduce liver metastases of CRC cells, hindering angiogenesis and inducing their apoptosis [65]. This outcome is extremely relevant since the

liver is the primary location for metastasis of colorectal cancer, as stated in **subsection 2.1.2** on page 7.

2.3.2.6. Anti-inflammatory effect

The anti-inflammatory effect of EGCG is well known, but it does not seem to be connected to cancer development. However, tumour-elicited inflammation and therapy-induced inflammation are the two main ways through which inflammation can promote cancer development, and turn the tumour microenvironment immunosuppressive. In particular chemotherapy can cause not only tumour cell death, but also alterations within the tumour microenvironment, thus evoking 'wound-healing' responses [29]. For instance, the catabolic enzyme indoleamine 2,3-dioxygenase (IDO) is an immune suppressor associated with cancer-related immunosuppression. EGCG significantly attenuates IDO activity in colorectal cancer cells, thus exerting antitumour action [66].

2.3.2.7. Anti-oxidation and pro-oxidation

The last, but not least, important feature of GT catechins is the presence of OH groups in their molecules, making them both antioxidant and pro-oxidant. Actually, cancer is characterized by oxidative stress, *i.e.*, an increased imbalance between reactive oxygen species (ROS) and antioxidants. Moreover, most anti-cancer drugs work by inducing oxidative stress: this has been related to the remarkable damage to healthy cells and the arising of drug resistance [67]. ROS are a double-faced actor in the malignant environment: in the right amount, they are useful to induce apoptosis and inhibit cancer proliferation; whereas if accumulating, they can promote gene aberrations and pro-oncogenic signalling. Another tumour accomplice are metal ions, which enhance the proliferation of cancer cells. Literature reports that GTE has the positive anti-oxidant effects to reduce consequences of oxidative damage: they enhance anti-oxidant enzymes, scavenge carcinogenesis-induced ROS, promote the repair of DNA and chelate metal ions [58]. On the other hand, the pro-oxidant activity of catechins, whether used in the right amount, results in the beneficial production of ROS. Thus, both antioxidant and pro-oxidant activity of GT play pivotal roles during the cancer process [68].

3 In vitro studies

3.1. General aim

In vitro models are a critical tool for cancer research as they allow to produce reliable biomedical information and help to predict anticancer drug response [69]. They have also the advantage of reduced costs, they overcome limited access to clinical samples, and impossibility of repeated trials in humans. In this work, monolayer culture of cancer cells [two-dimensional (2D) features] have been used. In particular, the WiDr cell line (ATTC®) has been selected [70]. It is well documented that the cellular and biochemical microenvironments of the body have a strong influence on cancer development [71]. Thus, this *in vitro* model was an oversimplified version of *in vivo* tumour conditions. Research focused only on: cells, culture medium, chemodrugs, and GTE. Notably, the chosen setting did not reproduce the complexity of the interaction between cancer cells and other tissues surrounding the cancer itself (including signalling molecules, receptors, other cells, etc.). Consequently, not all the mechanisms of action of GT against CRC will be evidenced and studied. Hence, while looking at the outcomes of this technique, it is important to keep in mind that *in vitro* essays grasp limited aspects of tumour microenvironment, but at the same time they allow to control most experimental variables, enabling quantitative analysis. In addition, due to this oversimplification, it will not be so unreasonable if some results are not as good as expected. Briefly, the goal of this chapter will be the evaluation of the cytotoxicity of a GTE towards WiDr cells, as a potential adjuvant agent for reducing malignant cell proliferation (see **subsection 1.2**, page 3).

3.2. Materials and Methods

This section will focused on the description of both equipment and procedures used during the *in vitro* experimental studies.

(a) Adherent to the bottom of the flask and to each other.

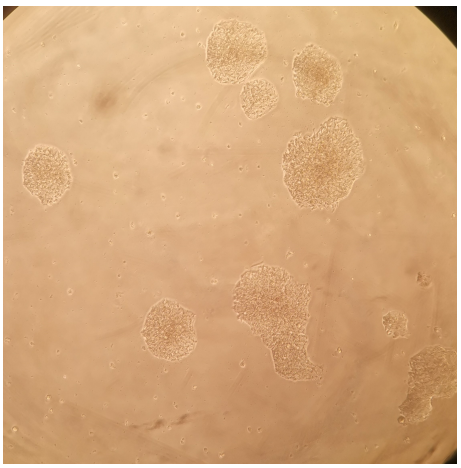

(b) Adherent to the bottom of the flask when forming isolated clumps.

Figure 3.1: Microphotographs of WiDr cells captured with a contrast phase optical microscope (CPOM) (*Nikon Eclipse, TS100, Japan*)(10 x magnification).

3.2.1. Cell line

The *in vitro* assays have been done with the WiDr cell line (*American Type Culture Collection® (ATTC®) CCL-218™*). The WiDr cells, exhibiting an epithelial morphology are adherent cells which have been demonstrated to be tumorigenic (**Figure 3.1**). Originally this line was thought to have been isolated from the colon of a 78-year-old female patient with colorectal adenocarcinoma cancer. Nevertheless, DNA fingerprinting has shown it is a derivative of HT-29 (*ATCC HTB-38*) [72]. WiDr cells were acquired by the Institute of Biophysics of the Faculty of Medicine of the University of Coimbra (FMUC). These cells were grown in sterile flat-bottom flasks for adherent cells, with vented screw caps (*Corning 430639, 431080 or Corning 430825*, according to the chosen size) and they were stored in a incubator under the following conditions: 37°C, 95% of humidity and 5% CO_2. The cells' choice was advantageous not only because of their tumorigenicity[1], but also because they are easy to propagate in culture, with a short population doubling-time (about 15 hours) and a relatively high plating efficiency (51%) [72]. The original sample coming from ATTC® was thawed, cultured, divided and stocked into several mother aliquots, which were kept in cryopreservation conditions to ensure quality maintenance during the storage period. **Figure 3.1** shows the microscopical appearance of adhered WiDr cells.

3.2.2. Cell culture

The cell culture procedure allows to cultivate cells outside a living organism. Hence, in order to mimic physiological conditions and favour cellular growth, the cell culture environment must be strictly controlled and monitored. During this work, all cell procedures were performed in a dedicated culture room, using sterile material (discardable when possible) under aseptic conditions. The specific equipment which allowed appropriate settings consisted of:

[1] Essential for the *in vivo* planned studies.

Table 3.1: Description of the main equipment/material used during cell manipulations (*Biophysics Institute, FMUC-iCBR-cibb, Portugal*).

EQUIPMENT	FUNCTION	CHARACTERISTICS
Vertical laminar flow chamber **Figure 3.2a**	It is an enclosed workstation in which stable vertical unidirectional flow creates an environment protected against particle or biological contamination.	It draws air from the surrounding room into its bench through a perforated opening at the top. Then this air is pressurized and filtered. It is provided with an ultraviolet light lamp that sterilizes its interior before use.
Cell culture flasks **Figure 3.2b**	These flasks are specifically designed for successful growth, propagation and adhesion of cells. They were stored in the incubator.	They are sterile, sealed with a vented screw cap and have a flat bottom.
Incubator **Figure 3.2c**	It is a device used for cell culture, which helps to maintain the optimal conditions required for the growth and survival of cells.	Cells were cultured at a constant temperature (37°C), humidity (95%) and 5% CO_2.
Contrast phase CPOM 3.2d	It is used to observe cells and culture medium, and verify whatever cell maintenance is needed (*e.g.* cell confluence[2] or checking for the presence of contamination).	As cells are naturally non-colored, the objectives are located under the microscope stage, where the flasks for observation are placed.
Refrigerated centrifuge **Figure 3.2e**	Falcon tubes are inserted in it and are subject to a centrifugal rotation and acceleration at high speed for a certain time, at a chosen temperature. This leads to the the sedimentation of the components of a suspension/solution.	At each time it was set at 4°C, 1,100 rpm for 5 minutes. The low temperature was set to reduce cellular metabolism and the rotation speed was selected to maintain the integrity of the cellular membranes.
Thermostatic water bath **Figure 3.2f**	It is used to heat or to keep samples of substances at a certain temperature.	It was useful to heat culture medium before using it, being set at 37°C.

- a vertical laminar flow chamber (*Holten Lamin Air, HB2448, USA*),
- an incubator (*Binder, Dias de Sousa S.A, Portugal; certified by Certilab, Portugal*),
- an inverted CPOM (*Nikon Eclipse, TS100, Japan*),
- a refrigerated centrifuge (*Thermo Scientific, Heraeus Multifuge 1L-R, USA*),
- a thermostatic water bath (*Tissue water bath, GFL 1002, Germany*),
- a dedicated refrigerator.

Special culture material has been used:

- sterile flat-bottom flasks for adherent cells, with vented screw caps (*Corning 430693 or 43639, USA*),
- sterile Falcon tubes (*Sarsted, 62.554.502, Germany*),
- micropipettes and respective sterile tips (*BioPette TM Plus, Labnet, USA*),
- a vacuum pump (*Vacusafe, Integra Biosciences SAS, France*),
- graduated sterile glass pipettes (*Normax, Portugal*),
- sterile glass Pasteur pipettes (*VWR, Pasteur Pipettes 612-1702, France*),
- automatic pipettor (*Gilson, Pipetting Aid 080333, France*).

Table 3.1 provides the description and the functions of each aforementioned equipment, whereas **Figure 3.2** depicts them.
The compliance with specific laboratory rules was guaranteed to keep optimum conditions and to minimize the possibility of contaminations. Within the cell culture room all the procedures involved the use of discardable nitrile gloves, designated lab coats and face masks. Furthermore, the cell culture room was provided with an anteroom: the doors of the room and the anteroom were never opened simultaneously in order to avoid the direct contact with outer air. It was also guaranteed that the incubator door was opened only when the culture room's door was closed. All material (discardable and glass) was sterile and everything that went into the laminar flow chamber was previously sprayed with 75% ethanol[3] [73]. Before plating, cells were tested for possible mycoplasma contamination and the culture medium was tested at least for 72 h before use and checked at the CPOM to verify the absence of microbiological contamination (bacteria and fungi). At the end of each manipulation all material which contacted with cancer cells was inactivated with bleach (NaClO) and then either discarded in special containers as waste to be

[1] In cell culture, adherent cells require a surface to attach and grow on. When these cells reach a point where they have completely covered the available growth surface, this is called confluence or a confluent monolayer.

[2] In cell culture, adherent cells require a surface to attach and grow on. When these cells reach a point where they have completely covered the available growth surface, this is called confluence or a confluent monolayer.

[3] This, because ethanol has an inactivating effect on bacteria and viruses: it can denature their proteins, disrupt their cell wall and kill them.

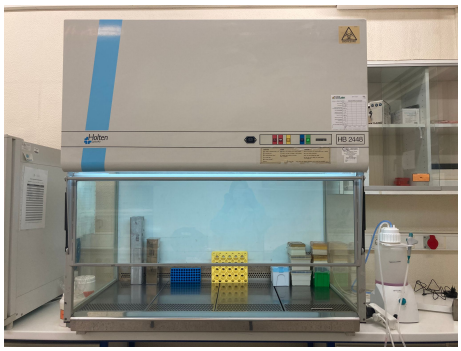

(a) Vertical laminar flow chamber

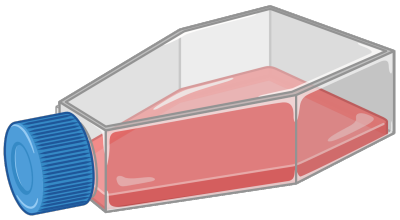

(b) cell culture flask

(c) incubator

(d) CPOM

(e) refrigerated centrifuge

(f) thermostatic water bath

Figure 3.2: Laboratory equipment (*Biophysics Institute, FMUC-iCBR-cibb, Portugal*).

incinerated or washed with tap and distilled water and finally sterilized in an autoclave (only if there were conditions for reuse). All above mentioned equipment and material was in the cell culture room, apart from the thermostatic bath and the refrigerator which were kept in another laboratory room.

3.2.2.1. Culture medium

Cell culture medium is a nutrient-rich liquid or gel, which is vital for a culture environment as it supplies components (e.g. nutrients, growth factors, vitamins, etc.) that promote the growth and health of cells [74]. Culture media tipically contain a mixture of the following components:

- **buffering systems**: they regulate pH, which is a crucial element for optimum culture condition;
- **an inorganic salt mixture**: it is useful to preserve the osmolarity and to regulate membrane potential by supplying sodium, potassium, and calcium ions;
- **amino acids**: they are vital for cell proliferation as they are not able to synthesize them by themselves. L-glutamine, in particular, is an important auxiliary source of energy [75];
- **carbohydrates** (*e.g.* glucose): in the form of sugars, they are the major fuel of cells;
- **antibiotics**: their role is not promoting cell growth, but controlling and preventing the growth of contaminants (bacteria and fungi); an example of antibiotics combination is penicillin/streptomycin (Pen/Strep);
- **trace elements** (*e.g.* metal ions): they are a key micronutrient for many biological processes, such as the maintenance of enzyme functionality;
- **vitamins**: many of them are important promoters of cell proliferation. This supplement is needed as vitamins cannot be produced in sufficient amounts by cells themselves;
- **serum** (*e.g.* foetal bovine serum (FBS)): it carries growth factors and hormones that stimulate cellular functionality, growth and proliferation. It promotes the attachment of cells, helping tokeep the pH around physiological value (7.35-7.45), and plays many other auxiliary functions [74].

The producer of the selected cell line, gives the following instructions: Eagle's Minimum Essential Medium (EMEM) (*ATTC® 30-2003™*) should be used as base medium, and FBS should be added to it until reaching a final concentration of 10% to obtain a complete growth medium [70]. Hence, EMEM should contain 2 *mM* of L-glutamine, 1% of non-essential amino acids, FBS at 10% and 1% of Pen/Strep [76]. Additionally, medium renewal should be performed twice or three times a week. Despite these directions, in order to increase cell culture potential, the chosen medium for the current work was DMEM (*Gibco® 1x, 11966-025, UK*), supplemented with 1% of L-glutamine (*Biowest, Lglutamine 100x, 200mM, XO55O-100, USA*), enriched with 5% FBS (*SigmaAldrich®, F7524, USA*) and 1% of Pen/Strep (*Lonza Pen Strep, Amphotericin, B 100x, 17-745E, USA*). This solution was not so far from instructions, as EMEM and DMEM have the same origin: each of them is a variation of the *Basal Medium Eagle* by Harry Eagle. DMEM was preferred to EMEM since it contains more nutrients: if compared to EMEM, it has a double amount of non-essential amino acids, four times the amount of vitamins, some supplementary

amino acids and a higher concentration of glucose (4,500 mg/L) [74]. Therefore, this enriched formulation favours a faster growth of cells. Furthermore, the addition of FBS is a crucial aid to the survival and proliferation of cultured cells.

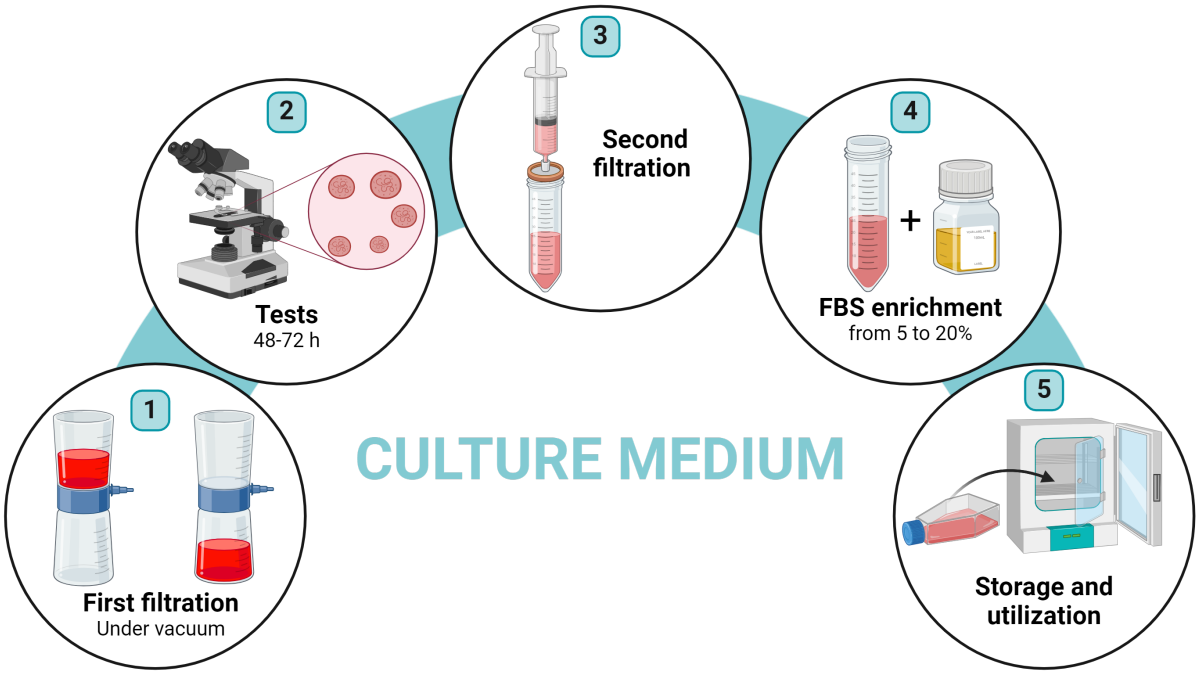

Figure 3.3: Main steps of the DMEM preparation (created with BioRender.com).

The procedure to prepare DMEM is shown in **Figure 3.3**. The powdered reagents were added to ultrapure water and then adjusted to physiological pH (7.4). Afterwards, inside the laminar flow chamber, the obtained medium was filtered under vacuum, in order to ensure its sterilization. Subsequently, it was tested to verify the absence of whatever microbiological contamination and, if negative, it was ulteriorly filtered to minimize the possibility of contamination. The second filtration was carried out using syringe filters (*Merck Millipore SLGSR33SS Syringe Filter Millex - 33mm; 0,22 μm (EOG)*). After this, the obtained medium was enriched with FBS at 5% concentration (*i.e.* 2.5 mL of FBS in 50 mL of DMEM). To preserve its properties and decrease contamination conditions, DMEM was stored in a fridge set at 4° C. The storage occurred in the dark, to prevent the degradation of vitamins, which are important for cell growth. Herein, the thermostatic water bath (**Figure 3.2f**) was set at 37° C to warm up, at body temperature, the medium coming from the fridge before its use. Ultimately, a relevant component of DMEM is a pH indicator (*e.g.* phenol red): the medium turns orange-yellow if the environment is more acidic, whereas it turns pinker in case of basicity. As described in **subsection 3.2.2.3** (on page 26), this coloration is useful to rapidly assess if the cells are more or less active, and, consequently, renew the medium to ensure their continuous development.

3.2.2.2. Cell thawing

WiDr cells were brought by the Biophysics Institute cryopreserved by the producer. Cryopreservation enables reproducibility: it stops cellular clocks, thus allowing the use of very similar batches of cells for months, years, or even decades apart [77]. WiDr cells were supplied as aliquots stored into cryogenic vials and packed in dry ice during transportation. ATTC® recommends: WiDr cells must be placed at a temperature below -130° C, preferably in liquid nitrogen vapor [70]. Thus, in case of long cryopreservation, stock aliquots were stored in a liquid nitrogen chamber (*ThermoNorma, Cryoplus 1, USA*) at -190° C; otherwise, if they were going to be used sooner, they were stored in a freezer set at -80° C (*Thermo Scientific, Herafreeze HFUT Series, USA*). The supplied 'mother aliquots' were expanded, which means that the content of a single vial (1 *mL* of cell suspension) was cultured to produce multiple aliquots, *i.e.* to obtain a larger population of cells to be used in many experiences. The thawing procedure (either of a stock aliquot or of the mother aliquot) is described below and schematized in the upper panel of **Figure 3.4**.

Immediately after their withdrawal from the refrigerator (or dry ice), cryogenic vials were defrosted in the thermostatic water bath (37° C) and brought into the cell culture room. The process started within the laminar flow chamber; the content of the thawed vial was transferred into a 15 *mL* sterile Falcon tube (*SARSTEDT 15 mL, 62.554.504, Germany*) and resuspended in 2-3 *mL* of complete DMEM (5% FBS and 1% Pen/Strep)[4]. DMEM was added to minimize the adverse effects of dimethyl sulfoxide (DMSO), which was used by the producer/users at the laboratory [5]. Then the Falcon containing the suspension was removed from the flow chamber to undergo centrifugation (1,100 rpm, 4° C, 5 minutes). Once more inside the flow chamber, the obtained supernatant, containing the cryoprotectant+medium mixture, was withdrawn from the tube, whereas the pellet - containing WiDr cells clump - was resuspended in 1-2 *mL* of DMEM. Finally, the cell suspension was transferred into a flat-bottom cell culture flask. According to the pellet size, two different sizes of culture flasks were used: 25 cm^2 (*Corning 430693, USA*) or 75 cm^2 (*Corning, 43639, USA*). Approximately 5 *mL* or with 25 *mL* of DMEM, for smaller and bigger flasks, respectively, were added to each flask. Culture flasks were stored in the referred incubator in a controlled atmosphere (37°C, 95% H_2O and 5% CO_2). Flasks were routinely checked in a daily basis and, if needed, the medium was changed, as described below.

3.2.2.3. Cell maintenance

It is important to remark that whatever manipulation or maintenance procedure done concerning the WiDr cells must occur at least 48 hours after cell seeding in the culture flasks. In fact, WiDr cells need at least 2 days to adhere to its bottom and to start proliferating. In this case,

[4]When produced at the laboratory, powdered DMEM is used, adding 1% Pen/Strep. Complete DMEM medium is DMEM which has been supplemented with FBS. Whenever DMEM is referred as such it means it is already supplemented.

[5]DMSO is a cryoprotective agent used for cryopreservation, which means that it helps preventing intracellular ice formation that induces cell death. Usually used at concentrations varying from 5 to 15%, it should be removed as soon as possible when cells are thawed [78].

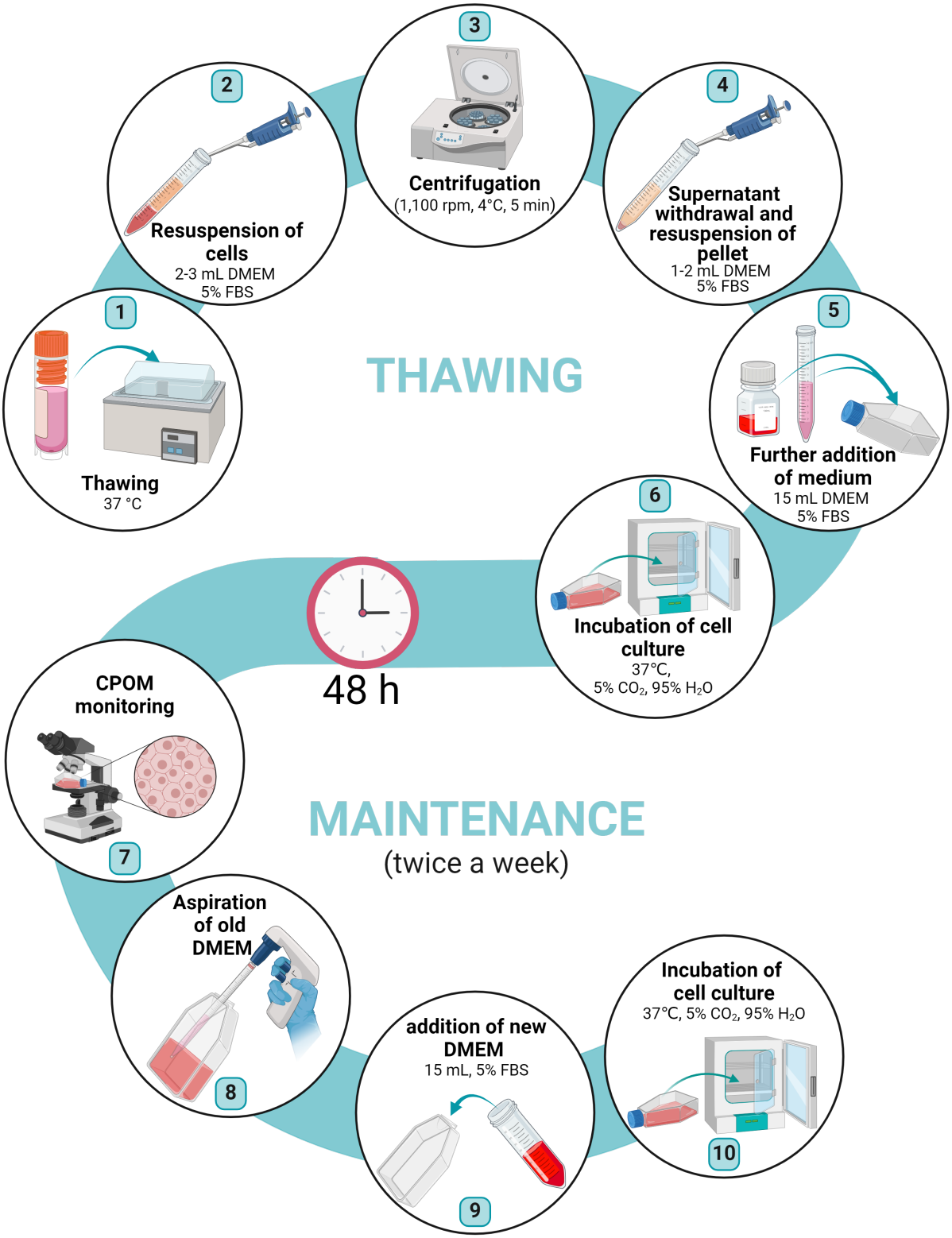

Figure 3.4: Schematic representation of the main steps of cell thawing and cell maintenance procedures (created with BioRender.com).

maintaining cells meant monitoring the progression of cultured cells' growth and proliferation daily. This evaluation was performed firstly with a visual inspection of the medium coloration (due to the presence of phenol red, see **subsection 3.2.2.1**, page 24) and secondly with a more accurate observation at the CPOM. As cells grow they consume the culture medium nourishment, and subsequently, they produce acid metabolites which will acidify the surrounding environment. Hence, an expert operator can perceive what is occurring at a glance. An orangish or yellowish medium, can be a hint on the accumulation of waste metabolites, corresponding to an increased acidity, an obstacle to cell growth [79]. In this case, medium renewal is the solution: it is a way of providing fresh nutrients to cells and cleaning their surrounding environment. DMEM was usually changed twice a week: the steps are illustrated in the lower part of **Figure 3.4**, being done inside the laminar flow chamber. To begin with, medium removal was gently made with a glass *Pasteur* pipette (*VWR®, Pasteur Pipettes 612-1702, France*) coupled to a vacuum pump (*Integra Vacusafe, Dias de Sousa S.A, Portugal*). Then, around 15 *mL* of new DMEM (previously tested, enriched with 5% FBS and warmed up at 37° C) were added to the culture flask. The flask was thus sprayed with 75% ethanol and placed into the incubator.
The medium colour check alone, is not enough: CPOM observation is crucial for several reasons: it confirms the need of medium renewal, it detects the presence of contamination, it checks on cells' proliferation, and it verifies the presence of detached or dead cells. Moreover, a daily CPOM monitoring is useful to ascertain the culture confluence and proceed with detachment at the right moment, as described in the subsequent paragraph. WiDr cells may grow forming 'cell bubbles', also named as clumps (**Figure 3.1**). Cell clumping should be avoided as it reduces access to critical nutrients and, as a result, prevents overall cell growth. Hence, in case of cell clumping, a useful procedure to allow their branched growth was: retrieving the medium, applying the detachment protocol and putting the obtained cell suspension in a new culture flask.

3.2.2.4. Cell detachment

During the maintenance phase, adherent WiDr cells grew and proliferated. Herein, as soon as this monolayer reached 70-80% confluence, a specific detachment protocol was applied to obtain them before further passages[6]. The area of bottom flask coverage must not overpass the 70-80% limit, otherwise cells would not have enough space. Most cell lines growth is inhibited by contact and, consequently, they die when overcrowded. Although WiDr cells can grow in piles, simulating stalagmites, and small dots at the bottom of the culture flasks become visible to the naked eye, it is not advisable for this to happen, as explained above and in the footnote. Detachment is a process that helps to break the interactions between cell adhesion proteins and the surface of the flask, thus allowing cell release while keeping their viability and membrane integrity [80]. There are two strategies to obtain cell detachment: mechanically or enzymatically.

[6]**Cell passage** is a routine procedure in cell culture that serves several purposes: i) **maintaining healthy cell growth**: by preventing overcrowding and ensuring access to fresh nutrients and space, passaging promotes optimal cell health and function; ii) **expanding cell cultures**: each passage allows to increase the total number of cells available for experiments or other applications; iii) **maintaining specific cell characteristics**: regularly passaged cells are typically more uniform and predictable in their behaviour.

In the current study the enzymatic way was chosen due to the strong adherent profile of WiDr cells, and also because it is more convenient to preserve the cells: TrypLE™ Express (*Gibco by life tecnologiesTM, Denmark*) was the used enzymatic solution. It is a recombinant bacterial-derived animal-free trypsin product. It can be classified as a proteolytic enzyme, since it promotes the cellular dissociation similarly to trypsin[7]: it cleaves at the amino-arginine and lysine site [81], which are the major responsibles for the anchoring of cells to the flask surface. Moreover, if compared to trypsin, TrypLE™ activity towards cells is gentler [82].
To sum up, soon after microscopical assessment, detachment took place: its steps are illustrated in **Figure 3.5**. The process started with the medium careful aspiration by pipetting under vacuum (similarly as described in **subsection 3.2.2.3**). Hence, TrypLE™ was poured into the flask, in such an amount that could cover the entire bottom of the flask (about 5-7 *mL*). Herein, the flask was incubated for 5 minutes (similar conditions as for culture) to let the enzyme act. Then, the flask was checked by CPOM to ensure that most of the cells were detached. If the purpose was achieved, inside the flow chamber, TrypLE™ reaction was inactivated by adding 1 *mL* of DMEM. Then, using a sterile glass Pasteur pipette coupled to an automatic pipette controller (*Pipetboy ACU 2, INTEGRA, China*) the cell suspension was transferred into a 15 *mL Falcon* tube, which underwent centrifugation (1,100 rpm, 4° C, 5 min). At the end, again inside the flow chamber, the removal of the supernatant and a second resuspension of the obtained pellet were (1 *mL* of DMEM).
The final product of this procedure was a suspension of detached cells which could have three different goals:

1. count cells to be plated for *in vitro* essays;

2. count cells to be subcutaneously injected to mice for *in vivo* studies;

3. if there was a surplus of cells, the suspension was placed into a cryogenic vial (*SARSTEDT, 72380992, Germany*), in a total volume of 1 - 1.5 *mL* of DMEM and added with 10% DMSO. In this way, exceeding cells were cryopreserved at -80° C as stock aliquots to be used in near future experiments.

3.2.2.5. Cell counting

Cell counting is the quantification of the number of cells within a specific volume of suspension: it is a preliminary step, necessary to start both any *in vitro* and *in vivo* experiments. Notably, for the present work, it was indispensable to know how many cells were going to be plated for *in vitro* assays, considering the number of wells/plate (typically 48) and how many cells were needed for each animal inoculation. There are two methods to quantify cells: a manual method, which relies mainly on an optical microscope and counting chambers and an automatic one. It is true that manual counting is time-consuming, and is subject to human error, particularly if performing many cells counts sequentially [83]. However, manual methods, if compared with the

[7]Trypsin is the commonly used enzymatic agent for cell detachment.

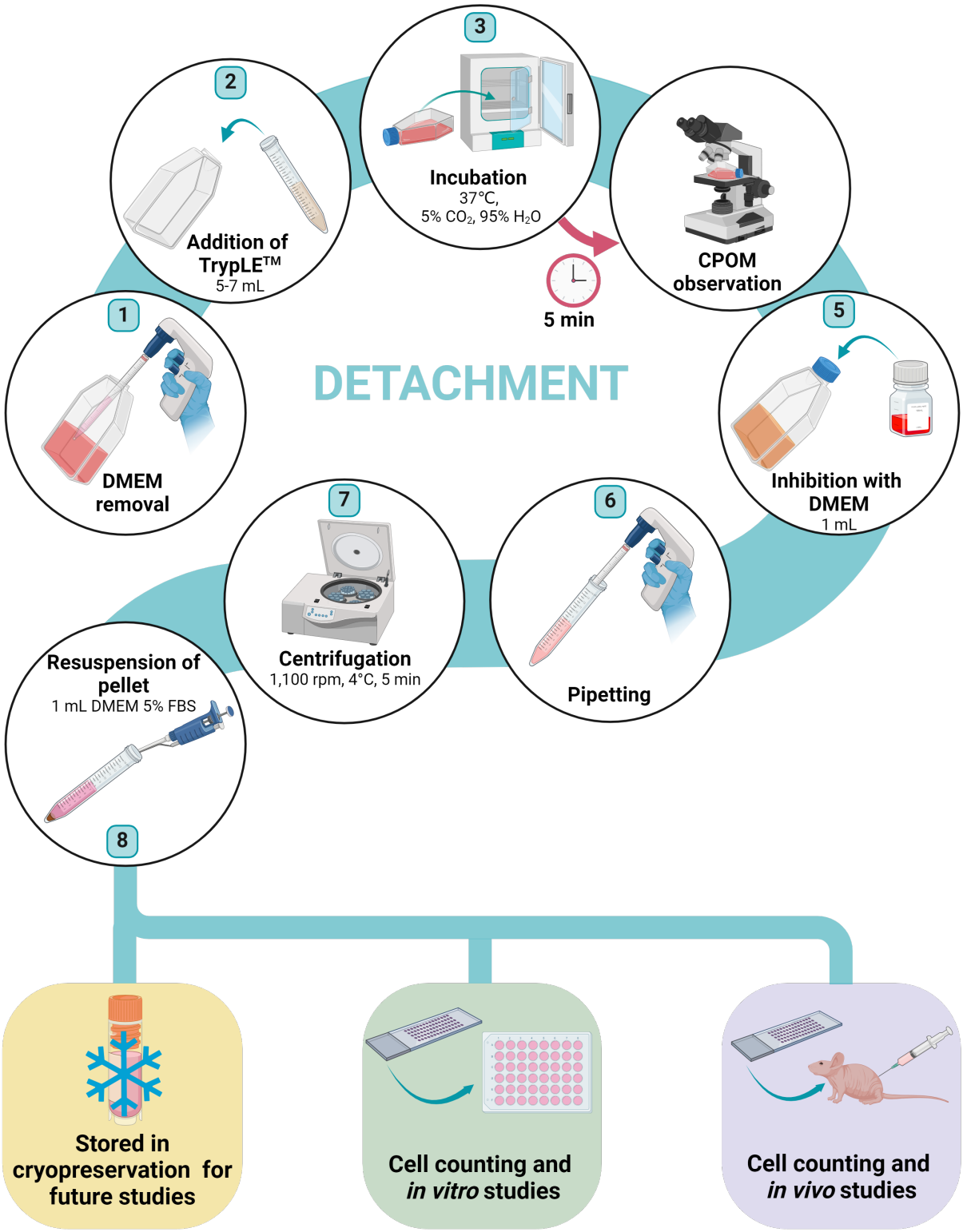

Figure 3.5: Schematic representation of the main steps for the cell detachment process. The lower bubbles show the three main uses of detached cells (created with BioRender.com).

automatic one, rely on a more scientific measurement principle [84]. Therefore, in the present study a manual cell counting protocol was applied. The main tool used for this protocol was a counting chamber, also known as haemocytometer; in particular, a Neubauer chamber (*Marienfeld Neubauer Improve Bright-line, 0640030, Germany*) was used. A detailed description of this chamber is shown in **Figure 3.6**: it is made of a thick optical glass with overall dimensions 30×70×4 *mm*. It shows two separated counting grids which can be used to quantify two different sample microvolumes. A counting grid is a square of 3 *mm* side, further divided into 9 squares, each with a 1 mm^2 area, making up a total of 9 mm^2. Among the 1 mm^2 squares (wich will be referred as *big squares*), there are 4 *corner squares* (orange in **Figure 3.6**) and one *central square* (red in **Figure 3.6**). Each corner square is again partitioned into 16 *small squares* (green in **Figure 3.6**, each one with a 0.25 *mm* side). Finally, the central square is divided into 25 more squares, which are in turn divided into 16 *tiny squares*. This last partition allows to quantify samples with an extremely high cellular density. The chamber is topped with a 0.4 *mm* thick cover glass (*RS, Cover Glass 100 PCS Thickness 0.13-0.17 mm, France*) to limit the volume over the counting grids.

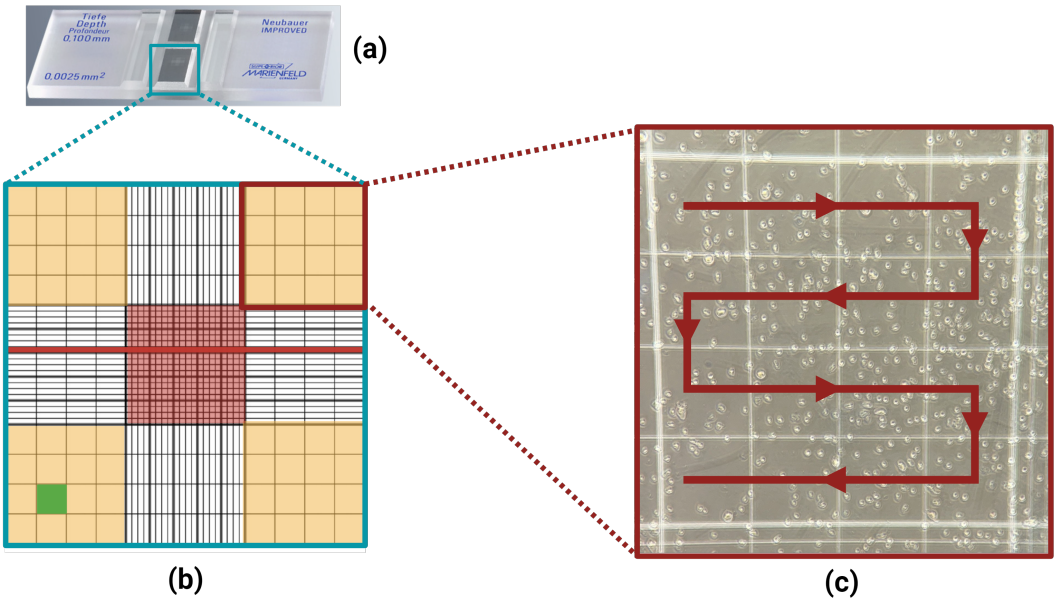

Figure 3.6: Several details of the used Neubauer Chamber during the counting process: **(a)** chamber made of optical glass, with overall dimensions $30 \times 70 \times 4$ *mm* (adapted from [85]); **(b)** overall grid: the total side measure of the main square is 3 *mm*. The side of each corner square (orange) and of the centre square (red) is 1 *mm*. Each corner square is divided again into 16 small squares (0.25 *mm* side). Finally, the centre square is divided into 25 squares, which are again divided into 16 tiny squares, whose side is 0.05 *mm* (red line thickness) (adapted from [86]); **(c)** CPOM detail of a corner square, in which the counting snake-shaped trajectory is shown.

The counting process is illustrated in **Figure 3.6**: as soon as the suspension of detached cells was obtained (subsection 3.2.2.4 [8]), 10 μL of the cell suspension were pipetted into a 2 *mL eppendorf* tube (*DeltaLab S.L., 4092.2N, Spain*). Subsequently, out of the laminar flow chamber, the same amount (10 μL) of 4% trypan blue (*Sigma-Aldrich®, T0776, USA*) was gently homogenized with

[8] Pellet resuspended in 1 mL of DMEM

the suspension within the same eppendorf tube. Trypan blue is a vital dye used to stain cells for the *dye exclusion test*, which quantifies the number of viable cells in a cell suspension. It is based upon the principle that the membranes of competent cells are intact and, as a result, they exclude certain dyes, including trypan blue. Hence, only dead cells with a compromised cell membrane are stained [87]. This means that cell counting will take into consideration only non-blue cells, *i.e.* viable ones.

Given this premise, after checking that the coverslip was properly positioned atop the chamber, a 10 μL drop of the cell-trypan mixture was placed within the chamber and the cover glass. It spread over the grid (under the cover glass) due to the capillarity phenomenon. The counting was then performed through by chamber observation under the CPOM (100 or 200$\times$ magnitude). Given the not so high cellular density obtained during this work, the corner squares were suitable

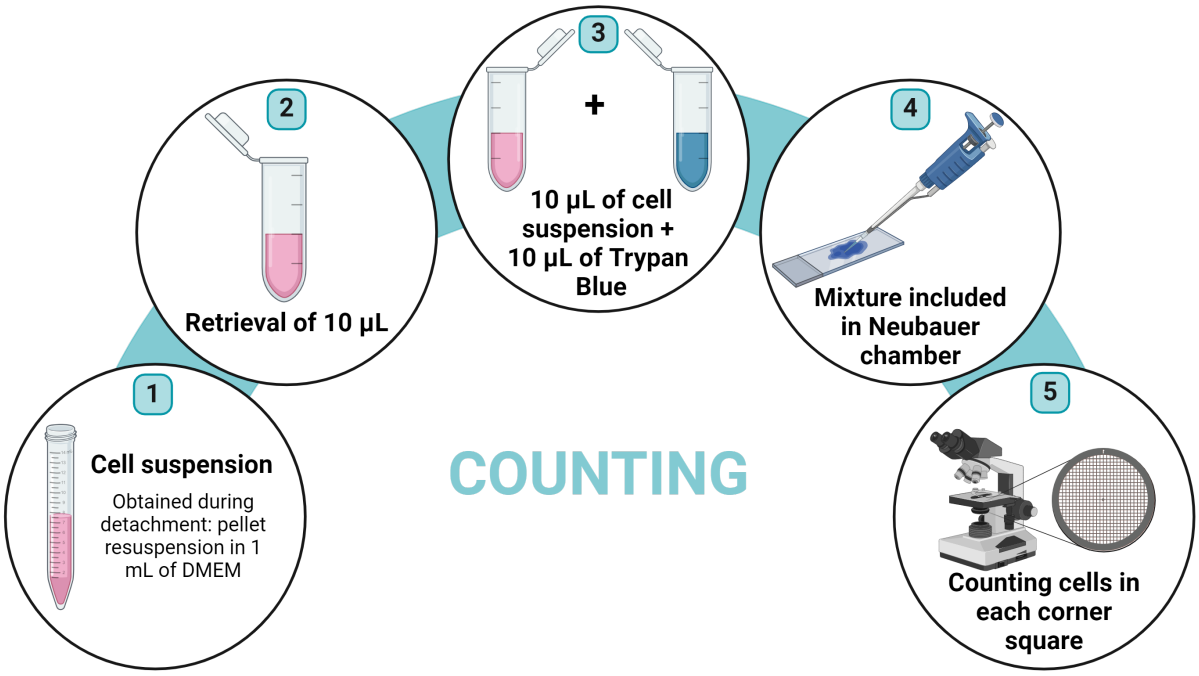

Figure 3.7: Sequence of actions made during counting protocol (created with BioRender.com).

to the quantification. The microscope was focused on one corner square at a time, and cells were counted following a serpentine line crossing all the small squares (*i.e.* starting from the upper-left small square and ending into the lower-right small square), as shown in the third panel of **Figure 3.6**. This trajectory was a strategy to avoid considering the same cell twice or forgetting any square. To a uniform counting, the following rule was set: cells touching the perimeter of small squares, only the ones that are also touching the perimeter of the corner square must be considered. In other words, all cells crossing the internal lines of the corner squares were excluded from the count. Blue cells, which were cells with a disrupted membrane, were also excluded.

After taking note of the number of cells accounted for the corner squares, some calculations were done. First, the volume of each corner square is 1 mm^3 (equal to $1 \cdot 10^{-4}$ mL and to 10^{-1} μL) as it covers a 1 mm^2 area and the space between the glass lamella and the chamber is 1 mm. Second, the total number of cells per microliter (μL) of sample could be calculated starting from the total

number of counted cells and the evaluated volume using the following formula:

$$C\,[cells/\mu L] \;=\; \frac{N \cdot 10}{S} \tag{3.1}$$

Where N is the total number of counted cells, S is the number of considered square corners, and C is the estimate of the number of cells per microliter (μL). Furthermore, if the used suspension had been formerly diluted, the previous formula was multiplied by the dilution factor.

3.2.2.6. Cell seeding/plating

After cells detachment and counting, the seeding/plating took place and the *in vitro* assay begun. This phase was carried out using 48 well plates (*SPL Life Sciences, 30048, Korea*). Each well of these plates have a flat bottom, suitable to adherent cells, with a $0.95\,cm^2$ area. In previous studies, the research group figured out the optimum number of WiDr cells to be seeded: $5.8 \times 10^3\ cells/well$. Herein, a proportion was made to work out the volume (x in μL) of counted cell suspension which should have gone in each well:

$$N\,[cells] : 1\,[\mu L] \;=\; 5.8 \times 10^3\,[cells] : x\,[\mu L] \tag{3.2}$$

The x volume was plated in each well with a micropipette (*BioPette™ Plus*) coupled to sterile tips of adequate size (*Labcon, 1036-800-000-9, USA*). Then, each well was filled with 300 μL of DMEM. The plates covered with their lid and properly sprayed with 75% ethanol, were afterwards stored in the incubator (37°C, 95% H_2O, 5% CO_2). The plates were left undisturbed for the next two days to allow the cells to attach and grow on the bottom of the wells.

3.2.3. Green tea extract powder

GTE was the key player of the whole project: the main goal in this phase was to analyse the possible cytotoxicity of EGCG and its anticancer activity against CRC. Notably, GT was already proved to have highly antioxidant properties, anti-inflammatory effects and an anti-mutagenic action, as investigated in **subsection 2.3.1** (page 15). The GTE used in this study was acquired in a powdered form (GTE po *MyProtein, Green Tea Extract powder, 500 g, 1705807841, UK*). It was chosen after assessing its phytochemical composition using High Performance Liquid Chromatography (HPLC) as a separation technique [88]. Hence, the powder was dissolved to prepare stock solutions to be used during both *in vitro* and *in vivo* assays. The preparation of GT for *in vitro* experiments is described below, whereas the preparation for in *in vivo* studies will be described in **subsection 4.2.2.3** (page 62).

A specific amount of GTE po was weighted with an analytical electronic scale (*Radlag, AS 220/c/2, Germany*, **Figure 3.8**). From here onwards, manipulations were performed in the laminar flow chamber. The weighted powder was dissolved in phosphate-buffered saline (PBS), previously prepared, prepared, being its pH adjusted to physiological value (7.4), and sterilized

via autoclaving[9]. Since the specific aim of *in vitro* studies was to identify the best concentration

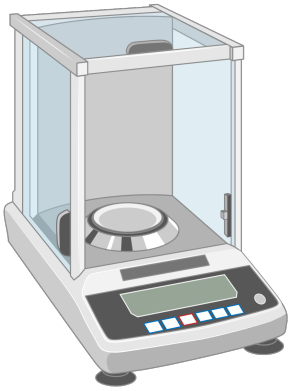

Figure 3.8: Analytical scale used in the laboratory for the preparation of GTE stock solutions (created with BioRender.com).

of GTE, several solutions were obtained using different diluition proportions of GTE po and PBS. Following previous studies of the group, three concentrations were chosen to be tested: 0,5 - 5 - 10 $\mu g/mL$ [90, 91]. The three stock solutions were stored into *Falcon* tubes, sealed with parafilm, duly labelled, protected from light at -20° C. When an *in vitro* assay was about to start, the solutions were defrosted and warmed up at 37° C, aliquoted into 2 *mL Eppendorf* tubes and stored in the fridge at a 4° C.

3.2.4. Tested chemopharmaceuticals and protocols

Three chemo drugs were chosen for the *in vitro* studies, either to be applied alone or in combination with each other: 5-Fluorouracil, Irinotecan and Cyclophosphamide. They are conventionally used in the clinic for CRC chemotherapy. Their mechanisms of action will be briefly described in the following sections.

3.2.4.1. 5-Fluorouracil

5-FU was among the first chemotherapeutic drugs reported to have anticancer effects. It is an antimetabolite: its action is focused on the inhibition of essential biosynthetic processes, and on it being incorporated into macromolecules (DNA and RNA), causing the suppression of their normal function [92]. This drug is an analogue of uracil, a DNA basis: as displayed in **Figure 3.9**. The two molecules are identical, apart from a Fluorine in 5-FU, which replaces a hydrogen at the C-5 position. This similarity gives 5-FU the ability to intercalate in DNA molecules forming adenine-uracil/5-FU base pairs.
The antitumour actions exerted by this drug are represented in **Figure 3.10**. In detail, 5-FU can enter the extremely active cancer cell quickly using the same facilitated transport mechanism as uracil [92]. Once inside them, this molecule is metabolized through two pathways which compete

[9]PBS is a non-toxic saline solution made of sodium chloride, sodium phosphate and potassium phosphate: it acts as a buffer, which means that it regulates the pH of the solution. It is also isotonic to the body fluids, which means that it has the same solute and water concentration [89].

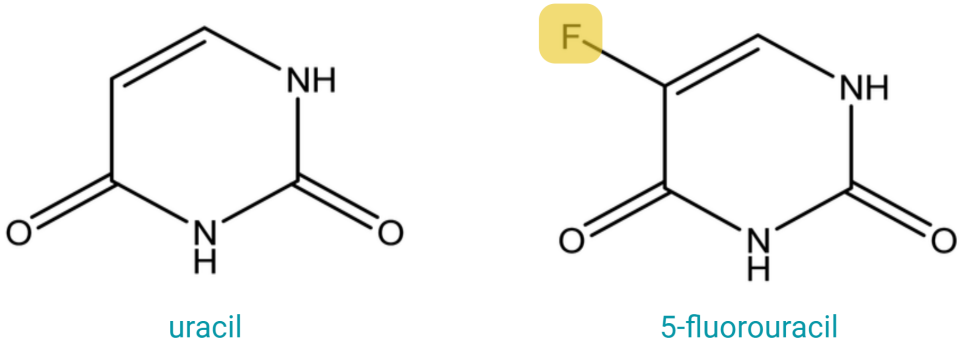

Figure 3.9: Chemical structure of uracil, a DNA basis, versus 5-Fluorouracil, the chemopharmaceutical (created with BioRender.com).

with each other: anabolic and catabolic [93].

Anabolic pathway - Within the cells, some enzymatically catalysed reactions that involve 5-FU and phosphorylated sugars take place. As a result, 5-FU is converted to several active metabolites, the real responsible for anti-cancer effects: 5-fluorouridine-5'-triphosphate (FUTP), 5-fluoro-2'-deoxyuridine-5'-triphosphate (FdUTP) and 5-fluoro-2'-deoxyuridine-5'-monophosphate (FdUMP) [94]. These compounds lead to the disruption of RNA synthesis and to the inhibition of thymidylate synthase (TS) enzyme, an essential precursor for DNA biosynthesis [95]. In other words, 5-FU metabolites cause DNA/RNA damages, which induce cell death [93].

Catabolic pathway - This route is responsible for 5-FU poor bioavailability. Cytotoxic effects of 5-FU are mainly due to its fast catabolic degradation which occurs mainly in the liver. Dihydropyrimidine dehydrogenase (DPD) is the rate-limiting enzyme in this catabolism, as it converts 5-FU into dihydrofluorouracil (DHFU), that is ultimately excreted via the kidneys.
Even if research advanced, 5-FU is still one of the most effective and most commonly used chemopharmaceuticals against CRC [96]. It is often adopted in chemotherapy combination regimens, coupled both with pro-drugs (such as Cyclophosphamide and Irinotecan) and chemo-protectants (*e.g.* Leucovorin) that improve its bioavailability, potentiate its therapeutic effects and, at the same time, limit its toxicity. Usually 5-FU is administered intravenously. Clinically reported side manifestations include fever, fatigue, mucositis, stomatitis, nausea, vomiting, and diarrhoea [94]. In the present study, 5-FU (*Fluorouracilo Hikma 50mg/mL, Hikma Farmacêutica SA, Portugal*) was tested in [400 mg/m^2], [550 mg/m^2] and [600 mg/m^2] concentrations (Figure 3.11).

3.2.4.2. Irinotecan

Irinotecan (IRI) is a semi-synthetic derivative of Camptothecin, a topoisomerase inhibitor which is found in *Camptotheca acuminata*, a plant native to China and Tibet [97]. It is water-soluble and, in aqueous solutions, it shows a dynamic equilibrium which depends on pH: in an acidic environment, it tends to be in the lactone form, whose counterpart is the carboxyl form in a basic

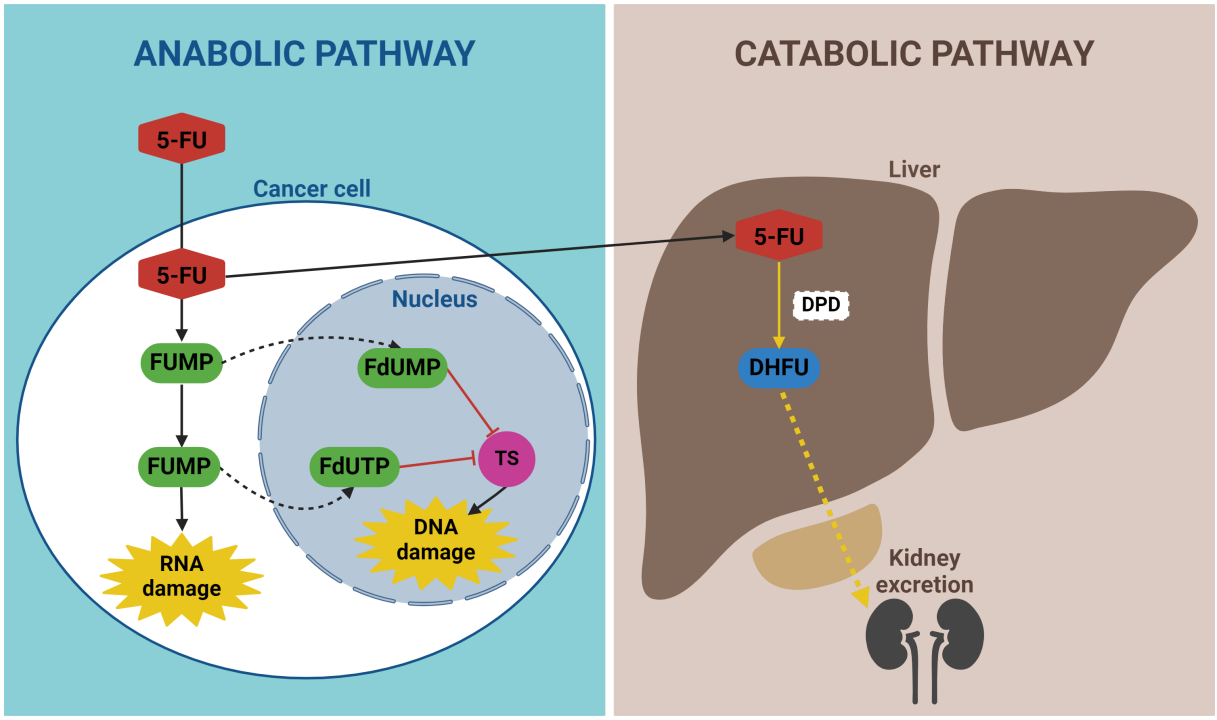

Figure 3.10: Simplified scheme of the metabolic process of 5-FU. Abbreviations: FdUMP, fluorodeoxy-uridinemonophosphate; FdUTP, fluorodeoxyuridinetriphosphate; FUTP, fluoro-uridinetriphosphate; TS, thymidylate synthase; DPD, dihydropyrimidine dehydrogenase; DHFU, dihydrofluorouracil (created with BioRender.com).

Figure 3.11: 5-Fluorouracil tested during this project (obtained through a special protocol between Biophysics Institute-FMUC-iCBR-cibb and CHUC).

encironment. Only the lactone is thought to have anti-cancer effects [98]. IRI is a pro-drug[10]: its active metabolite is SN-38. IRI is classified as a topoisomerase inhibitor as well. Topoisomerase I is an enzyme that carries out a crucial task for DNA replication: it can relax DNA supercoils by temporarily cutting a DNA strand, thus simplifying the rotation of the broken DNA strand around the opposite intact strand. Topoisomerase I catalyses the subsequent closing of this nick [100]. It is believed that IRI, together with SN-38, acts by forbidding the closing of this temporary cut. In particular, IRI and SN-38 combine with the DNA–topoisomerase I complex, thus forming Topo1-Irinotecan/SN-38-DNA ternary complex which is more stable. Subsequently, as the stabilized complex collides with the replication fork, the double strand of the DNA undwinds, triggering the apoptotic route which results in cellular death. To sum up, the anti-cancer effect of IRI is due to its interference with the DNA replication in cancer cells [101, 102]. After this sequence of actions, SN-38 is converted into its pharmacologically inactive form, SN-38G. This conversion happens in the liver and is catalysed by the UGT1A1 enzyme. Afterwards, IRI is mainly eliminated through liver metabolism and secretion. SN-38G can also be reactivated by BGUS, an enzyme of the intestinal tract. In this case the reactivated form is reabsorbed into the blood and induces diarrhoea (**Figure 3.12**). The chemical structure of lactone, its activated and its inactivated form are shown in **Figure 3.13**.

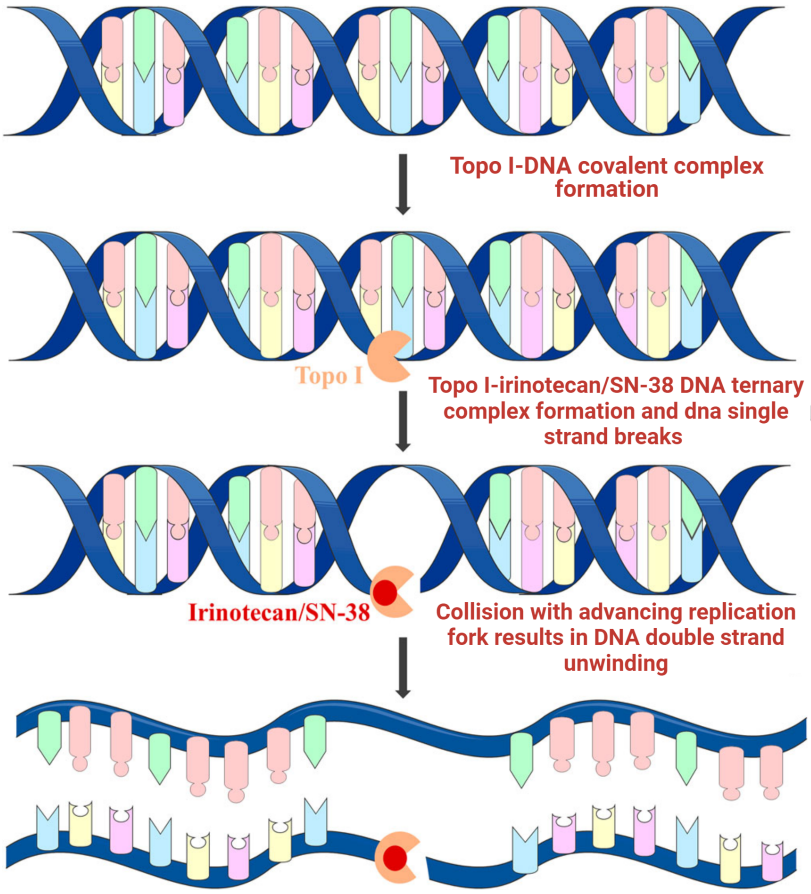

Figure 3.12: Mechanism of action of IRI as a topoisomerase inhibitor (retrieved from [101]).

[10]Pro-drug: a compound with little or no pharmacological activity that is converted into a pharmacologically active compound as soon as it is metabolized inside the body [99].

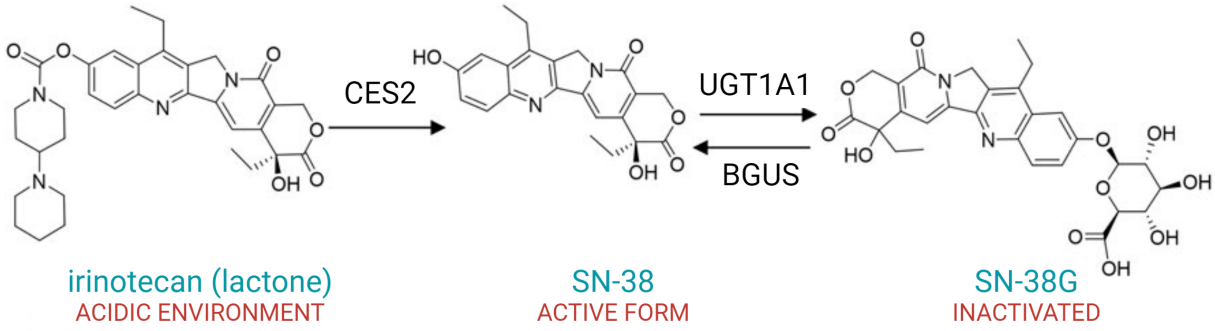

Figure 3.13: Chemical structure of the main chemical forms of IRI showing an anticancer effect. Lactone (left) is the most prevalent form in an acidic environment. Then, the catalytic action of the enzyme CES2 (carboxylesterase2) transforms it into the active metabolite SN-38 (centre). This can be inactivated into SN-38G (on the right) via the UGT1A1 hepatic enzyme. Finally, this inactivated form can be reconverted into the corresponding active metabolite via the BGUS enzyme (adapted from [101]).

IRI is usually administered via a continuous intravenous infusion for 30-90 minutes. Besides diarrhoea, another common side effect of this chemopharmaceutical is neutropenia[11] [103]. IRI can play a part in combination therapy, in order to improve its efficacy and reduce the adverse manifestations, resulting a more tolerable treatment. A triple therapy commonly including IRI is the 5-Fluorouracil + Irinotecan + Leucovorin (FOLFIRI) regimen.

During *in vitro* tests, two concentrations of IRI (*Irinotecan Accord 20 mg/mL, Accord Healthcare, Ireland*, **Figure 3.14**) were used : $[180\ mg/m^2]$ and $[275\ mg/m^2]$.

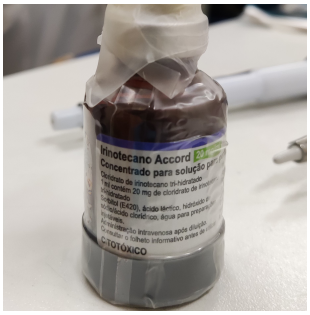

Figure 3.14: Irinotecan tested during this project (obtained through a special protocol between Biophysics Institute-FMUC-iCBR-cibb and CHUC).

3.2.4.3. Cyclophosphamide

Similarly to IRI, CFA is a pro-drug that enters the body as non-toxic and needs to be enzymatically activated into the active component phosphoramide mustard (PM) to exert its therapeutical benefit (chemical structures are in **Figure 3.15**).

The bioconversion of CFA into PM is believed to occur only in the liver rather than directly in cancer cells. CFA undergoes a cascade of reactions catalysed by hepatic enzymes: among

[11] Neutropenia is a condition characterized by an abnormally low level of neutrophils in the bloodstream. Neutrophils are a type of white blood cell that plays a critical role in the immune system's defense against infections.

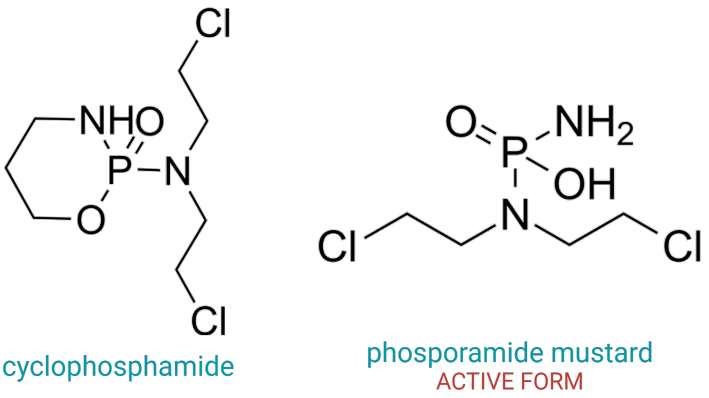

Figure 3.15: Chemical structure of Cyclophosphamide and its activated correspondent: phosporamide mustard (retrieved from [104, 105]).

intermediate products there are the isomers 4-hydroxycyclophosphamide (4OHCP) and aldophosphamide (ALDO). The first toxic product of this sequence is PM and, specifically, its protonated form, named protonated phosphoramide mustard (PM_{prot}). PM is an alkylating agent owing to 2-chloroethyl groups bonded to the central nitrogen atom, which leads to the intramolecular formation of a cyclic aziridinium ion. This cation has a strong electrophilic character; hence it is capable of strong interactions with DNA, establishing inter and intra-strand cross-linking. This modification hinders both DNA replication and gene transcription, inducing cell apopotosis. The reactions involving CFA produce many other secondary products, such as acrolein that is inactive but toxic [106, 107, 108].

Clinically, CFA is used in combinatory regimens to treat different kinds of cancer, including CRC. Its main adverse side effects are associated with bladder and gonadal toxicity. Other reported effects are haemorrhagic cystitis, amenorrhea, myelosuppression[12], alopecia, nausea and vomiting [109]. In the present study, CFA was used in the concentration $[1{,}000\ mg/m^2]$ (*ENDOXAN, 1 g, Baxter Médico Farmacêutica, Portugal*, **Figure 3.16**).

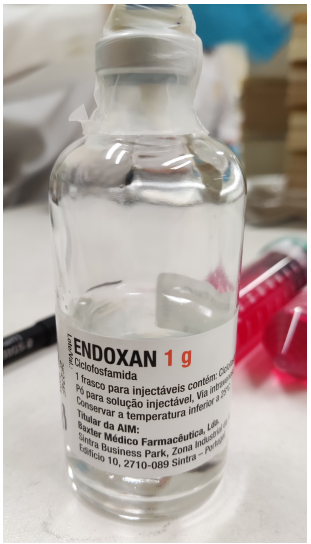

Figure 3.16: Cyclophosphamide tested during this project (obtained through a special protocol between Biophysics Institute-FMUC-iCBR-cibb and CHUC).

[12] Myelosuppression is the decreased ability of the bone marrow to produce blood cells.

Table 3.2: Tested protocols within the *in vitro* studies. All agents taking part in combination regimens were tested also as a monotherapy, to appraise their isolated effect as well. Some of the combinations therapies derive from previous studies performed by the group: protocols showing the most promising results were taken up again and the doses were reduced.

	PROTOCOL	PHARMACEUTICALS	GTE CONCENTRATIONS
(1)	5-FU+CFA	5-FU $[400\ mg/m^2]$ CFA $[1{,}000\ mg/m^2]$	GTE po $[0.5-5-10\ \mu g/mL]$
(2)	5-FU+CFA	5-FU $[550\ mg/m^2]$ CFA $[1{,}000\ mg/m^2]$	GTE po $[0.5-5-10\ \mu g/mL]$
(3)	5-FU+CFA	5-FU $[600\ mg/m^2]$ CFA $[1000\ mg/m^2]$	GTE po $[0.5-5-10\ \mu g/mL]$
(4)	FOLFIRI	5-FU $[400\ mg/m^2]$ IRI $[180\ mg/m^2]$	GTE po $[0.5-5-10\ \mu g/mL]$
(5)	IRI	IRI $[275\ mg/m^2]$	GTE po $[0.5-5\ \mu g/mL]$

3.2.4.4. Tested chemotherapy protocols

Chemotherapeutical protocols tested *in vitro* are the transposition of clinical protocols: the aim was to reproduce the clinical conditions happening in human treatment. Moreover, some of the tested protocols were chosen according to the results of prior studies done in the same research group [110]. Protocols showing up the most promising results were taken up again to try some dose reduction in combination with GTE. Details are given in **Table 3.2**.

3.2.5. Experimental protocol

As described in **subsection 3.2.2.6** (page 33), seeded WiDr cells were placed in the incubator for the adhesion time of 48 hours. By then, the actual *in vitro* assay begun. The used protocol had a total duration of seven days: the first task of each day was the CPOM observation of cell plates to monitor them. The overall organisation of the protocol was:

day 1: study initiation
day 1 to day 6: daily application of stimuli
day 7: MTT assay.

The scheme to be followed in each day was fully designed in advance, in order to calculate the specific amount of each component to be added to each well. The first two columns of each plate were planned as control columns, which means that only DMEM was added. On the other hand, the rest of the columns, were organized into duplets, being added medium, pharmaceuticals and (eventually) GTE po. The amount of medium to be added on the first day into each couple of columns was calculated to obtain, by the end of the study, a total volume of 450 $\mu L/well$. Moreover, the chemo-agents were applied only once, on the first day of study: their amount was calculated considering the area of each well, *i.e.* 0.95 cm^2. In fact, most of the used therapeutical

concentration in the clinics are expressed in mg/m^2. This project involved the evaluation of several protocols: an example of scheme to organize the plates is illustrated in **Figure 3.17**. The

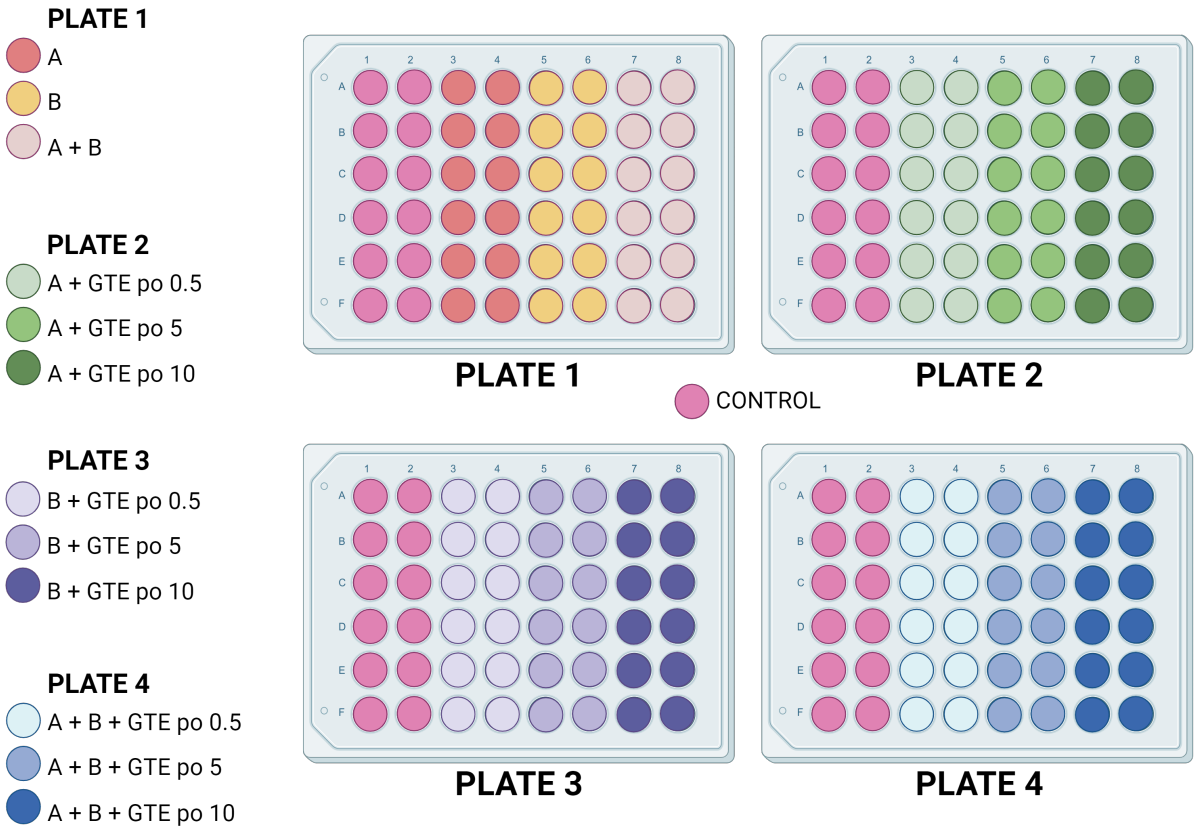

Figure 3.17: Example of the suddivision of the different pharmaceuticals combinations within four plates. A = first chemo agent; B = second chemoagent; GTE po concentration is expressed in $\mu g/ml$. Each study was designed in order to compare the action of an isolated agent A not only to the action of the conjugation A-GTE, but also to the action of the triplet A-B-GTE. (created with BioRender.com).

following sequence of steps, which is also represented in **Figure 3.18**, was carried out each day (for 6 days in a row) within the aseptic laminar flow chamber. After each daily manipulation, the plates were sealed with Scotch tape on their lids and returned to the incubator in described culture conditions (37° C, 95% H_2O, 5% CO_2).

Day 1: study initiation

First, the old medium (used during the 48 hours for adhesion) was retrieved from each well using a 1 mL pipette (*BioPette™ Plus, 1 000 µL*) coupled with sterile tips (*SARSTEDT AG & Co. KG, 70.3050, Germany*). The operator had the caution not to touch the bottom of the wells, to avoid scratching the adhered cells. Then the old medium was replaced with the previously calculated amount of new DMEM. Hence, the designated chemo pharmaceuticals were inserted in the wells and gently mixed with the DMEM by pipetting the liquid repeatedly.

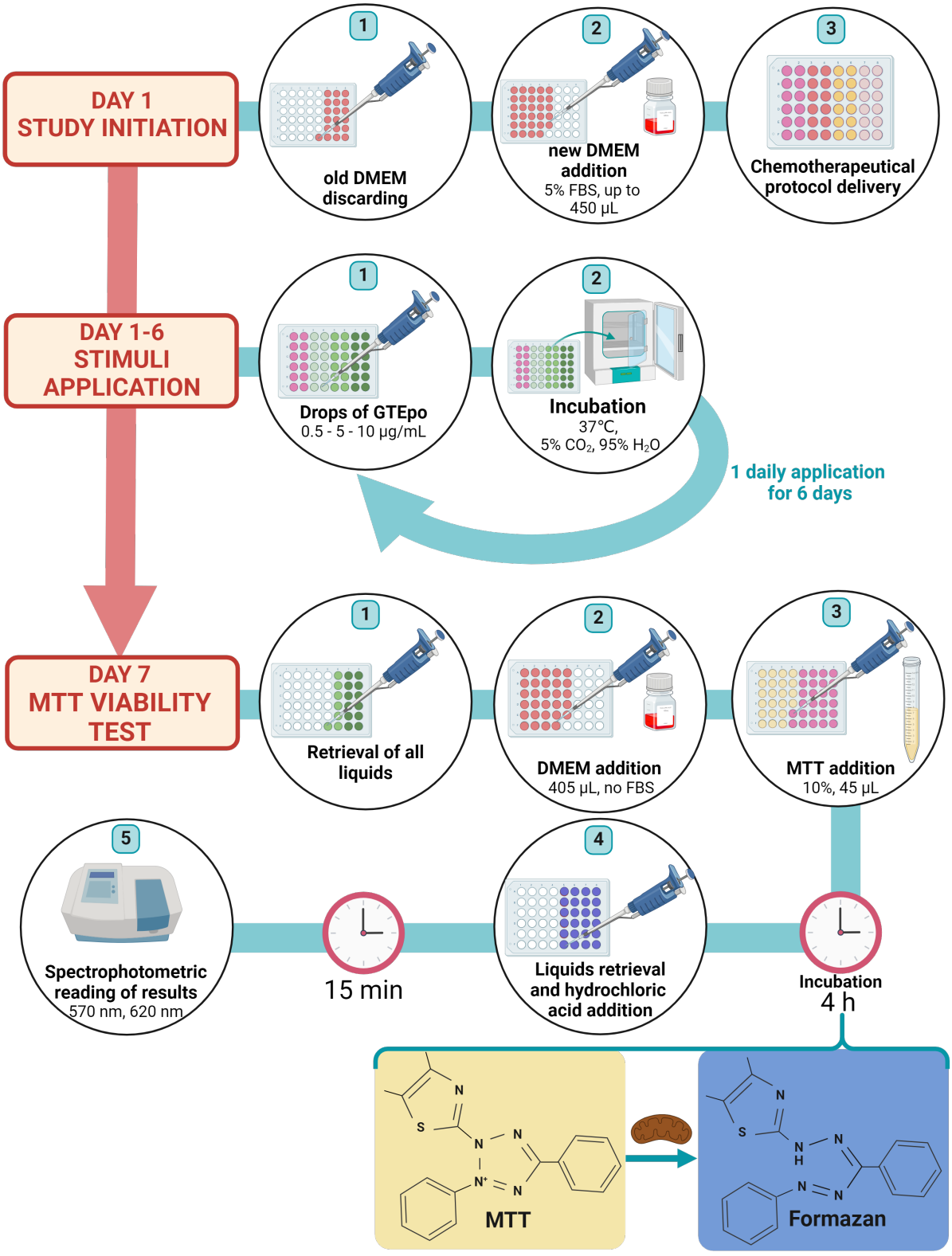

Figure 3.18: Sequence of tasks carried out within each step of the *in vitro* protocol (created with BioRender.com).

Day 1 to day 6: stimuli application

The stimuli application to cells, implied the daily supplement of GTE po in the three prepared different concentrations [0.5 – 5 – 10 $\mu g/mL$] to the previously wells. The GTE po administration frequency (1 application/day for 6 days) after a former research conducted performed in the same laboratory [111]. The cells were stimulated by carefully adding (pipetting) a designated volume of the GTE solution into each well. The solution was then gently mixed using pipetting to ensure homogeneity (uniform distribution throughout the well).

Day 7: MTT viability test

The procedure to be done during the seventh and final day of study, was the assessment of the cytotoxicity of the used chemo-agents, either isolated or coupled with GTE po. In this regard, the MTT test measures the effect of a drug on the growth of a population of cells and uses as endpoint the estimate of cell number [112]. MTT was selected as it uses metabolic activity as an indicator of cell viability and proliferation. The key reagent of this assay is 3-(4, 5-dimethylthiazolyl-2)-2, 5-diphenyltetrazolium bromide (MTT): a yellow mono-tetrazolium salt whose chemical structure contains a positively charged quaternary tetrazole ring [113]. When MTT is reduced, its chemical structure gets disrupted and the salt turns into formazan, a violet-blue water-insoluble molecule. MTT reagent has a positive charge and a lipophilic structure; therefore, it cross not only the cell membrane, but also the mitochondrial membranes [114]. Once inside the mitochondria, the reagent is enzymatically reduced by mithocondrial reductase to formazan by metabolically active cells. Hence, the MTT assay is connected to the chromogenic nature of MTT reduction. A colorimetric-based measurement is used to quantify the amount of intracellularly produced formazan, which is directly correlated to the intracellular metabolism [115]. A necessary step, prior to the quantification, is the solubilization of the formed formazan crystals [116]. In this work, this test was used to understand how much cytotoxic the tested protocols were: the higher the cytotoxicity, the lower the number of alive cells, the lower the amount of produced formazan. The practical method followed during MTT is composed of several steps (lower panel of **Figure 3.18**). Everything started in the laminar flow chamber.

1. **Removal of well's liquid content**: the mixture of DMEM, GTE po and chemo agents was carefully aspirated from each well using a 1 mL pipette.

2. **DMEM and MTT addition**: the volumes pippeted for each well were: 405 μL of DMEM without FBS (but supplemented with Pen/Strep) and 45 μL of MTT 10% (*Sigma, M2128, USA*); these quantities allowed to have 10% of reagent and 90% of medium.

3. **Incubation of the plates**: lasted 4 hours, to wait for the MTT intracellular reduction.

4. **Further removal of the well's content**: in this case a mixture of DMEM and MTT.

5. **Addition of solvent**: 450 μL of homemade acidified isopropanol[13], prepared by diluting

[13]Acidified isopropanol here was used as a solvent to favour the disruption of the membrane of viable cells, and the subsequent solubilization of formazan crystals.

37% of hydrochloric acid (*VWR Chemicals BDH Prolabo®, 20255.420, 2.5L, Belgium*) into isopropanol (*Honeywell Riedel-de Haën™, 33539, 2L, France*) were added to each plate.

6. **Solubilization of formazan crystals**: 15 minutes post solvent's addition. It was necessary to let the solvent work, while plates were protected from light (as MTT reagent is photosensitive).

7. **Spectrophotometric reading**: a microplate reader (*BioTek®, SynergyTM HT, USA*), coupled to the interface Gen5 BioTek® (*BioTek®, SynergyTM HT, USA*) installed in a PC was used. This reading measures the optical density (OD) to quantify the decrease of the light transmission due to the homogenized MTT-formazan solution. The reading was done at 570 *nm* and 620 *nm* wavelengths, due to the wavelength at which the MTT-derived formazan has its absorbance peak [115].

To conclude, the measured OD values were assumed to be a representation of formazan concentration and consequently the intracellular reduction of MTT.

3.3. Results and discussion

The MTT assay data was rigorously analyzed using statistical methods to assess the cytotoxicity of the tested protocols over WiDr cells. The MTT data underwent a three-step process: first, it was organized, pre-processed, and standardized to ensure consistency. Second, it was submitted to specific statistical analysis to identify meaningful patterns. Finally, the results were visualized using boxplots, which effectively displayed the distribution of data across the different protocols. Three softwares were used: Microsoft Excel® (*Version 2402 Build 16.0.17328.2012*), MATLAB (*Version: 9.12.0.1884302, R2022a*) and Rstudio (*Version 4.3.1*).

3.3.1. Data pre-processing and standardisation

The MTT data was first uploaded to spreadsheets. To identify and remove potential outliers, the MATLAB function `isoutlier` was used. This function analyzed each well column and flagged data points exceeding 3 times the median absolute deviation (MAD) from the median as outliers. These outliers were subsequently excluded from the analysis [117].
As previously described (**section 3.2.5**, page 40) the first two columns of each plate were not exposed to the experimental treatment, thus being controls. This cell group was used as a baseline. These cells displayed normal behaviour and growth rate, allowing for a comparison with the effects of treatment on other cell groups, as both control and experimental groups were cultured within the same conditions during the overall experiment. To strengthen the study's reliability (robustness), each treatment combination was tested three times ($n = 3$) using a total of 36 wells (12 per plate). Ideally, these triplicate experiments should have been performed on the same day and in the same assay to minimize variation. However, this was not feasible for all studies. As a result, several factors could potentially induce group inconsistencies: I. cells were not

plated simultaneously across all replicates; II. cells may have originated from different mother flasks; III. different assays might have begun during different cell cycle stages. These variations could have introduced external influences and affected the homogeneity of the cell groups. Therefore, the control group was an important standardization tool to allow the comparison between different groups, aiming to minimize variation within each group and improve data consistency. The MTT data point (MTT_{well}) for each non-control well was normalized using the following standard formula :

$$MTT_{standard} = \frac{MTT_{well}}{AVG_{control}} \tag{3.3}$$

... where, $AVG_{control}$ is the average of the MTT data obtained from the control wells of the same plate. According to $MTT_{standard}$ value, two different conclusions can be drawn:

- $MTT_{standard} > 1$: the tested combination does not show cytotoxicity towards WiDr cells;
- $MTT_{standard} < 1$: the tested compound interferes with WiDr cells death, by decreasing the number of viable cells per each well.

3.3.2. Statistical tests

The subsequent step was the statistical analysis of MTT results. To fulfil this task, two statistical tests were applied: the *Kruskal Wallis test* and the *Mann-Whitney test* (also known as *Wilcoxon Rank Sum test*). They are both non-parametric tests[14], being well suited for analysing small datasets (in this study $n_{tot} = 36$ samples per group). Unlike parametric tests that rely on specific data distributions (*e.g.* normal distribution), non-parametric tests focus on comparing the medians (centermost values) of different groups. By analyzing medians, non-parametric tests can effectively determine if the data in each group originates from the same underlying distribution, regardless of the specific shape of that distribution [118]. *Kruskal-Wallis* test is analogous to one-way analysis of variance (ANOVA). It replaces ANOVA when data show a non-normal distribution and it is useful to compare two or more independent groups. The further prerequisites for its application are: a minimum of 5 observations for each group and data coming from independent samples, belonging to groups unrelated to each other. Herein, the present study fulfilled these requirements, since each well was independent from the others. In fact, during all manipulations, pipette tips had obviously to be changed for each well or for each group (according to the procedure), to avoid the mixture/possible contamination between different wells or groups. Hence, even if a plate came from the same cell culture, the cells in each well grew independently one from another. The null hypothesis (H_0) of *Kruskal-Wallis* test is that the group medians are equal. On the other hand, the alternative hypothesis (H_1) is: at least the median of a group is different from the others. Hence, if the null hypothesis is rejected, it means that the tested groups come from different distributions [119].
Unlike *Kruskal-Wallis*, *Mann-Whitney test*, also known as Mann-Whitney U test, is ideal to compare only two groups. It can be used when there is reason to believe that the data are

[14] Non-parametric test: it assumes that there is not a specific distribution underlying data

not normally distributed and variances between the two groups are not homogeneous [120]. It establishes the null hypothesis (H_0) that two groups are equal and the alternative hypothesis (H_1) is that the groups are not equal.
For both tests, ($\alpha = 0.05$) was set as significancy level (CI = 95%). It means that 0.05 was the threshold to determine whether the differences between different groups could be regarded as statistically significant: a p-value lower than 0.05 lead to the discard of the null hypothesis. Thus, through these analyses, it was possible to appraise whether the compared combinations of chemo-agents showed relevant differences in terms of their effect to cell viability. To be precise, each comparison involved not only the comparison between isolated agents and combined agents, but above all between agents alone and agents coupled with GTE po.

3.3.3. Boxplots examination

Boxplots were selected as the most immediate graphical representation of statistical analysis outcomes. It should be reminded that each well contained 5.8×10^3 *cells* and that GTE po was applied daily during 6 days (6 applications). All figures will be analysed within the subsequent subsections: the left panel of each graph corresponds to a group to which GTE was not delivered. There are other important elements to be considered to analyse each boxplot: each graph shows two horizontal dashed lines, representing drug-response metrics.

- Standardization line (**red**): it represents the control group, where cell growth is not inhibited. It serves as a benchmark ($y = 1$) for evaluating the effectiveness of other protocols against WiDr cells. For a protocol to be considered inhibitory, the median growth in the treated group must be lower than this threshold.
- IC_{50} (**green**): researchers use it in experiments with cells to see the efficacy of a drug, and how they are killed by it [121]. An IC_{50} value corresponds to the concentration of the drug that kills half the cells. It is shown on the graph at the point where the line crosses the y-axis at 0.5. Hence, if the middle value (median) of a group falls below this line, it means that more than half the cells were killed by the treatment [122].

To sum up, the worst result according to the expectations would have been a boxplot around $y = 1$ (*i.e.* pharmaceutical protocol with no effect). The last detail to be mentioned about subsequent figures, is the presence of the symbols *, ** and ***. Each of them identifies a different statistical significance: $p < 0.05$, $p < 0.005$ and $p < 0.001$, respectively.

3.3.3.1. Protocol: 5-FU + CFA

This combination was tested with three concentrations of 5-FU [123]: $[400 - 550 - 600 mg/m^2]$. First, the conjugation CFA + GTE po (**Figure 3.19**), induces a statistically significant improvement of cytotoxity: the comparison with the control group with the *Mann-Whitney test* results for p-values: 0.02954, 0.02048 and 0.001061 for [0.5–5–10 $\mu g/mL$] GTE po, respectively. Even though there is a statistically significant difference, it is not very meaningful for the present

study, as all three groups have boxplots beyond the line at $y = 1$. This line represents no effect on the cells. Hence, the drug, whether alone or combined with GTE po, does not seem to have a clear impact on WiDr cells The explanation underlying this could due to the fact that CFA is a pro-drug. Actually, it needs to be activated by hepatic enzymes, which are obviously absent in the simplified *in vitro* setting. Anyway, the highest concentration of GTE po is the one showing the best results. This could be due to the action of GT, which makes cells more susceptible to the weak cytotoxicity of CFA.
On the other hand, the effect of 5-FU (**Figure 3.19**) gave different results. The cocktail conjugation 5-FU + GTE po does not enhance, but lowers the cytotoxicity. Despite this reduction, all boxplots remain below the IC_{50} line. The addition of GTE po to 5-FU still kills more than 50% of cells. 5-FU is an antimetabolite that hinders the DNA biosynthesis causing cell death. While this can be effective in treating cancer, it also causes serious side effects. These results might not be statistically significant but clinically very important for those patients with severe adverse drug effects [124].
Finally, the cocktail 5-FU + CFA shows different results according to 5-FU concentrations:

- **Figure 3.19a**: 5-FU $[400 mg/m^2]$ + CFA cocktail, together with GTE po shows goods results, keeping cytotoxicity statistically like the action of 5-FU + GT.
- **Figure 3.19b**: 5-FU $[550 mg/m^2]$ + CFA + GTE po is the best protocol amongst the three. In fact, the addition of GTE po keeps the cytotoxicity of the pharmaceutical cocktail unaltered. There is no statistical difference between any concentrations of GTE if added to this combination. Nonetheless, the boxplots of 5-FU $[550 mg/m^2]$ + CFA + GTE po are always the lowest in **Figure 3.20b**.
- **Figure 3.20a**: 5-FU $[600 mg/m^2]$ + CFA is the most cytotoxic cocktail; however, the coupling with GT is not relevant, as the values increase and come close to the IC_{50} line.

In most of the cases, the coupling of CFA and 5-FU does not show a statistically relevant difference from the cytotoxicity of isolated 5-FU. This suggests that *in vitro* the main cytotoxic action is due to 5-FU, which does not need enzymatic activation to exert its effect against DNA biosynthesis. However, if translated in the clinical context, these results could show that GTE po does not interfere with the cocktail pharmacological effects too much. Indeed it can compensate, through its multiple benefits, the secondary effects of the cocktail, thus improving patients' quality of life. It can be finally noticed that a higher dose of 5-FU $[600\, mg/m^2]$ was not the best option. Nevertheless it is used in the clinic, hence the reports that high doses can be useless in terms of effectiveness and dangerous in terms of toxicity [125].

3.3.3.2. Protocol: IRI

According to the clinical recommendations, IRI should be administered in a monotherapy regimen as first-line therapy for the rare patients who cannot tolerate 5-FU [126]. In this case, the recommended dose is $350\, mg/m^2$: in case of adverse events, it is suggested to reduce it [103]. Herein, the monotherapy regimen was tested in a previous study with a slightly reduced

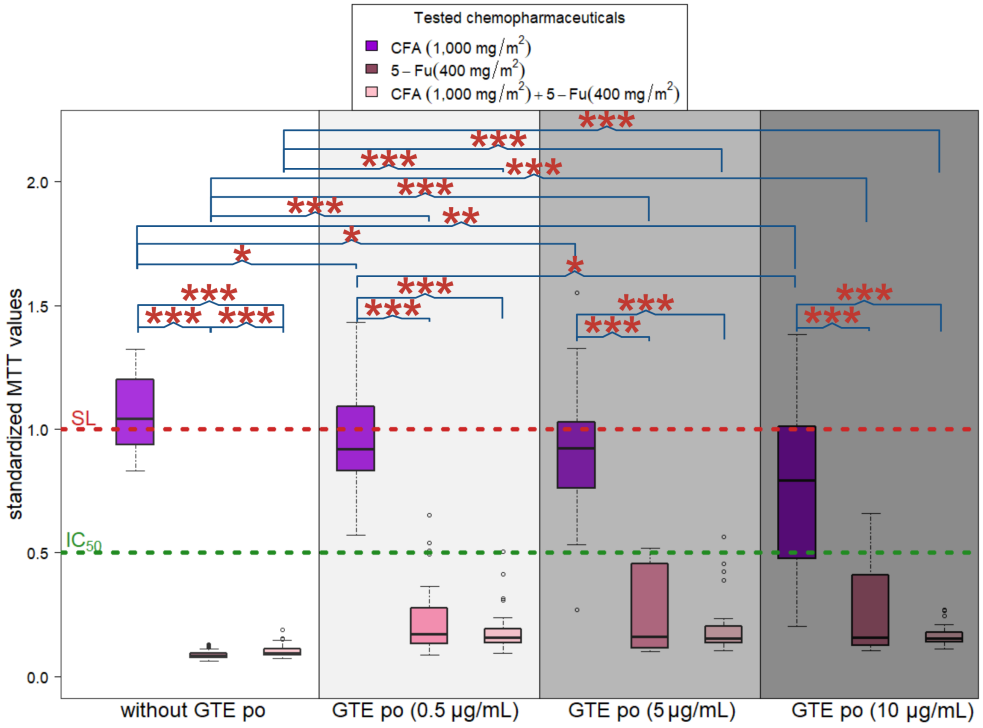

(a) CFA $(1{,}000 mg/m^2)$; 5-FU $(400 mg/m^2)$; CFA $(1{,}000 mg/m^2)$+5-FU $(400 mg/m^2)$. This combination was tested with GTE po, at 0.5 - 5 - 10 $\mu g/mL$ concentrations.

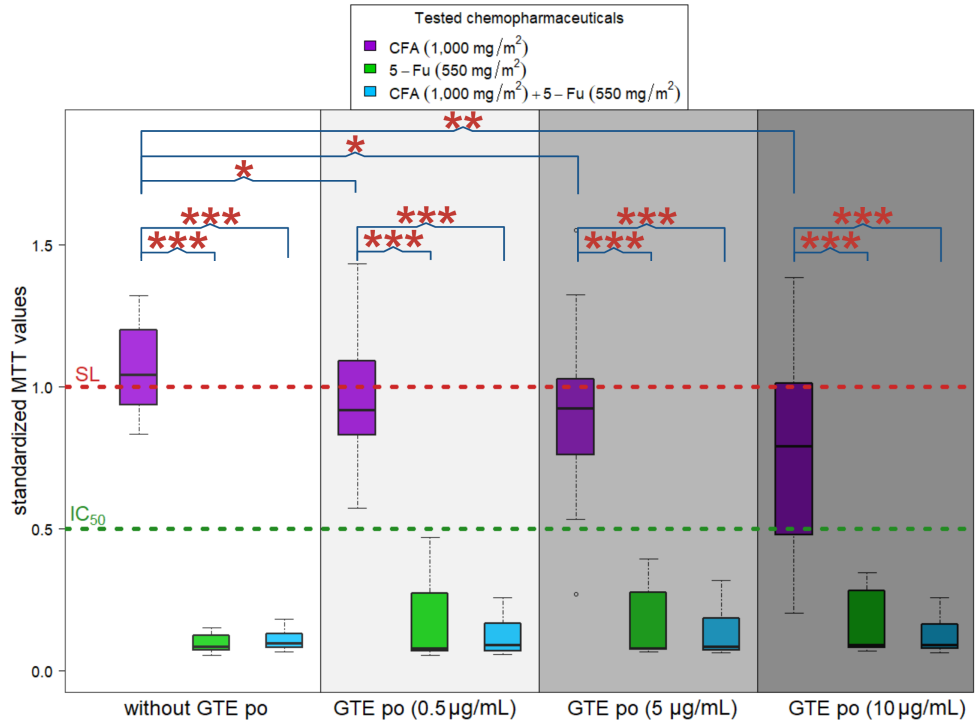

(b) CFA $(1{,}000\, mg/m^2)$; 5-FU $(550\, mg/m^2)$; CFA $(1{,}000\, mg/m^2)$ +5-FU $(550\, mg/m^2)$. This combination was tested with GTE po, at 0.5 - 5 - 10 $\mu g/mL$ concentrations.

Figure 3.19: Results obtained with 5-FU+CFA combination, with and without GTE po, for WiDr cells; * p-value < 0.05; ** p-value < 0.005 *** p-value < 0.001.

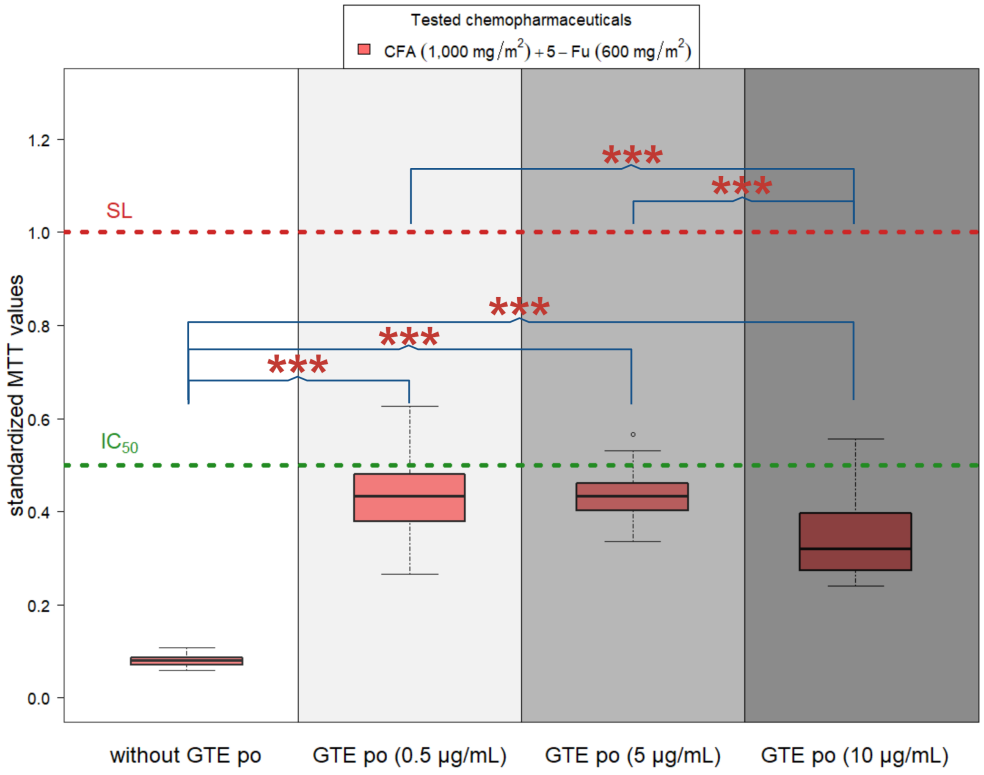

(a) CFA $(1{,}000\,mg/m^2)$ + 5-FU $(600\,mg/m^2)$. This combination was tested with GTE po, at 0.5 - 5 - 10 $\mu g/mL$ concentrations.

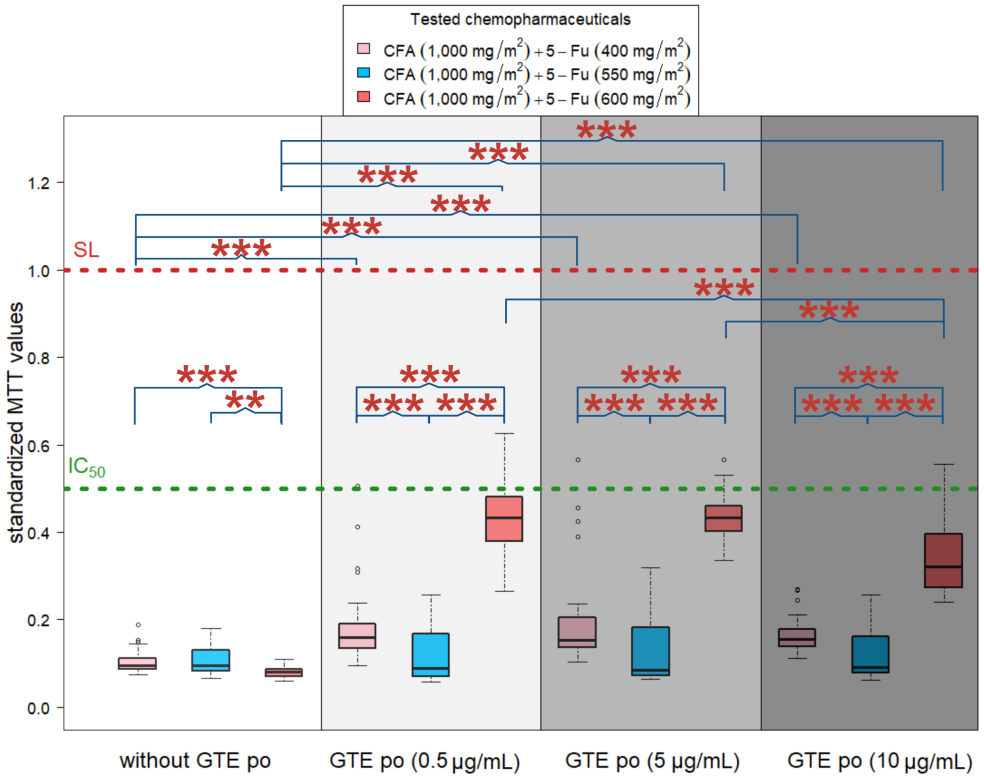

(b) Ensemble of results obtained for the combination of the three different concentrations of 5-FU $400-550-600\,mg/m^2$, with green tea

Figure 3.20: Results obtained with 5-FU + CFA combination, with and without GTE po, for WiDr cells; * p-value < 0.05; ** p-value < 0.005 *** p-value < 0.001.

dose $[325\,mg/m^2]$ [110]. Since results were promising for the conjugation made of IRI and the lower concentrations $[0.5-5\ \mu g/mL]$ of GTE po, it was decided to test a further reduced dose of this pharmaceutical: $[275\,mg/m^2]$. According to the previous results, only the 0.5 and 5 $\mu g/mL$ concentrations were evaluated. **Figure 3.21a** shows the boxplots for this IRI concentration. Both the *Kruskal-Wallis* and the *Mann-Whitney* test revealed that there is not a statistically significant difference between the cytotoxicity of isolated IRI and its combination with GTE po (the p-value of *Kruskal-Wallis* was 0.9199, while the lowest p-value of the *Mann-Withney* test was 0.6064). In fact, the three tested combinations stay clearly below the IC_{50} line, showing the ability of this concentration of IRI (both alone and coupled with GTE) of inducing the death of more than half of the cells. This is encouraging, since it could mean that the chemo-agent does not interfere with the natural compound effect and vice-versa, being an appreciable dose reduction. Clinically this could mean an improvement of patient's quality of life. To further evaluate these results, **Figure 3.21b** summarizes the action of IRI $[275\,mg/m^2]$ as compared to IRI $[180\,mg/m^2]$ (which was included in the subsequent protocol). The *Mann-Whitney* test proved that there is a statistically relevant difference between the two tested concentrations if coupled with GTE po $[5\,\mu g/mL]$ (p-value = 0.002721). IRI is a pro-drug: hence, it cannot fully express its action *in vitro*, where there are not the organs responsible for its enzymatic activation. Anyway, WiDr cells have the tendency of agglomerating, thus forming a small tumoral tissue *in vitro*. This small tissue can activate IRI into its active product: SN-38, whose outcome is cell apoptosis induction [127]. This could explain why IRI, differently from CFA, shows a clear cytotoxic effect.

3.3.3.3. Protocol: FOLFIRI

FOLFIRI is a common chemotherapy regimen for the therapy of CRC consisting in a cocktail of three drugs: 5-FU, IRI and Leucovorin (LV). It is clinically implemented as it allows to obtain a significant improvement in terms of response rate with regarding a single agent treatment with 5-FU [128]. The *in vitro* test involved the combination only of 5-FU and IRI, whereas LV will be used *in vivo*. The chosen concentrations where the ones used in the clinic: $[400\,mg/m^2]$ for 5-FU and $[180\,mg/m^2]$ for IRI [129]. The boxplots of the results are shown in **Figure 3.22**. The *Kruskal-Wallis* test showed that, in general, there is a difference between the tested groups ($p-value < 2.2\times10^{16}$).

At a glance, it can be noticed that, despite the conjugation with GTE po slightly decreased the cytotoxicity, both the action of the isolated agents and of the cocktail remained far below the IC_{50} line. There is a statistically significant improvement of cytotoxicity starting from the isolated effect of IRI to 5-FU and ending into the FOLFIRI cocktail. This happened with all GTE po concentrations (p-values 0.005413, $2.287\cdot10^{-5}$ and 0.001038 for $[0.5–5-10\ \mu g/mL]$ respectively, by the *Mann-Whitney* test). Even if there are not statistical differences between isolated 5-FU and FOLFIRI, the boxplots corresponding to 5-FU are dispersed, compared to the narrow FOLFIRI boxplots. This may be explain the absence of statistical relevance, but might also confirm that the use of the cocktail is successful, since it induced a more homogeneous

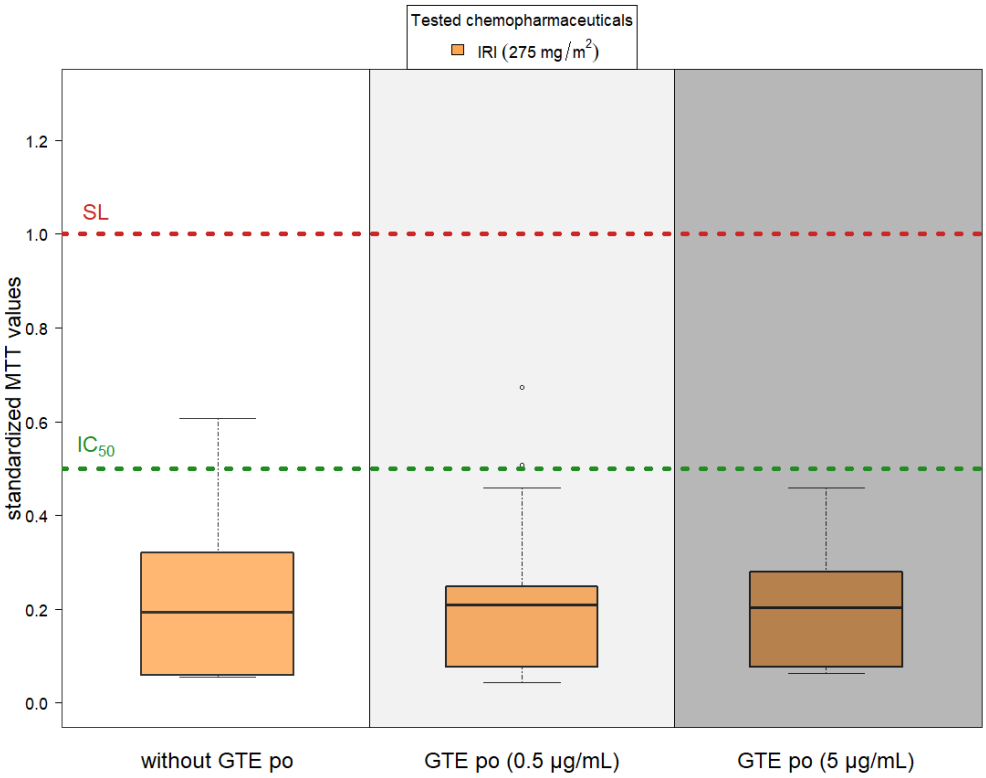

(a) IRI 275 mg/m^2. This combination was tested with GTE po, at 0.5-5 $\mu g/mL$ concentrations.

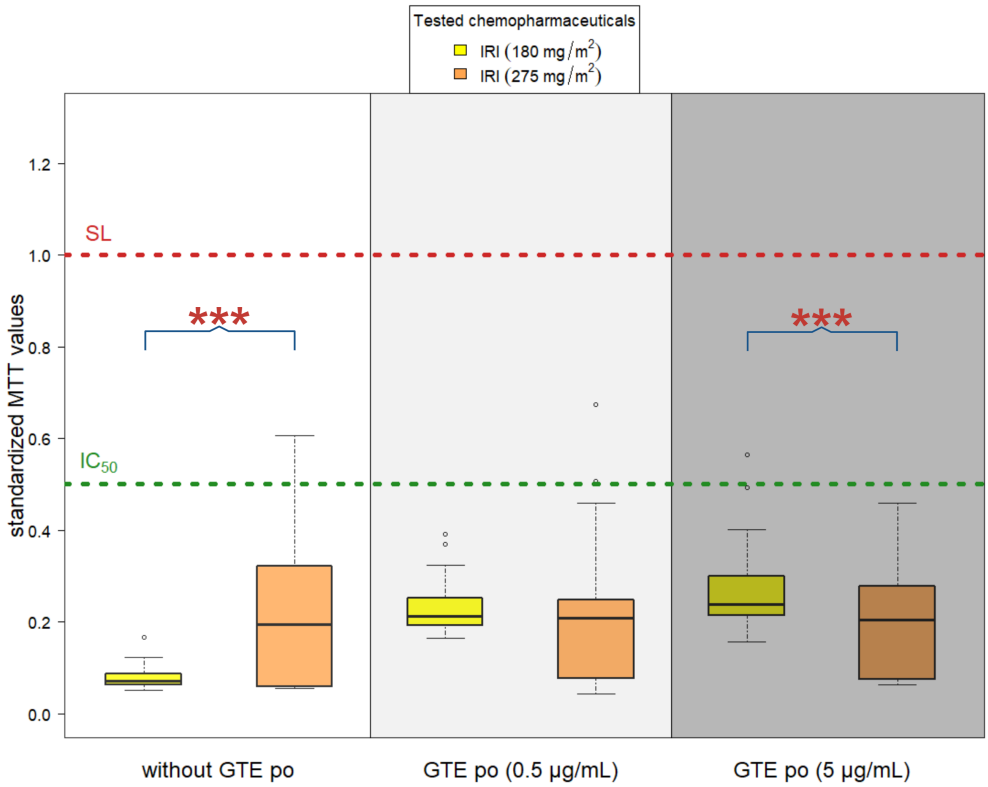

(b) Comparison between IRI 275 mg/m^2 and IRI 180 mg/m^2.

Figure 3.21: Results obtained with isolated IRI, with and without GTE po; * p-value < 0.05; ** p-value < 0.005 *** p-value < 0.001.

effect towards the malignant cells. Moreover, the GTE action is better expressed over the cocktail (narrower boxplots) rather than for isolated 5-FU (more dispersed boxplots).

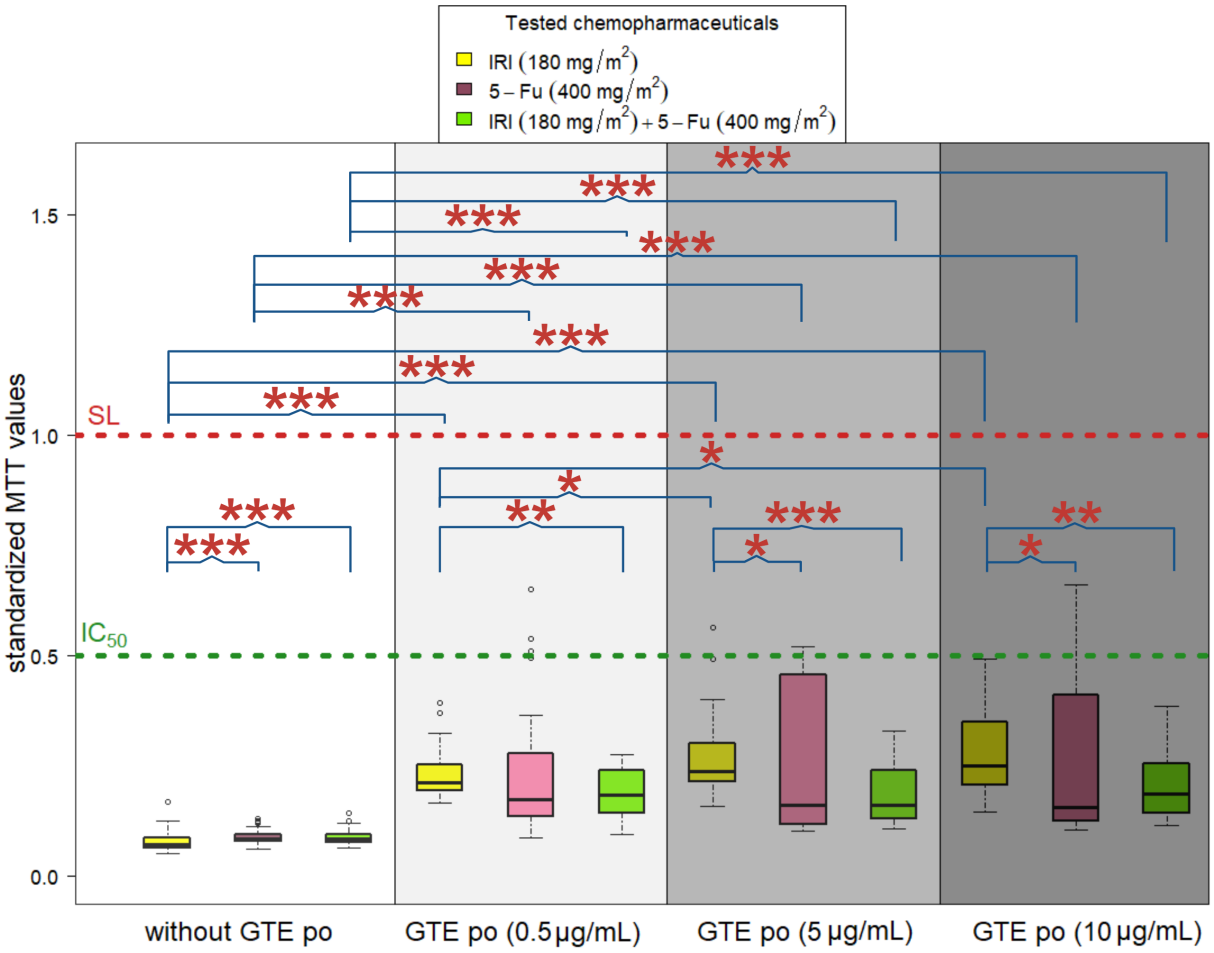

Figure 3.22: Results obtained with IRI $[180 mg/m^2]$ + 5-FU $[400 mg/m^2]$ combination, with and without GTE po, used in all three available concentrations. * p-value < 0.05; ** p-value < 0.005 *** p-value < 0.001.

3.3.3.4. Final considerations

A comprehensive evaluation of the results allows for the formulation of key observations. The shape of the obtained boxplots confirms the non-normality of data, since most of them are asymmetric. This asymmetry is not attributable to outliers, as they were discarded in the pre-processing. Furthermore, some boxplots are wider: they represent more dispersed and, therefore, heterogeneous data. This could be ascribed to the fact that not all plates, and therefore not all wells, contained cells coming from the same culture flask. In other words, all assays where not synchronous and could have started with cells in different stages of the cell cycle. Standardization would not fully eliminate this variation, as not all cells in a population are in the same cycle phase. Moreover, other sources of variability come from human error and the imprecision of tools. Another important remark is about what does MTT read. In fact, it also reads the formazan deriving from the reduction of the reagent happening in mitochondria outside cells (who have already died). Additionally, it was demonstrated that MTT results are not only influenced by cell

viability, but also by a sum of several factors, like cell growth phase and the rate of MTT uptake and formazan extrusion that all could be potentially conditioned by the tested treatment [115]. MTT does not give information on the type of cell death, nor of the cell cycle phase they are at the moment of the experiment. Cytometry studies should be done concomitantly, however, due to several factors (number of WiDr cells, reagents, and equipment availability) researchers mainly do them only for the best assays with MTT. It is noteworthy that GTE's cytotoxicity appears to be selective for WiDr cancer cells

Furthermore, it must be pointed out that it is right to speak about cytotoxicity of GTE only with respect to cancer cells. In fact, it was already shown in a previous study that, unlike chemodrugs, doses of GTE in this range do not induce normal colon cells death (*CCN 841, ATCC®*) [91]. Finally, while GTE po may not have significantly boosted the effectiveness of most treatment protocols, it importantly did not counteract the action of the chemotherapy drugs. Considering the known positive effects of GTE on the human body, this suggests potential for GTE po to be a valuable tool in mitigating the side effects of chemotherapy, improving patient's quality of life.

4 In vivo studies

4.1. General aim

In vitro studies are a valuable tool in oncological research. Specifically, in this study, they allowed insights into how WiDr cells responded to the coupling of GT with clinically approved drugs in a controlled and isolated environment. While the initial cell-based experiments (*in vitro*) were promising, the next step was to understand how these treatments would interact with the body (*in vivo*). Unlike a flask or a cell plate, the body presents a complex environment. To bridge this gap, researchers use animal models, specifically mice. This approach allows to recreate some aspects of human disease and assess the drug combinations' overall impact, including safety, metabolism, and effectiveness [130].

Rodent models are a widespread and helpful tool in cancer research: mice are small, easy to handle and house, reproduce quickly, and are cost-effective [131]. Nevertheless, what makes them so appealing for pre-clinical studies are their genetic features. Some studies performed a whole-genome comparison between humans and mice, revealing that the human genome size (2.9 Gb) is approximately 14% bigger than the mouse genome (2.5 Gb). However, the most interesting finding is that the gene content and its linear organization along the chromosomes in mice are highly similar to those in humans. Mice share 95% of their genes with humans [132, 133]. Given these considerations, mice were chosen as the animal model for this study.

Before delving into detail, it is essential to address some ethical premises and considerations, as the use of animals for research purposes is a topic of concern. Animal research in the European Union (EU) is regulated under specific legislation (Directive 2010/63/EU), which mandates proper scientific justification before conducting animal trials. Furthermore, this directive requires implementation of the 3**R**s principles:

1. **R**educe the number of tested animals to a necessary minimum, while ensuring scientifically reliable results;
2. **R**eplace animals by non-animal models (if possible);
3. **R**efine practices to reduce the burden on animals (in terms of pain, suffering, and lasting harm) [134].

These guidelines were duly followed in the present work, and the measures taken to this purpose will be listed in the following paragraph. Additionally, all procedures were implemented in accordance with Portuguese legislation (Law-Decree 113/2013) and the Animal Welfare Body of iCBR (ORBEAs 17/2015 and 12/2021).
Given these premises, the aims of the *in vivo* experiments were:

- the inoculation of WiDr cells into mice and the evaluation of tumuor mass progression using traditional measurement methods;
- assessment of the effective metabolic activity of the tumour mass by PET imaging after a preliminary evaluation of the acquisition system;
- evaluation of the animals' response to the different administered protocols, including GT.

4.2. Materials and Methods

This section will describe the protocols used during the *in vivo* studies, with particular attention to detailing the specific PET imaging method employed.

4.2.1. Animal model

To mimic the human disease and to reproduce the tumour microenvironment, BALB/c nude (BALB/c(-)) male mice were chosen as animal model (**Figure 4.1**). The male gender was selected based on CRC epidemiology, which suggests that the studied disease is more prevalent among men (see **subsection 2.1.4**, page 11).
BALB/c(-) mice are widely used in cancer research as they can host human tumour growth without rejecting it due to host versus graft rejection [135]. They lack a functioning thymus[1], leading to a deficiency of immune T-cells. This enables the engraftment and growth of human implanted cancer cells. Another notable macroscopic trait of BALB/c(-) mice is the apparent absence of hair, hence the term 'nude'. Actually, their skin at birth contains normal hair follicles, but as hair grows, they are unable to penetrate the epidermis [137]. This characteristic is due to a spontaneous genetic mutation occurring in the locus of the FoxN1 (Forkhead box) gene, located on chromosome 11, which encodes transcription factors. The experimental model used in this study was a non-orthotopic[2] cell line-derived xenograft (CDX), *i.e.*, cells from the WiDr cell line cultured *in vitro* were inoculated subcutaneously into immunodeficient mice. This approach has two advantages. First, the lack of hair on these mice makes it easy to check the tumour growth. Second, thanks to the subcutaneous (s.c.) injection, researchers can easily monitor them [139, 140].
The age of the mice used varied between 2 and 4 months and they were supplied by the *Vivarium* of the Institute of Clinical and Biomedical Research (iCBR) of the Faculty of Medicine of the

[1] Thymus is a fundamental gland of the immune system responsible for the production and maturation of immune cells, such as T-cells, which play a crucial role in protecting the body from foreign antigens [136].

[2] In an orthotopic xenograft the grafted tumour grows into the equivalent organ from which the cancer originated in the human [138].

University of Coimbra, which is licensed and compliant with national legislation regarding animal experimentation. To ensure Refinement, animals were maintained under carefully controlled conditions. They were housed in cages, which were periodically changed and disinfected, with bedding consisting of sterilized corn cob and enriched with playful material. Each cage provided sterilized food and water *ad libitum*. In the *Vivarium*, they were housed in special racks to ensure ventilation of each cage. The surrounding temperature was maintained between 24 and 28° C, with air humidity between 40 and 60%, and and circadian light/dark cycle. Furthermore, all animal manipulations were done in a calm and sanitized environment using sterile equipment by licensed and trained personnel. To comply with the Reduction rule, only ten animals were used, as the study's design allowed for an appropriate estimation of the necessary number of animals. A sequence of the main steps of the animal protocol is illustrated in **Figure 4.2**.

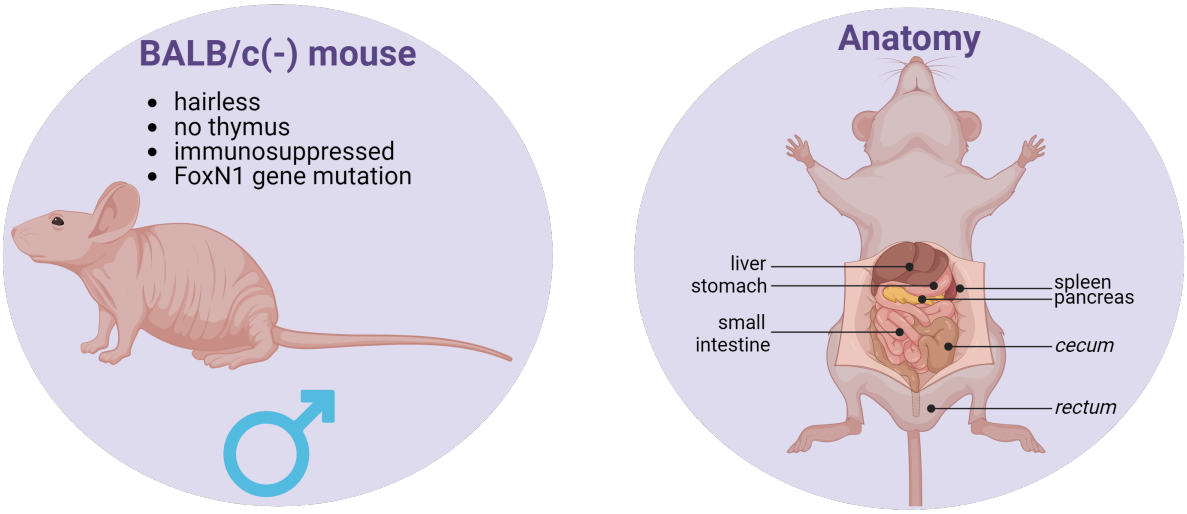

Figure 4.1: Illustration of a BALB/c nude mice, highlighting the main anatomical elements of its digestive system (created with BioRender.com).

4.2.1.1. WiDr cell inoculation

The WiDr cells to be injected into the mouse were similar to those used for the *in vitro* studies. WiDr cells were cultured following the previously described protocol (**section 3.2**, page 19). After being detached and resuspended (**subsection 3.2.2.4**, page 28), they were counted (**subsection 3.2.2.5**, page 29) to obtain between $1.5 - 2.5 \times 10^6$ cells to inject per animal. This number of cells was chosen based on the literature [141] and previous studies done within the same group. It is crucial to establish the appropriate number of cells to maximize the probability of successful xenograft growth. In fact, all inoculated animals developed tumours as expected. Therefore, while remaining in the laminar flow chamber, a specific volume of cell suspension (usually around 0.2 *mL*, obtained with **equation 3.1**, on page 33) was drawn into a 1 *mL* syringe (*Pic Solution Syringe, U-100 insulin, 1608022, Italy*) coupled to a 25G needle (*Pic Solution, 0,5×16 mm, 25 G5/8", 1811371, Italy*).

In a room dedicated to animal manipulations, the mouse was placed in a prone position and carefully secured to allow exposure of the right thigh, where the WiDr cells were injected

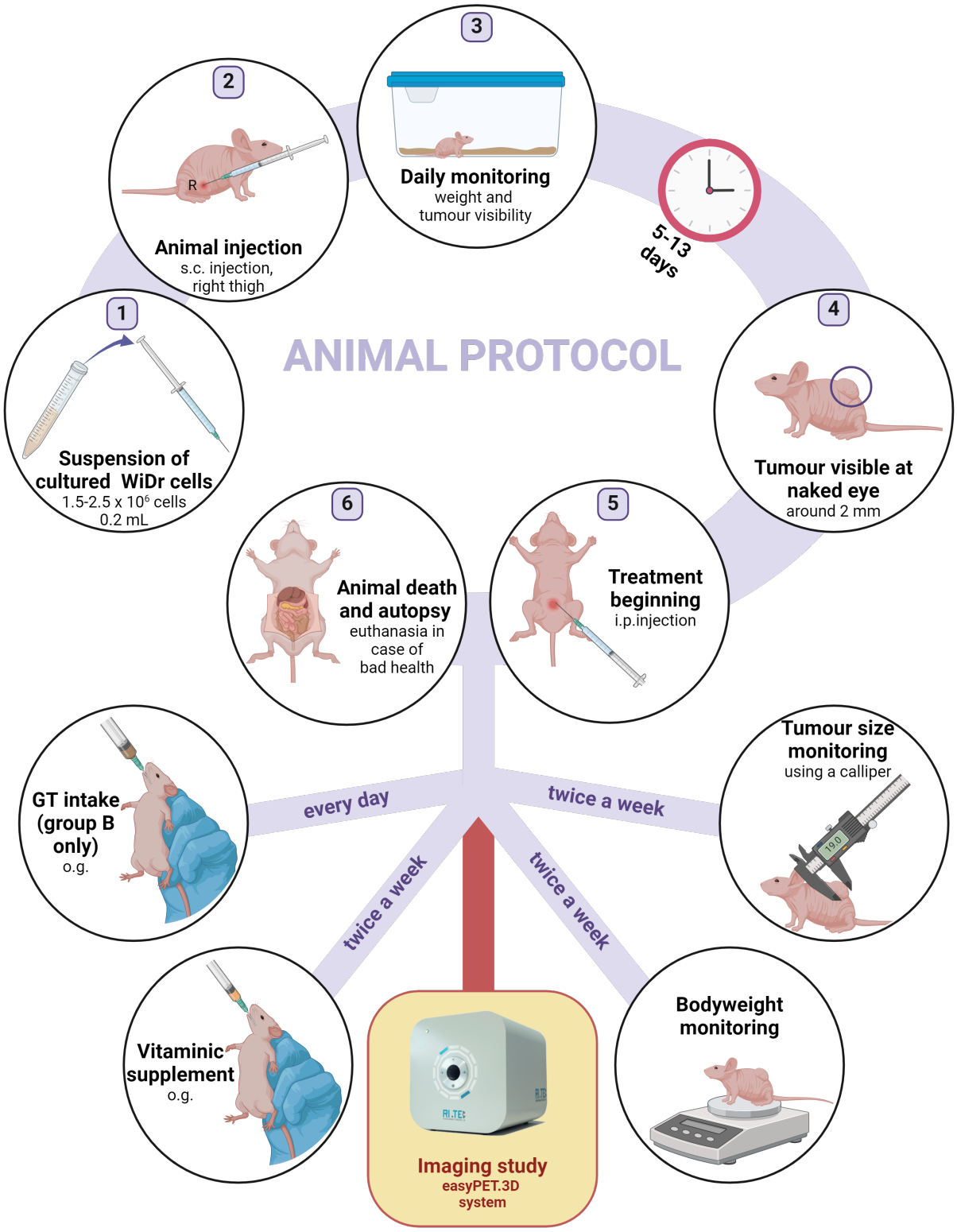

Figure 4.2: Main steps carried out during the animal experimental study. The tasks reported in the lower half of the illustration were done repeatedly, with a specific frequency (created with BioRender.com).

subcutaneously. As depicted in **Figure 4.3**, the operator inserted the needle from the top downwards, keeping the syringe bevel facing himself to exert less pressure and create a s.c. pocket. It was crucial to insert the needle gently to avoid reaching the muscle fascia, could lead to tumour dissemination through a blood vessel. After the injection, the animal was monitored daily to assess its well-being and the presence of a visible tumour mass near the injection site. Additionally, its weight was recorded using a Seca scale (*Seca, model 734, series 1/1, Germany*), and a photographic record was created (twice a week).

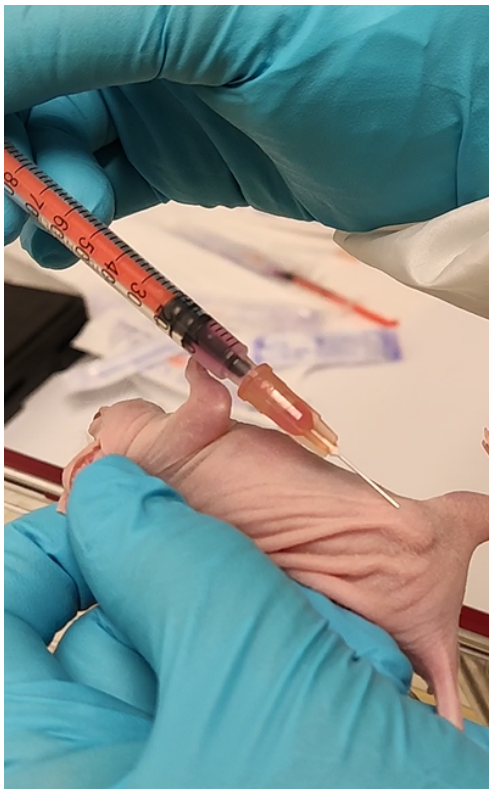

Figure 4.3: Technique used for s.c. injection of WiDr cells in the right thigh of the animal.

4.2.2. Therapeutical essay

The therapy began when the tumour became visible to the naked eye during daily surveillance, typically around 2 *mm* in size. This was fairly easy due to the hairless skin of nude mice. At this point, the superficial dimensions of the tumour (width and length[3]) were measured twice a week, along with the animal's weight. Measurements were taken using a digital calliper (*Wurth, stainless hardened, Germany*), ensuring consistency by involving the same well-trained operator to avoid inter-operator variability [143]. If the tumour grew in multiple nodules, the two dimensions of each visible one were registered. Each of the ten animals underwent a specific treatment according to its assignment to one of the following two groups:

- **Control group (A)**: mice inoculated with tumour and treated with chemotherapy, drinking water.

[3]They are the two greatest dimensions measured at right angles; width = transverse diameter; length = longitudinal diameter [142].

Table 4.1: Tested protocols within the *in vivo* studies. All protocols where tested in a minimum of two mice (one taking GTE and one drinking only water). All the selected combinations derive from clinical protocols, but some of the concentrations were modulated according to the *in vitro* results.

	PROTOCOL	PHARMACEUTICALS	REFERENCE
(1)	5-FU+CFA	5-FU $[400\,mg/m^2]$ CFA $[1,000\,mg/m^2]$	subsection 3.3.3.1
(2)	5-FU+CFA	5-FU $[600\,mg/m^2]$ CFA $[1000\,mg/m^2]$	subsection 3.3.3.1
(3)	FOLFIRI	5-FU $[400\,mg/m^2]$ IRI $[180\,mg/m^2]$ LV $[200\,mg/m^2]$	[147]
(4)	IRI	IRI $[180\,mg/m^2]$	subsection 3.3.3.2

- **Experimental group (B)**: mice inoculated with tumour, treated with chemotherapy, drinking water and a daily dose of GTE.

Four chemotherapeutic protocols were tested in four pairs of animals, matched between the two groups. The same protocol was administered to an animal drinking water and its counterpart drinking GTE. The two additional animals belonged to the control group and were used to further test two chemotherapy regimens. Further information about the tested chemotherapeutic protocols will be provided in the following paragraphs and in **Table 4.1**.
Animals undergoing chemotherapy were given a multivitamin and mineral supplement (vitamin D, calcium, and magnesium) twice a week (2.5 mg). This supplement was dissolved either into GTE (experimental group) or water (control group), and delivered via oral gavage (**Figure 4.4**). It aimed to improve the mice's quality of life and sustain their diet, especially in cases of reduced appetite and diarrhoea, which are common chemotherapy side effects. Literature suggests that proper intake of vitamin D, calcium, and magnesium can help increase patient survival, and vitamin D is necessary for better calcium absorption [144, 145, 146].
Animal monitoring was performed constantly through weight and tumour size records. Occision was programmed if the tumour or chemotherapy burden became unbearable for the animal (complying with the established humane endpoints) [22]. Situations leading to this decision included tumour diameter exceeding 1.4 cm, severe and rapid body weight loss (equal to or greater than 20% of pre-treatment weight), and persistent hypothermia.

4.2.2.1. Tested protocols

The chemotherapeutic protocols were determined based upon the best *in vitro* results achieved at the start of the *in vivo* experiments. Additionally, information from clinically used protocols helped to determine the dosage and treatment frequency. Details and references of each administered protocol are provided in **Table 4.1**. Two important remarks should be made regarding the designated protocols for *in vivo* testing. Firstly, the choice of tested concentrations for the CFA + 5-FU protocol. Although the optimal combination concentration *in vitro* was

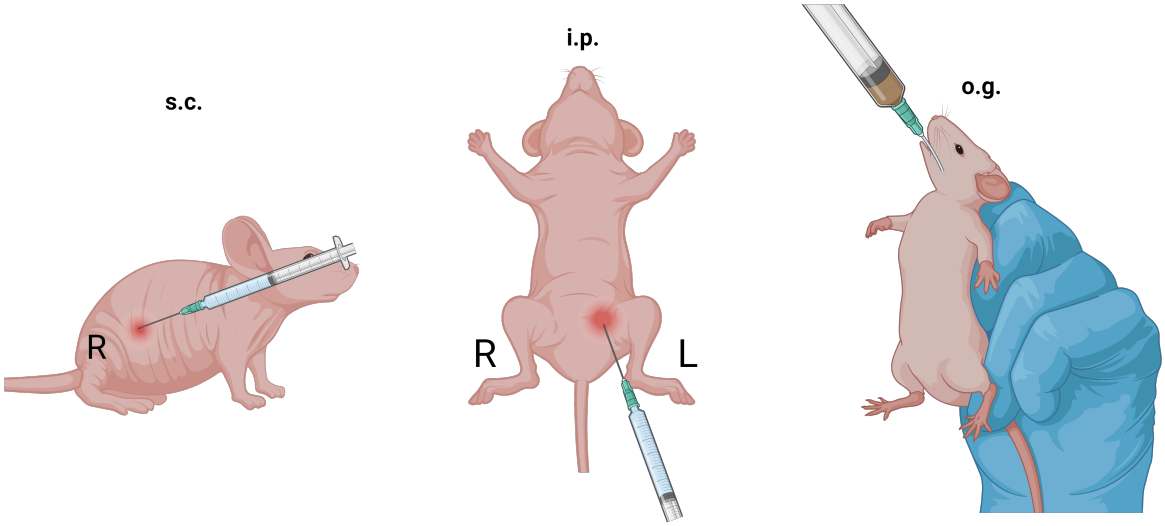

(a) s.c. subcutaneous **(b) i.p.** intraperitoneal **(c) o.g.** oral gavage

Figure 4.4: Ways of delivering cells or treatments to an animal: **(a)** the subcutaneous via (s.c.) was used to inject cancer cells; **(b)** the intraperitoneal administration (i.p) was used for chemotherapy delivery, radiotracer and anaesthesia injection; **(c)** the oral gavage was used to deliver GTE/water+vitamins (created with BioRender.com).

$[550\ mg/m^2]$, the two 5-FU concentrations tested on the animals were the lowest and highest ($[400\ mg/m^2]$ – $[600\ mg/m^2]$) (**subsection 3.3.3.1**, page 46). This decision was justified by the nature of CFA as a pro-drug. Hence, it was coupled with the minimum and maximum dosages of 5-FU to determine if its effect *in vivo* surpassed that of cultured cells. Furthermore, since 5-FU $[550\ mg/m^2]$ + CFA resulted in the most cytotoxic combination *in vitro*, it was preferable to start with the least cytotoxic concentrations to assess their side effect on the mouse. Failure of this test would have led to the rejection of this chemotherapy combination. Secondly, a notable remark concerns the *in vivo* FOLFIRI regimen, which, in addition to 5-FU and IRI, included LV (*MEDIFOLIN®, 15 mg capsules, Portugal*).

Leucovorin, also known as folinic acid, is a 5-formyl derivative of folic acid. Its role in CRC therapy is adjuvant, as it is usually co-administered with 5-FU. It stabilizes the binding of the drug to TS, thereby enhancing its effect on DNA [126]. The 5-FU/LV combination is beneficial as it requires a lower dose of 5-FU and prolongs patient survival. Moreover, the addition of IRI to this combination further improves the overall effects of chemotherapy, making it more tolerable and reducing the rate of adverse events [101].

4.2.2.2. Chemotherapy administration

The chemotherapy dosages mentioned were expressed using body surface area (BSA), a parameter commonly used in clinical practice [148]. The measurement unit $[mg/m^2]$ was adapted to the size of mice to represent an equivalent of human treatment. Specifically, the dosage of each chemotherapeutic agent was calculated proportionally, considering that each mouse has an average BSA of 60 cm^2 [149]. These dosages were administered as a bolus intraperitoneal (i.p.) injection (refer to **Figure 4.4b**). A 1 mL syringe coupled to a 25G needle, similar to

the ones used for tumour inoculation, was utilized. Despite the volume being on the order of 10^2 μL, the administration was performed as slowly as possible to mimic human injections and minimize animal suffering. In cases where the calculated amount of drug was too small, it was diluted in PBS to slow down the injection. When delivering combination regimens, different pharmaceuticals were administered sequentially using distinct syringes. Although the intravenous route offers the best drug bioavailability, it is challenging for repeated injections due to the very reduced calibre of tail vein in mice. On the other hand, the i.p. route was preferred as it is more feasible and provides outcomes comparable to the intravenous route in terms of drug bioavailability and absorption rate, enabling numerous injections [150]. Hence, the i.p. route was selected for chemodrugs' administration.

4.2.2.3. Green tea

Upon starting of chemotherapy, animals in the experimental group (Group B) were supplemented with GTE. For the *in vivo* studies, the GTE solution was prepared using the same green tea extract powder (GTE po) used *in vitro* (see **subsection 3.2.3**, page 33 - *MyProtein, Green Tea Extract powder, 500 g, 1705807841, UK*). The procedure began by measuring GTE po using a precision electronic balance (*Radlag, AS 220/c/2, Germany*), and transferring it into a 50 *mL Falcon* tube. Tap water was used to dissolve GTE po using a vortex mixer (*Unimag ZX3 Vortex Mixer, D-82152, Germany*). Once homogenized, the resulting solution (0.046 g/mL) was divided into sterile 2 *mL Eppendorf* tubes (*Biologix, 80-0020, China*). Due to the photosensitivity of GT, the *Eppendorf* tubes were wrapped with aluminium foil and stored in the fridge until administration (at -20° C for longer waiting periods or 4° C for shorter periods). GTE wase administered daily. Several minutes in advance, the *Eppendorf* tubes containing GTE were removed from the fridge to warm up until room temperature. In a preceding study, it was discovered that mice do not like the taste of GTE at all, hence they do not drink it spontaneously as a substituent of water [151]. Oral gavage (o.g.) was the strategy to overcome this situation. For this procedure, a 1 *mL* syringe was coupled with a flexible Abbocath (*BD InsyteTM AutoguardTM Blood Control, 381034, 20G × 1,16 pol., 1,1 mm × 30 mm*), cut to a length of approximately 2 *cm*. The operator gently grasped the mouse by the skin of the back and of the neck to distend it and immobilize the animal. This technique enables a better positioning of the esophagus to introduce the Abbocath, ensuring its placement behind the tongue to prevent suffocation and tube teeth bite. The GT solution was then delivered directly into the esophagus, as depicted in **Figure4.4c**. The daily administered dose was 0.55 mg/g of animal body weight. Therefore, the volume of liquid to be administered via syringe was approximately 0.3 *mL*. This calculation considered the mean body weight of mice (25 *mg*) and the concentration of the GTE solution (0.046 mg/mL).

4.2.3. Imaging study

The calliper measurement, while standard for tumour volume assessment, lacks precision due to its manual nature. Tumors can be replaced by fibroadipose tissue, especially when undergoing chemotherapy, or even become necrotic. Thus, the tumour may be larger in size, but tumoural

tissue will no longer be functional due to cell replacement or death. Therefore, in this study, a functional imaging technique was required to gain a comprehensive understanding of the internal dynamics occurring within the animal subjects. Given the research group's expertise in this field, Positron Emission Tomography (PET) was chosen as the imaging technique.

PET, a powerful tool in nuclear medicine, uses a radioactive tracer (radiopharmaceutical) to evaluate bodily functions. The radioactive tracer is injected into the body and emits positrons through radioactive decay. When a positron encounters an electron, annihilation occurs, releasing energy in the form of two antiparallel gamma photons (511 keV). PET scanners detect these emitted photons and use the information to generate a 3-dimensional (3D) image of the body's internal activity distribution [152] (**Figure 4.5**). PET scanners have special detectors usually arranged as pairs in a ring, to capture the nearly simultaneous incidence of collinear 511 keV photons (coincidence event). The line connecting any two detectors, known as the LoR, is used to localize the positron-emitting nucleus. The number of coincidence events between a pair of detectors indicates the amount of radioactivity along the LoR. Mathematical algorithms are then applied to reconstruct biomedical images, as discussed in a following paragraph [153, 154].

PET is a well-established imaging modality in oncology due to its non-invasiveness and its ability to assess metabolic activity through an enhanced radiotracer uptake by cancer tissue [155]. Commonly used radiotracers include [^{18}F]-FDG, a glucose analogue, which accumulates in areas of increased glycometabolism, enabling quantification of tumour tissue activity. It is a diagnosis at the molecular level [156]. Despite its advantages, PET is limited by low resolution, especially for early tumour detection. This limitation (more deeply discussed later on) is particularly challenging in small animal imaging, where high resolution is crucial [157]. However, recent advancements have led to the adaptation of PET imaging techniques and scanners for small animals, such as the easyPET.3D system used in this study [158]. The easyPET.3D system enabled the longitudinal monitoring of mice, with each animal undergoing weekly imaging when feasible. This imaging study aimed to assess the system's ability to detect small tumours and track tumour burden progression. Additionally, it aimed to quantitatively evaluate the effect of the experimental therapy. Specifically, the expectation was to observe a longitudinal reduction in [^{18}F]-FDG uptake by the tumour tissue in the experimental group compared to the control group. This reduction would serve as an indicator of tumour response to the tested treatments, particularly to GTE.

The imaging protocol steps are shown in **Figure 4.6**. The As Low As Reasonably Achievable (ALARA) principle drove the study design. This principle states that every time that a ionizing radiation has to be applied to humans, animals or materials, the exposure should be as low as reasonably achievable, still maintaining suitable image quality for diagnosis/study [159]. This principle translates into practical guidelines, including selecting the appropriate dose for the patient, minimizing exposure time to radioactive sources, maximizing the distance from the source[4], and using appropriate shielding to minimize radiation exposure to both animals and operators [161, 162]. To fulfil them, all procedures took place in laboratories certified by the

[4]The amount of radiation exposure is inversely proportional to the square of the distance from the radiation source [160].

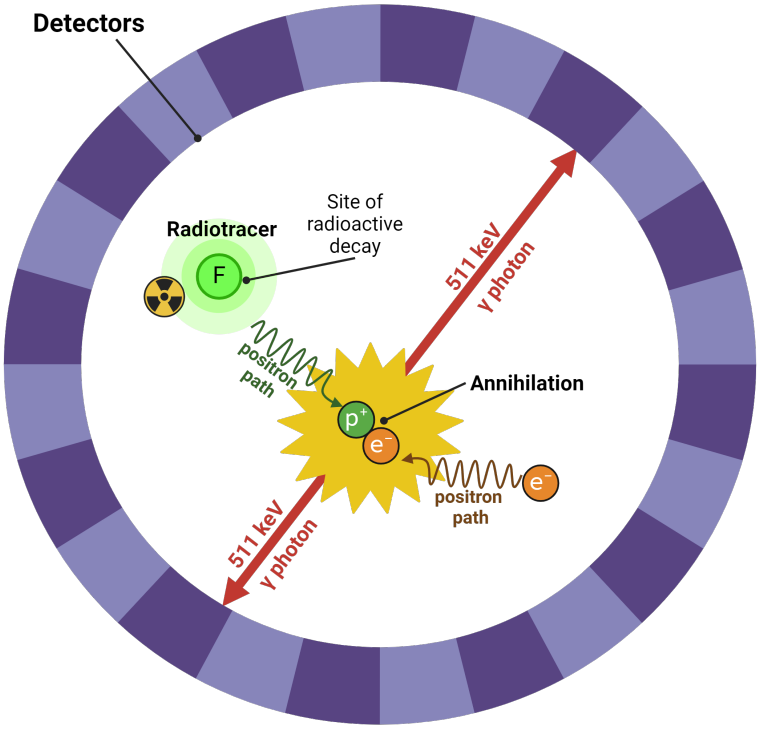

Figure 4.5: Basic principle of a conventional PET system: a PET detector ring detects a couple of collinear gamma photons with 511 keV energy (red arrows) which derive from the annihilation of an electron coming from the body (e^-) with a positron (p^+) emitted by the radiotracer, [^{18}F]-FDG (created with BioRender.com).

Nuclear and Technologic Institute and a rigorous control over the radiation exposure was applied. The operator manipulating the radiation always wore a dosimeter, and lead protections were used for shielding. Additionally, all radioactive waste underwent proper disposal procedures.

4.2.3.1. Radiotracer

The radiotracer injection into the mice enabled PET imaging acquisition. As already reported, ^{18}F-fluorodeoxyglucose ([^{18}F]-FDG) was the radiopharmaceutical used. Its formula is depicted in **Figure 4.7**: it is a glucose molecule labelled with a radioactive fluorine (^{18}F). The radiolabelled glucose molecule is uptaken by the cells through glucose transporters; then hexokinases phosphorylate it, turning it in [^{18}F]-FDG-6-phosphate, which becomes stored within the cell [163]. In contrast to glucose, which undergoes further metabolic processing within the cell, phosphorylated [^{18}F]-FDG experiences a metabolic halt and becomes trapped within the cell [163]. [^{18}F]-FDG is extensively used in oncology for cancer diagnosis and monitoring, as it has a preference for cancer cells over normal ones due to their increased anaerobic glycolysis[5] [165, 166]. ^{18}F is a radionuclide that undergoes β^+ decay[6] with a half-life[7] of 109.8 minutes [167]. These features make it a highly attractive radionuclide for radiochemical labelling and molecular

[5]Anaerobic glycolysis is an energy production process occurring in cells that cannot produce adequate energy via oxidative phosphorylation [164].

[6]In a β^+ decay the radioactive nucleus emits a positron.

[7]Radioactive half-life ($\tau_{1/2}$): time required for a quantity of a radioisotope to decay by half.

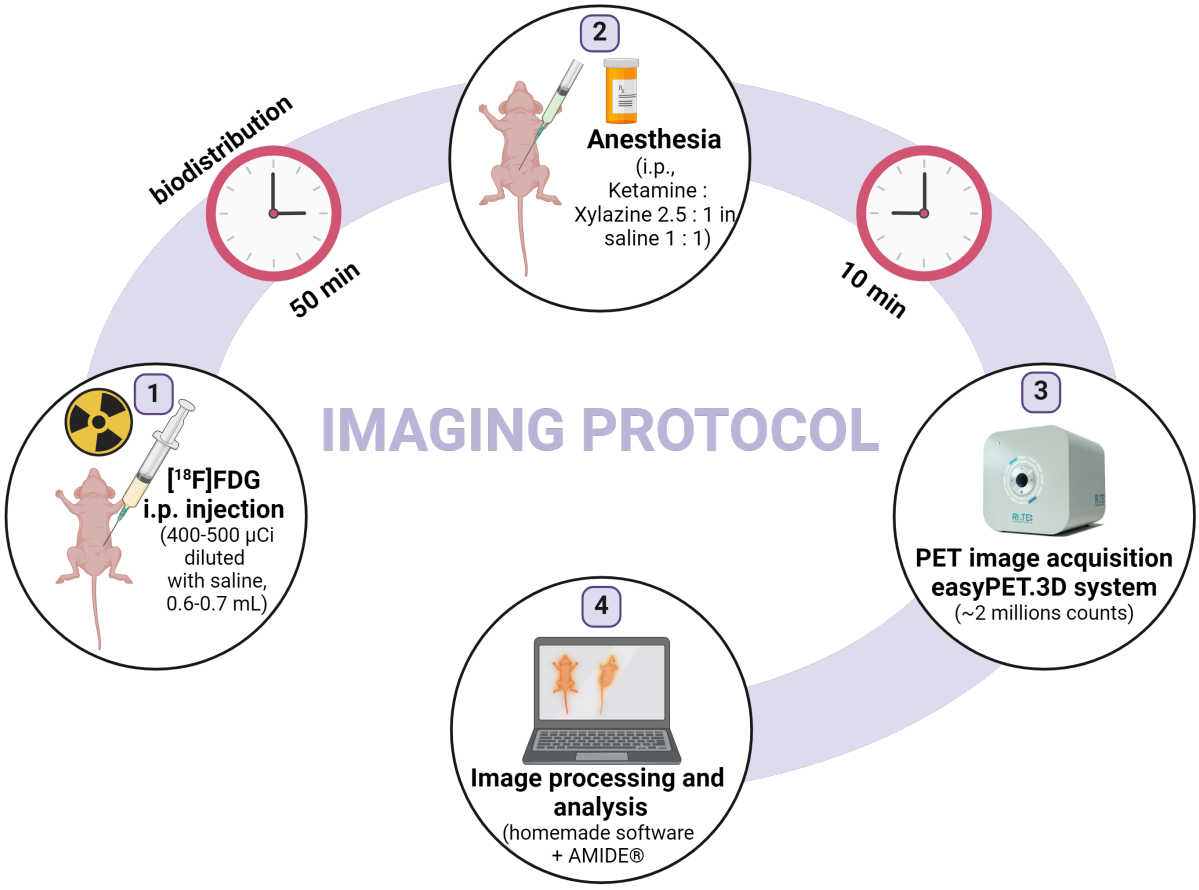

Figure 4.6: Steps followed for the imaging study (created with BioRender.com).

imaging applications such as PET.

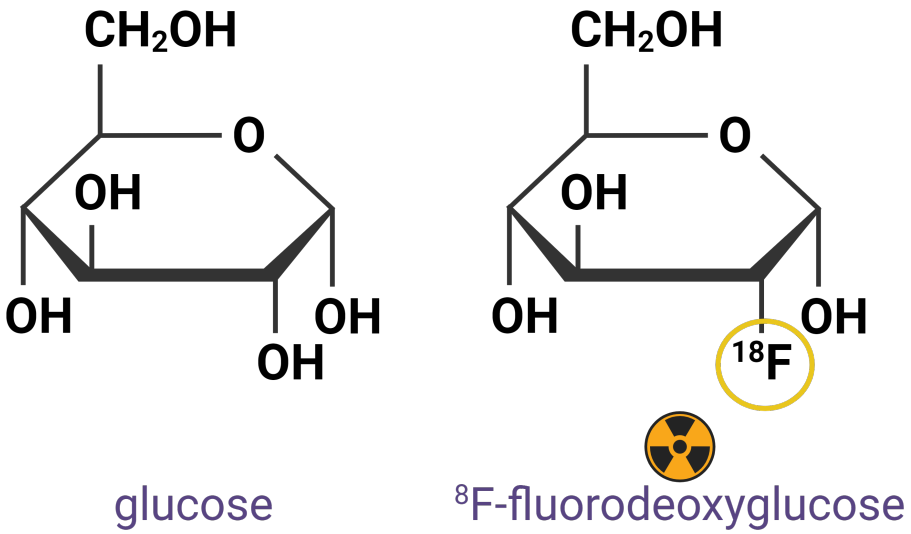

Figure 4.7: Chemical structure of glucose and its radioactive counterpart [^{18}F]-FDG. The only difference between the two is the presence of a ^{18}F replacing an OH (hydroxyl) group (created with BioRender.com).

The [^{18}F]-FDG used in this study was provided by the Department of Nuclear Medicine at Coimbra University Hospital, following partnership with the Biophysics Institute (FMUC-iCBR-cibb) where the research was conducted. It is important to note that the feasibility of performing weekly scans on each animal depended on their health status and the availability of [^{18}F]-FDG, which was obtained from surplus supplies of the hospital's daily diagnostic activities. The [^{18}F]-FDG was collected by the hospital and transported until the laboratory using a lead shielded carrying case (*Protector Shield Biodex, USA*, **Figure 4.8a**). The radiopharmaceutical dose was prepared in a hot cell[8] (*Medisystem, Medi 9000 4R LME, 11915*). [^{18}F]-FDG was drawn into a 1 *mL* syringe (*Pic Solution Syringe, U-100 insulin, 1608022, Italy*) coupled to a 25G needle (*Pic Solution, 0,5×16mm, 25 G5/8", 1811371, Italy*). The administered dose was adjusted to 14.8 - 18.5 MBq. The radioactivity was measured using a dose calibrator[9] (*CRC®-15 W, Capintec, USA*). The [^{18}F]-FDG was then diluted with physiological saline (*Cloreto de Sódio 0,9%, Labesfal, Laboratórios Almiro S.A, Portugal*) until reaching a final volume between 0.5 and 0.6 *mL*. This volume of liquid has been ascertain in previous studies, considering factors such as the animal's mean body weight, the characteristics of the easyPET.3D system, and the residual radioactivity remaining in the syringe after injection [169]. The prepared solution was administered to the mouse via i.p. injection. Radioactivity records were meticulously maintained throughout the study, noting the measured

[8]Hot cell: shielded containment chamber used by operators to prepare radioactive substances in a protected environment.

[9]Dose calibrator: a device that measures the total amount of a radionuclide (in curies (Ci) or becquerels (Bq)). It is a hollow, lead shielded cylinder, ionization chamber, to hold the radioactive source during measurement. It has also a display unit showing the activity level [168].

(a) Lead carrying box to transport the syringe containing the radiotracer.

(b) Opened lead box.

(c) Hot cell.

(d) Dose calibrator.

Figure 4.8: Laboratory equipment used for the manipulation of radioactive substances (Biophysics Institute-FMUC-iCBR-cibb).

radioactivity in the syringe before and after injection, as well as the residual activity in the syringe after injection together with the hour of each measurement. Following injection, a biodistribution time of 60 minutes was allowed before image acquisition [169]. During this uptake period, the animal was housed alone in a dedicated clean cage without access to food but with water *ad libitum*. Additionally, the animal had been fasting for the preceding 5-6 hours to reduce blood glucose levels, thereby minimizing competition between [^{18}F]-FDG and endogenous glucose for transporters and enhancing [^{18}F]-FDG uptake at the cancer site [169]. The animal was kept warm during this period using an electric heater set to maintain a temperature between 36.5 - 38° C. This was done to minimize tracer accumulation in skeletal muscles and brown fat while increasing metabolic rate [165, 170].

4.2.3.2. Anaesthetic solution

Administering anaesthesia is an essential step to ensure animals remain immobile and minimize non-physiological motion during PET acquisition. Additionally, it has been observed that anaesthesia has a secondary positive effect of markedly reducing background activity ([^{18}F]-FDG

uptake by brown fat tissue and skeletal muscles), thereby enabling a clearer identification of the tumour mass in the image [169]. Therefore, 50 minutes after [^{18}F]-FDG injection (and 10 minutes before the PET scan), an anaesthetic solution was prepared and administered intraperitoneally. The anaesthetic solution consisted of 2.5 parts of ketamine (*Ketamine Hikma 50 mg/ml, Hikma pharmaceuticals™, Portugal*) mixed with 1 part of xylazine (*Rompum®, 20 mg/ml, Bayer, Portugal*). This solution was diluted with physiological saline in a 1:1 proportion until reaching a volume between 0.15 and 0.20 *mL*.

Xylazine (2-(2,6-xylidino)-5,6-dihydro-4H-1,3-thiazine hydrochloride) is an alpha-2 adrenergic agonist[10] that induces sedation, muscle relaxation, and possesses analgesic properties. It also has a hyperglycaemic effect by stimulating alpha-2 adrenergic pancreatic receptors to inhibit insulin secretion [171]. Xylazine is often combined with ketamine to achieve stable sedation and reduce muscular stiffness [172].

Ketamine (2-(2-chlorophenyl)-2-(methylamino)cyclohexan-1-one), on the other hand, is a derivative of phencyclidine. It acts as a dissociative anaesthetic through central nervous system activation and sympathetic stimulation [173]. Ketamine has a broad spectrum of pharmacological effects, including sedation, catalepsy, and sympathetic nervous system stimulation. It primarily acts as a non-competitive antagonist of the N-methyl D-aspartic acid (NMDA) receptor[11] [175]. During this phase, the animal's body temperature was maintained using the electrical heater (set to 36.5 - 38° C, as previously referred). Preserving body temperature is crucial for anaesthetic management, as hypothermia can be lethal for small rodents. Core body temperature typically decreases soon after injection and continues to decline during the period of general anaesthesia [173]. Once the animal was asleep and immobilized, it underwent the easyPET.3D scan.

4.2.3.3. easyPET.3D

PET imaging technology has made a fast progress over the past decades. This breakthrough in technology enabled the transition from human-sized PET systems to a setup suitable for small animal research. This development has significantly enhanced the applicability of PET in preclinical studies [154]. A direct comparison between their sizes reveals that while the lengths of most human bodies fall within the range of 150-180 cm, laboratory mice, which are commonly used in preclinical studies, have nose-to-anus lengths smaller than 10 cm. Clinical PET scanners typically have spatial resolutions[12] of nearly 3.0 *mm* [176]. For preclinical PET scans to achieve the same detail as those used in human studies, the scanners need a resolution exceeding 0.2 *mm*. This higher resolution allows researchers to see finer structures in mice, leading to more accurate data [177]. Hence, high sensitivity[13] and resolution are key required characteristics, but also major challenges for the development of these devices [179]. A common strategy to improve

[10] α2-adrenergic agonist: mimics the effects of the hormone norepinephrine, thus opposing the effects of the sympathetic nervous system.

[11] NMDA: a receptor of glutamate, the primary excitatory neurotransmitter in the human brain [174].

[12] Spatial resolution: a measure of the finest anatomical structure that the scanner can resolve.

[13] Sensitivity: the number of 511 *keV* photon pairs per unit time detected by the scanner for each activity unit present in a source [178].

the sensitivity is to use ring detectors with small diameters and thick scintillator crystals[14]. Unfortunately, thicker crystals cause a higher parallax error, which is a LoR mispositioning error occurring for off-center annihilations (**Figure 4.9a**) [181]. Other sources of error (independent from crystal thickness) include scattered coincidences due to the Compton effect[15] (**Figure 4.9b**) and random coincidences (**Figure 4.9c**).
The limitations of small animal PET imaging, stemming from factors such as reduced sizes and inherent physiological effects, result in compromised image quality and resolution, which imply advanced algorithms for reconstruction. Consequently, the cost of such systems ranges significantly between $400,000 and $1,200,000, often surpassing their benefits [183].

Responding to these challenges, the easyPET.3D system (*Patent, Aveiro University: WO2016147130*), developed at Aveiro University, emerges as a groundbreaking solution. Unlike traditional PET scanners with full detector rings, this system features only a pair of collinear detectors with two degrees of freedom. Despite their limited number, these detectors achieve coverage equivalent to conventional PET scanners by using innovative rotating movements pivoting on alternating rotation axes. The unique design and geometry of the easyPET system are elucidated in **Figure 4.10**.
Each detector block consists of an array of 64 detector cells. Each detector cell is made of lutetium-yttrium oxyorthosilicate (LYSO) scintillator crystals (size $2\times2\times30\ mm$) coupled with silicon photomultipliers (SiPMs) with an active area of $1.3 \times 1.3\ mm^2$. These components are used to detect optical photons emitted by the scintillators, thereby generating a measurable electrical signal [185]. Detectors are arranged on a printed circuit board, on which the time coincidence logic operates. This circuit is also attached to a two-step motor, performing the scan and the revolution, covering up a different FoV, depending on the θ range setting. These features constitute a maximum axial FoV[16] of 48 *mm*. This design forms the basis for the easyPET's intrinsic robustness against imaging errors. For instance, the fact that the two detectors are always face-to-face increases the probability that gamma-photons hit them perpendicularly, hence strongly reducing parallax errors, and scatter errors as well. Therefore, easyPET.3D enables the achievement of high spatial resolution ($1.0 \pm 0.1\ mm$), uniform across the entire FoV, thanks to the two degrees of freedom in the movement of the detectors. The detector arrangement itself could also lead to limited geometric acceptance, thus restricting the number of detected events and impairing the sensitivity of the system. However, the easyPET.3D system circumvents this limitation by lowering the energy threshold (that photons must overcome to be detectable), until the rate of random coincidences becomes negligible. This allows for the acceptance of more events, thereby increasing the overall sensitivity by up to 0.23% [184]. Thanks to the limited

[14] Scintillator crystals: they absorb gamma-rays coming from the photons' annihilation and convert them into visible photons; the thicker they are, the higher the number of gamma-photons they can capture and convert [180].

[15] Compton effect: gamma-photons collide with single electrons that are free in the matter. As they collide, photons transfer some of their energy and momentum to the electrons, thus losing energy and changing their trajectory [182].

[16] The axial FoV is the maximum length parallel to the long axis of a positron emission tomograph, along which the instrument generates transaxial tomographic images [186].

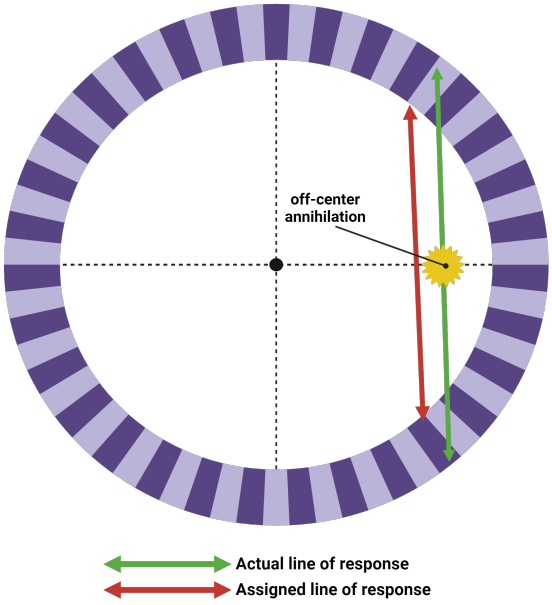

(a) Parallax error: when an annihilation event occurs away from the centre of the scanner, gamma-photons generated by the event do not enter the scintillators perpendicularly through their faces. Instead, they enter at an angle, which causes a misalignment between the true origin of the annihilation event and the line of response determined by the coincidence detection system.

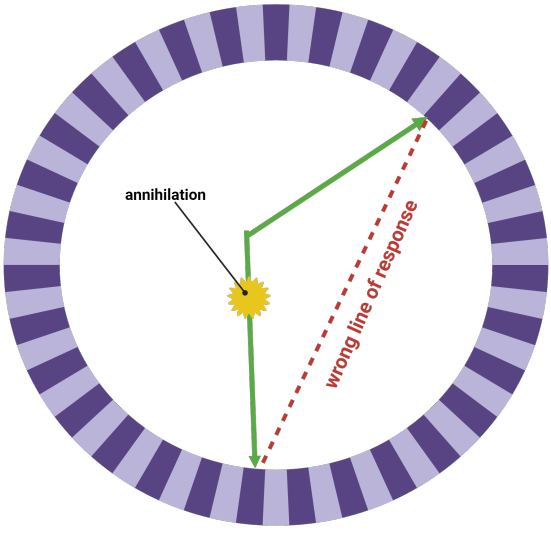

(b) Scatter coincidence: one of the two emitted gamma-photons may undergo scattering, causing its deviation from the original trajectory. Despite this scattering, both photons are still detected by the scanner: because of the deflection in trajectory, the detected positions may lead to the calculation of an incorrect line of response.

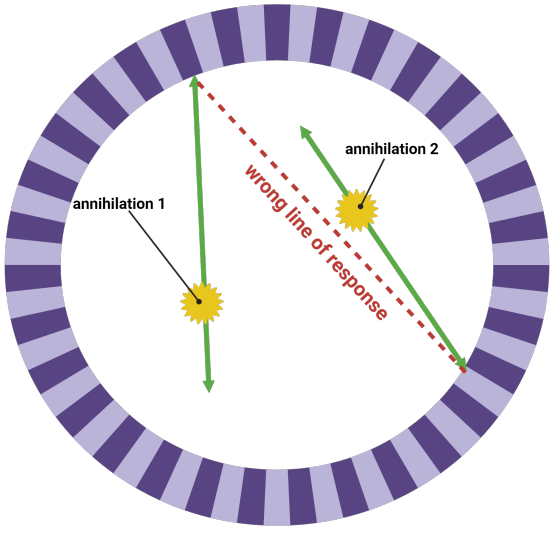

(c) Random coincidence: two simultaneous annihilations take place, producing two pairs of gamma photons; if, by chance, two of the photons coming from different events are detected within a short time window, they define a randomly oriented line of response.

Figure 4.9: Sources of error in PET images (created with BioRender.com).

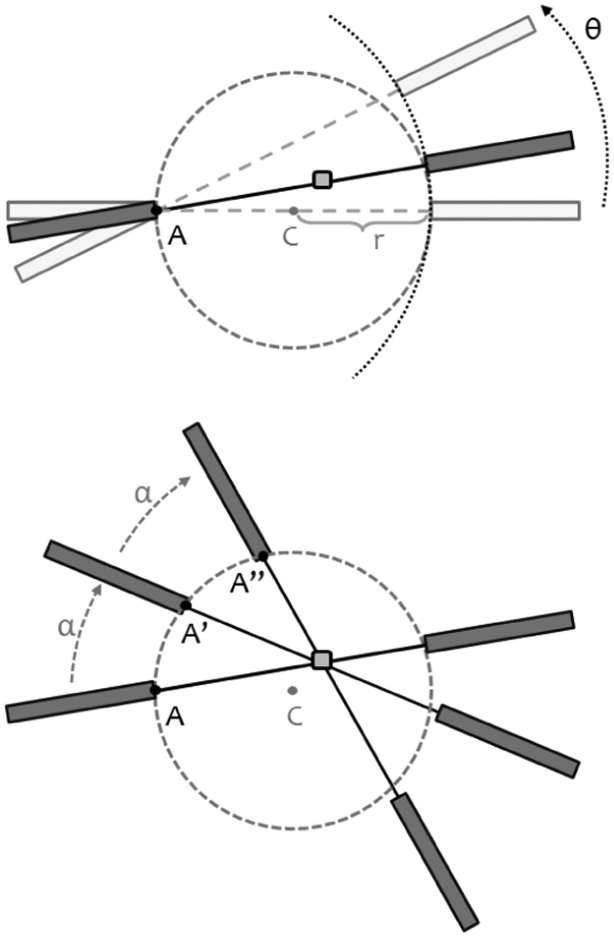

Figure 4.10: Geometry of the easyPET.3D system: **C** represents the system centre, and **2r** denotes the distance between the detectors, which are mounted on the same structure. If the detectors were to rotate solely around **C**, only annihilation events occurring at **C** would be detected. Hence, the pair starts rotating around **A**, the front face of one detector, moving along an arc of circumference and scanning an angle θ. The resulting scan axis then revolves in a circumference centred on **C**, moving through a sequence of positions (**A'**, **A"** and so on). This scan is replicated for every position of the θ scan axis until achieving a complete revolution of the system. During each scan, any source within the entire FoV will generate a coincidence detection at an azimuthal angle relative to the position of the θ scan axis. Consequently, by combining the information from all the LoRs obtained with the different orientations of the scan axis, it is possible to reconstruct the source position (retrieved from [184]).

number of components, the easyPET.3D device is a benchtop system, small, and affordable. The value of this new concept is remarkable as it reduces costs while maintaining high performance. It also has a broad spectrum of applications: by using detectors with different geometries and adjusting several parameters, it is possible to adapt it to specific regions of interest and desired levels of speed and sensitivity [184, 187, 188].

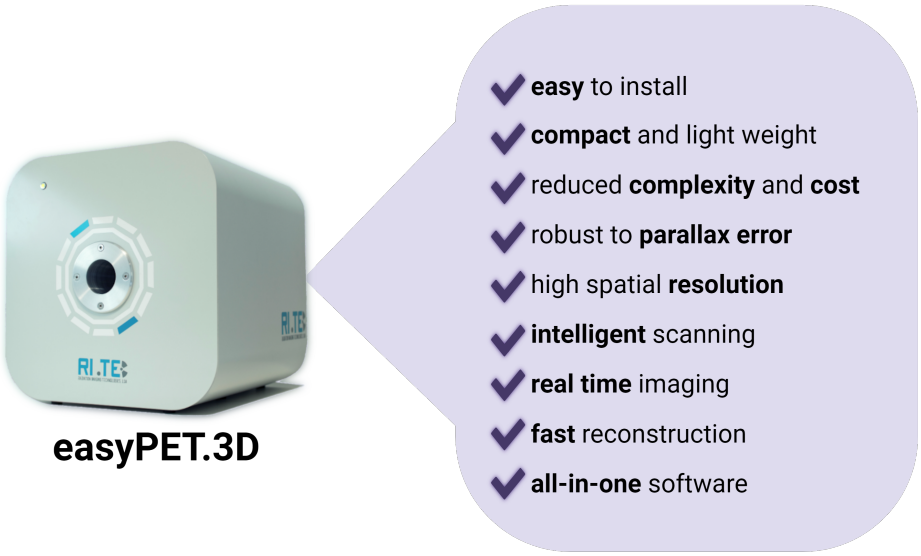

Figure 4.11: Main advantages of the easyPET.3D system (created with BioRender.com).

4.2.3.4. Image acquisition and reconstruction

While the animal is being anaesthetized and fell asleep, preparations for PET image acquisition start. The homemade software of the easyPET.3D system required several fields to be completed pertaining to animal identification (ID, date of birth, normal/not normal, and injected cell lines), the radiopharmaceutical (dose and administered volume, residual activity in the syringe, and the time of each measurement), the anaesthetic mixture (type and administered volume), and the animal's position on the device bed (head first/feet first). To ensure optimal animal positioning during the examination, the easyPET.3D system includes a specially designed 3D-printed plastic bed with a cylindrical shape (40 *mm* diameter and 260 *mm* length - **Figure 4.12a**). The material for the bed structure was chosen to minimize radiation attenuation. Thus, the anaesthetized animal was carefully placed on the bed in a ventral decubitus position, ensuring that the tumour was within the FoV (**Figure 4.12b**). Once all parameters were set, the image acquisition was started.

Each image acquisition session required a minimum of 2 billion counts, resulting in a duration of approximately 20 to 30 minutes. Throughout this period, the animal's body temperature was maintained using a heat therapy pump (*Adroit Medical Systems, HTP-1500, USA*, **Figure 4.13**), with silicone tubes positioned beneath the bed. This heating was crucial to prevent hypothermia, which could adversely affect image quality by increasing radiotracer uptake by the interscapular brown fat, and interfering with the visualization of neighbouring structures, as previously discussed (**subsection 4.2.3.1**, page 64) [173].

(a) Bed of easyPET.3D scanner.

(b) Transverse view of the animal position inside the tomograph.

Figure 4.12: Details of the easyPET.3D system

Figure 4.13: Heat therapy pump used to warm up the animal during the scan.

The easyPET.3D software provides an initial coarse visualization of the acquired image. Subsequently, the raw data collected during the scan undergoes a reconstruction process, a complex mathematical procedure wherein for each slice, coincidence events detected along different LoRs are projected and assembled. Then, all slices are put together to generate the PET image, representing the distribution of the radiotracer across the FoV[17] [190]. Reconstruction was performed using the easyPET.3D system. The iterative algorithm used for reconstruction was list-mode maximum-likelihood expectation-maximization (LM-MLEM) working on graphics processing unit (GPU) (25 iterations, energy window 350-650 keV[18]) to enable accurate real-time estimation of the annihilation event positions. In essence, this algorithm combines two techniques. The list-mode (LM) implies that detected gamma-photons, each characterized by its parameters (time + position), are organized into a list. This mode offers the advantage of leading to a more uniform reconstruction across the FoV [192]. Maximum-likelihood expectation-maximization (MLEM), on the other hand, is an iterative reconstruction algorithm that discretizes the image into pixels and considers each pixel value as unknown. This optimization method seeks the best estimate of the unknown vector f, representing image pixel values. The maximum-likelihood criterion is the statistical principle used to determine the most likely image among the many possible solutions. Expectation maximization, on the other hand, is the numerical method used to find the solution prescribed by the maximum-likelihood criterion [193, 194]. Specifically, maximum-likelihood is used twice: once for position estimation and once for reconstruction. Its utilization results in an asymptotically optimal estimate of the interaction location, thereby reducing blur in the reconstructed data [195].

As a result, the reconstructed 3D-PET image consists of many slices. Hence, the sum of the multiple 2D slices, produces a reconstructed 3D-PET image, which can be viewed from three different perspectives: axial, sagittal, and coronal. Each slice is a 2D image composed of a matrix of pixels. Each pixel represents a volume element (voxel), which has the same 2D sizes as the pixel, but also a third size (over the z-axis), equivalent to the slice thickness of the scan. The colour intensity of each pixel represents the number of detected gamma-photons in the corresponding voxel: the hotter the colour (according to the colour scale), the higher the radioactivity [196]. The voxel size used during reconstruction was $1 \times 1 \times 1.07\ mm^3$, with each slice being, therefore, 1.07 mm thick.

4.2.3.5. Image processing

In order to analyse and extract quantitative data from reconstructed images, it was necessary to process them. The PET datasets were imported using the non-proprietary AMIDE® software

[17] A projection is obtained by integrating the radiotracer distribution in the object along all parallel LoRs (at a specific angle ϕ). The collection of all projections for all angles is arranged into a sinogram, a 2D function where each row corresponds to one projection. Mathematical details of this process are well explained in [189].

[18] If there were no scattered photons, the energy of incident photons would form a sharp peak at 511 keV. However, the presence of scatter broadens this peak. The energy window in a PET tomograph is the range of energy within which incident photons must fall to be detected as true events. Typically, PET scanners use an energy window with minimum and maximum thresholds of 350 and 650 keV, respectively, to avoid discarding too many photons and maintain adequate system sensitivity. However, this wider energy enhances the image background noise [191].

(*AMIDE's a Medical Image Data Examiner, amide.exe 1.0.6*). The processing allowed to quantify PET data and obtain biological functional information about the tumour metabolic activity: the tumour area was segmented by implementing a ROI, which was used to calculate statistics, and, particularly, the standard uptake value (SUV). SUV is a PET imaging biomarker[19], frequently used for characterizing [^{18}F]-FDG uptake of a specific ROI [198]. The basic calculation of this index follows the equation:

$$SUV = \frac{C_{ROI}\,(MBq/mL)}{ID\,(MBq)/BW\,(g)} \tag{4.1}$$

Where C_{ROI} is the ROI activity (MBq/mL[20]) normalized for the injected dose (ID) and the animal body weight (BW) [199]. However, this index shows variability due to the time delay between [^{18}F]-FDG injection and the PET acquisition.

A correction for ^{18}F physical decay can be applied by multiplying the injected dose by λ, the ^{18}F physical decay constant, which is equal to $1.053 \times 10^{-4}\ s^{-1}$ [21] [201, 202]. Thus, the **Equation 4.1** becomes:

$$SUV = \frac{C_{ROI}\,(MBq/m)}{ID\,(MBq)/BW\,(g)} \times \frac{1}{\lambda} \tag{4.2}$$

There are several ways to express SUV, depending on the normalization factors used. More often, the general SUV can be expressed as mean standard uptake value (SUV_{mean}) or maximum standard uptake value (SUV_{max}). The former is the mean value of all voxels included in the selected ROI; the latter represents the pixel with the highest [^{18}F]-FDG uptake activity [203, 204]. To calculate these indexes, average and maximum values of tracer concentrations in the ROI are calculated and replace C_{ROI} in **Equation 4.2** [199]. For instance, the mean radioactivity concentration in the ROI ($C_{meanROI}$) is usually supplied by imaging softwares, which calculate via the formula [200]:

$$C_{meanROI} = \frac{\frac{Mean\ activity_{ROI} \times Number\ of\ voxels}{ROI\ volume(mm^3) \times 0.001mL}}{Acquisition\ time\ (s)}; \tag{4.3}$$

It is important to remember that SUV is a semiquantitative parameter. Two PET scans performed on two consecutive days in the same patient may yield slightly different SUV values, even if the lesion is the same. This occurs because the [^{18}F]-FDG uptake in a lesion depends on multiple technical and biological factors [205].

[19] An imaging biomarker is a characteristic extracted from an image that can be objectively measured and serves as an indicator of a normal biological process, a disease, or a response to a therapeutic intervention [197].

[20] Bq = Bequerel, SI unit of radioactivity. 1 Bq = one nuclear disintegration per second. The ROI activity in PET is expressed as a the measured concentration of radioactive events per tissue volume (Bq/mL).

[21] The physical decay constant (λ) is a crucial parameter in radioactive decay. It is expressed in the radioactive decay law: $N_t = N_0 \times e^{-\lambda t}$, where N_t is the number of radioactive nuclei remaining after time t, and N_0 is the initial number of nuclei. The physical decay constant λ is related to the half-life ($\log_2/\tau_{1/2}$) of the radioactive isotope by the equation $\lambda = \log 2/\tau_{1/2}$. Given that the half-life of ^{18}F is 109.8 minutes, λ can be calculated as the natural logarithm of 2 divided by the half-life ($\tau_{1/2}$) [200].

4.2.3.6. Quality control and quality assurance of the PET tomograph

The crucial features of experimental design in preclinical research include selecting an appropriate animal model, choosing the proper radiotracer, therapeutics, and anaesthesia. Additionally, it is essential to evaluate the performance of the imaging system, both in terms of acquisition and reconstruction processes, to ensure robustness and reproducibility [206, 207]. Fulfilling the instrumentation quality control[22] and assurance[23] requirements is fundamental to prevent the generation of inadequate results due to instrumentation bias or miscalibration [210]. In 2008, the National Electrical Manufacturers Association (NEMA) published a document entitled 'Performance Measurements of Small Animal Positron Emission Tomography' (NEMA-NU 2008), which aimed to establish standardized guidelines for evaluating the performance of PET scanners specifically developed for animal imaging [211].
The NU 4-2008 document discloses all the aspects of the PET scanner performance: scanner sensitivity, scatter corrections, spatial resolution, and image quality. While the procedures outlined in the NEMA document are detailed and extensive, NEMA testing is typically not performed as part of routine operations, but rather during scanner installation. During the present work, quality assurance was performed daily through visual checks of the equipment and careful preparation prior to radiotracer administration. System calibration was done once every two weeks, due to the frequency of image acquisitions. Furthermore, to assess the PET tomograph performance, specific acquisitions were conducted using phantoms. Phantoms are commonly used tools in molecular imaging to evaluate scanner performance [212].

Uniform phantom

The uniform phantom is a crucial tool for calibrating the PET system. Calibration involves assessing the relationship between the detected event rate in each pixel and the true activity concentration of the corresponding volume element within the phantom [213]. In essence, this process converts the PET true count rate (counts per second) detected in each pixel into a measure of radioactivity (*Bq*). Calibration is indispensable for establishing the relationship between the device's measurement and the actual amount of radioactivity, accounting for the sensitivity and performance of the PET scanner. This allows for quantification [214]. Calibration is achieved by scanning a radioactive object with a known quantity of radioactivity and shape, such as the uniform phantom. In the present study, the uniform phantom used was a polymethylmethacrylate (PMMA) fillable cylinder with an internal diameter of 38 *mm* and a length of 72 *mm*, providing a total fillable volume of 73 *mL*, thus able to cover the whole FoV (**Figure 4.14**). Designed with two lids, two screwas and two rubber gaskets to prevent liquid leakage, it was filled with tap water mixed gently and homogeneously with the radiotracer, [^{18}F]-FDG. This radioactive source was chosen to cross-validate the dose and PET systems with data from imaging experiments. To

[22] Quality control: regular monitoring, evaluation and maintenance of the performance of the imaging equipment to ensure optimal performance and stability, together with the radiation protection [208].

[23] Quality assurance is the planned and systematic process of assessing whether a product or service fulfils specified requirements [209].

Figure 4.14: Uniform phantom used for calibration.

ensure the calibration measurement closely mirrored animal imaging conditions, the phantom was filled with the dose typically used in animal imaging, ranging from 14.8 to 18.5 *MBq* [215]. Therefore, after mixing the measured amount of [^{18}F]-FDG with tap water, the filling process was meticulously performed using a syringe. Both openings were unsealed, and the syringe needle was alternately inserted into each one to prevent the formation of air bubbles. If necessary, any bubbles formed were removed using ultrasound. As previously noted, calibration scans were conducted once every two weeks.

Image Quality phantom

The IQ phantom, defined by NEMA guidelines, is a detailed physical phantom specifically designed for calculating image quality parameters relevant to the imaging application of this study. Essentially, its purpose is to simulate the image obtained in whole-body imaging of a small rodent with small hot lesions: the phantom is considered equivalent to a mouse in terms of size and shape, being also filled with the same amount of radioactivity as the uniform phantom (in this case 14.8-18.5 *MBq*), to mimic the conditions of the animal imaging [215]. Its use, along with the specific parameters to be calculated and reported, is recommended by NEMA guidelines [211].
The phantom was built from PMMA, with internal dimensions of 50 *mm* length and 30 *mm* diameter and a total fillable volume of 19.5 *mL*. It consists of three parts, each used to analysee a different aspect of image quality:

1. **Uniform region**: one end of the cylinder is a fillable cylindrical chamber with 30 *mm* length (Section 2 in **Figure 4.15**). This region is used to calculate the percentage standard

deviation (%STD) (standard deviation divided by mean multiplied by 100), a measure of noise [211].

2. **Rods region** - the remaining 20 *mm* consist of a solid part with 5 fillable capillaries of different diameters (1-2-3-4-5 *mm*). Each capillary is centred 7 *mm* away from the cylinder centre. This region is used to calculate the recovery coefficient (RC) (the ratio of observed to true activity) [211].

3. **Cold regions** - a lid attached to the large end of the uniform region supports two hollow cylinders, one filled with air and the other with non-radioactive water (to simulate attenuation only). These cold regions, each measuring 15 *mm* in length and 8 *mm* of internal diameter, are used to calculate the spill-over ratio (SOR) (activity concentration in the cold region relative to the concentration in the hot background).

Additionally, there is a lid on the opposite side (the one with rods), which facilitates the removal of trapped air bubbles and aids in drying. The top lid (uniform side) is closed with three screw caps equipped with rubber circular gaskets to prevent liquid leakage. Tap water mixed with a measured amount of [^{18}F]-FDG was used as the filling liquid (the same as for uniform phantom). The filling of the phantom was done inside the hot cell using a 20 *mL* syringe, inserted into the uniform region opening, applying slow and constant pressure to prevent the formation of air bubbles. Tap water mixed with a measured amount of [^{18}F]-FDG was used as the filling liquid (the same as for uniform phantom). To enhance visibility during filling and to detect any bubbles (which were subsequently removed using ultrasound), water was coloured with a small amount of blue dye (trypan blue) (**Figure 4.16**). Moreover, as a small trick, two drops of non-foaming detergent were added to the solution, to reduce surface tension and fill the capillaries easily without bubbles. According to recommendations, the IQ phantom was scanned quarterly in this study, totalling two scans [210].

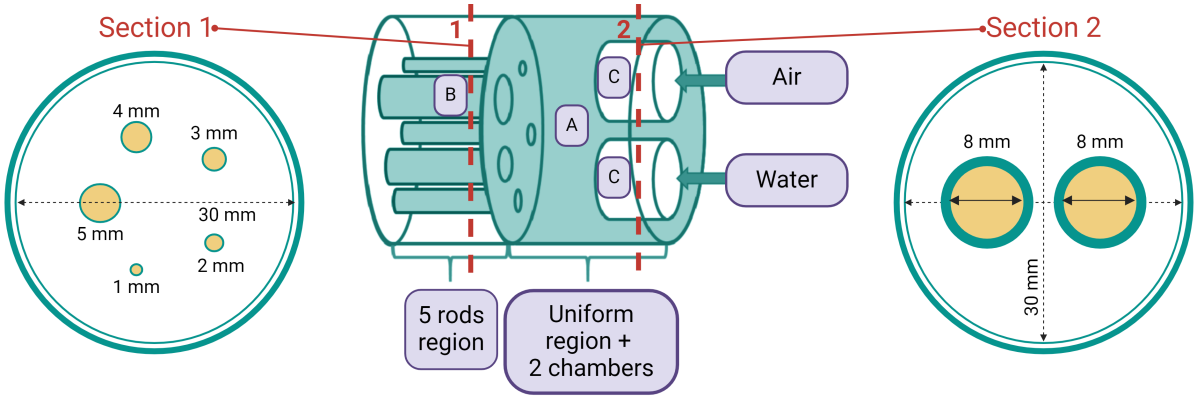

Figure 4.15: IQ phantom structure scheme, with the two described transverse sections (adapted from [216]) (created with BioRender.com).

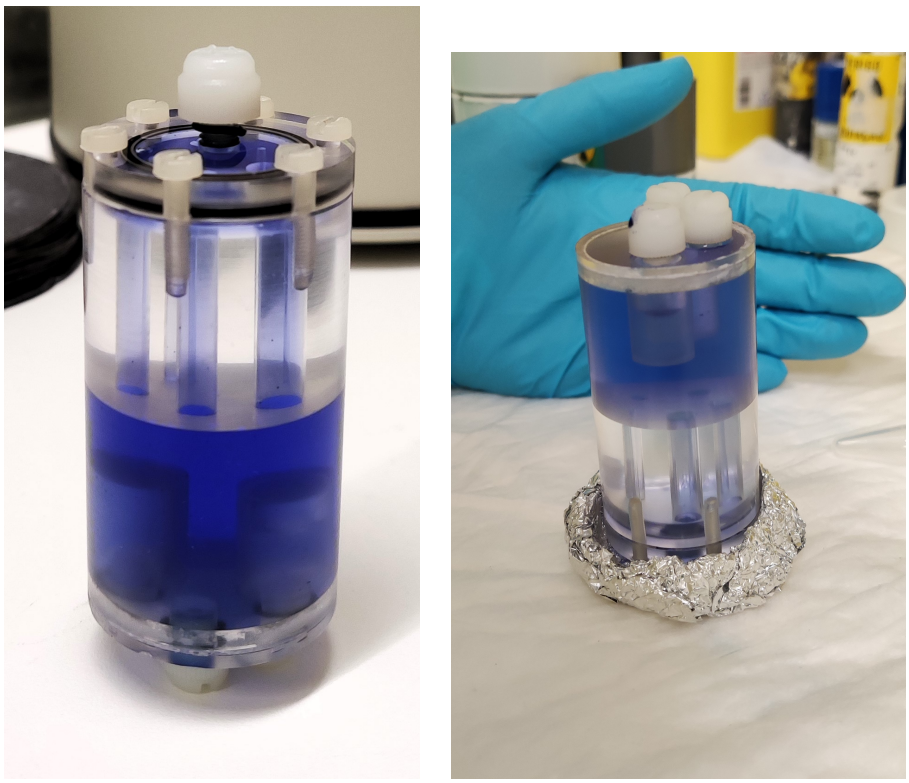

(a) (b)

Figure 4.16: IQ phantom filled with solution (tap water plus [^{18}F]-FDG). Blue dye was useful to assess its proper filling within the capillaries.

Phantoms imaging

The image acquisition and reconstruction process was consistent for both phantoms. It started by filling in basic information about each phantom (volume, measured activity, and time of measurement) into the easyPET.3D software. Subsequently, the phantom was positioned inside the easyPET.3D bed (conditioned in its dedicated holder), aligning its axis with the FoV main axis. The acquisition of phantom images began with a short scan (*quickscan*) for 5-10 minutes. This initial scan aimed to obtain a preliminary image, to identify any obvious anomalies and ensure correct positioning of the phantom. Following adjustments to the position, if necessary, a longer scan was initiated. The phantom acquisition typically took place at the end of the day, with the scan running overnight. NEMA guidelines emphasize the importance of reconstructing phantom images using the standard algorithm and parameters employed for mouse image processing [211]. Accordingly, the parameters selected for each phantom are detailed in **Table 4.2** and **Table 4.3**. To maintain consistency and comparability with mouse imaging, the same software (AMIDE) was chosen for image processing.

4.3. Results and discussion

This section presents results obtained during the *in vivo* experiments. Ten animals were used in this experiment, divided into two groups: Control (**A**) and Experimental (**B**) (details in

Table 4.2: Parameters used for uniform phantom reconstruction. The system matrix is used to reconstruct the projections. It characterizes the relationship between sources and data by linking each volume element (b_j) in the image space to each LoR (d_i), corresponding to a pair of detectors, in the projection space. Each term $p(b_j, d_i)$ of the $N \times M$ system matrix, represents the probability that an event generated in the region defined by b_j has of being detected by a detector pair d_i [194].

Algorithm	LM-MLEM
Iterations	25
Voxel size	$1.00 \times 1.00 \times 1.07\ mm^3$
Energy window	350-650 keV
System matrix size	$45 \times 45 \times 68$
Transverse FoV	$40\ mm$

Table 4.3: Parameters used for IQ phantom reconstruction.

Algorithm	LM-MLEM
Iterations	25
Voxel size	$1.00 \times 1.00 \times 1.07\ mm^3$
Energy window	350-650 keV
System matrix size	$40 \times 40 \times 68$
Transverse FoV	$35\ mm$

subsection 4.2.2 on page 59). Animals were matched in couples between **A** and **B**, but results were grouped only considering no GTE/GTE administration, according to the chosen chemotherapeutical protocol. Given the small sample sizes ($n_A = 6$, $n_B = 4$), data are reported descriptively. For each index or factor, the average value (mean) and its variability (standard deviation) are indicated. A larger sample size is necessary to avoid weak statistical power. However, observations with descriptive value that may offer insights into the regarding specific tested protocols will be made while analysing the results. The processing of results included: (i) analysis of the trend of mice weight throughout the study; (ii) analysis of the measurement of tumours superficial sizes (using a calliper); (iii) quantitative analysis of the PET imaging data.

While evaluating longitudinal data, time $t = 0$ was set at the beginning of the chosen therapy. Throughout the baseline period (before treatment), all mice underwent identical housing and handling protocols. The study aimed to collect data over time (longitudinal) to investigate potential differences in response to the administered treatment between the two groups. The main softwares used during these steps were Microsoft Excel® (*Version 2402 Build 16.0.17328.2012*) for data arrangement into spreadsheets, MATLAB (*Version: 9.12.0.1884302, R2022a*) for graphical analysis, and AMIDE (*AMIDE's a Medical Image Data Examiner, amide.exe 1.0.6*) for PET images. A preliminary analysis was performed on the IQ phantom images to assess the ability of the PET scan to detect small-sized tumours. This evaluation preceded the examination of the PET data.

4.3.0.1. Weight monitoring

It is noteworthy that the mean time that mice needed to develop a visible tumour at the naked eye was 7.70 $\pm$ 2.21 days, confirming the high tumorigenic power of WiDr cells. Furthermore, between the cells' injection and the treatment initiation, none of the animals showed weight loss: the mean ratio between the weight at $t = 0$ and the weight at the time of treatment administration was 1.0 $\pm$ 0.02. The raw data of the weights of groups **A** and **B** are shown in the upper panel of **Figure 4.17**. Since the time points were not correspondent and varied in number, to retrieve the mean trend of the weight of each group, the following procedure was followed:

1. the mean survival time of each group was calculated;
2. the t-axis was set with a time point every two days, until the mean survival time;
3. for each animal, available data were linearly interpolated on the t-axis;
4. the mean and standard deviation of interpolated data were calculated.

The results of the procedure are shown in the lower panel of **Figure 4.17**. Looking at the upper panels, it can be noticed that the longest survival time was 28 and 25 days for groups **A** and **B**, respectively. The animal surviving the longest without GTE treatment was the one treated with IRI [180 mg/m^2], whereas the longest survival for the opposite group was obtained with the FOLFIRI regimen. Both groups showed the shortest survival time (5 and 4 days for groups **A** and **B**, respectively) in animals treated with 5-FU [600 mg/m^2]+CFA [1,000 mg/m^2]. The treatment that improved the most the survival time between **A** and **B** was FOLFIRI (8 days in group **A**, *versus* 21 days in group **B**), followed by 5-FU [400 mg/m^2] + *CFA* [1,000 mg/m^2]. Two out of six control animals survived after the second cycle of the treatment (day 14), whereas three out of four animals taking GTE survived this threshold. The mean survival was 12.83 $\pm$ 8.70 days for group **A** and 16.25 $\pm$ 9.14 days for group **B**. Regarding the weights, it is evident that animals that survived the longest are also the ones whose weight remained more constant. All animals presented an overall weight loss during the study. This weight loss could be associated with the known side effects of chemotherapy, including diarrhoea, which was observed in half of them [217, 218]. Diarrhoea can lead to dehydration and decreased nutrient absorption, potentially contributing to weight loss. The weight pattern of the mice treated with 5-FU [600 mg/m^2] + CFA [1,000 mg/m^2], for both groups, confirms that this treatment was too aggressive, probably due to the high concentration of 5-FU that increased side effects: as soon as these animals were treated, their weight diminished from day to day. The most effective treatments according to the animals' weights were IRI for group **A** and 5-FU [400 mg/m^2] + CFA [1,000 mg/m^2] for group **B**. The middle panel of **Figure 4.17** proves that data, coming from a small sample, are considerably dispersed, obviously suggesting a sample size enlargement. The overall evaluation shown by the means (**Figure 4.18**) shows that GTE was effective in slowing down the side effects of chemotherapeutics, which resulted in a contrasting action towards weight loss. In fact, after a fast decrease soon after the first treatment administration, the weight, even if reduced, remained almost constant until the second treatment cycle. The low peak at day 4 (group **B**)

could be due to the influence of the administration of 5-FU $[600\ mg/m^2]$ + CFA $[1,000\ mg/m^2]$, whose weight reduced considerably during that day, leading to his death. On the other hand, the clear effect of chemotherapy is a constant reduction of weight: the curve reaches a *plateau* only when the weight of the animal is very low (approximately 16.7 g) (humane endpoint).

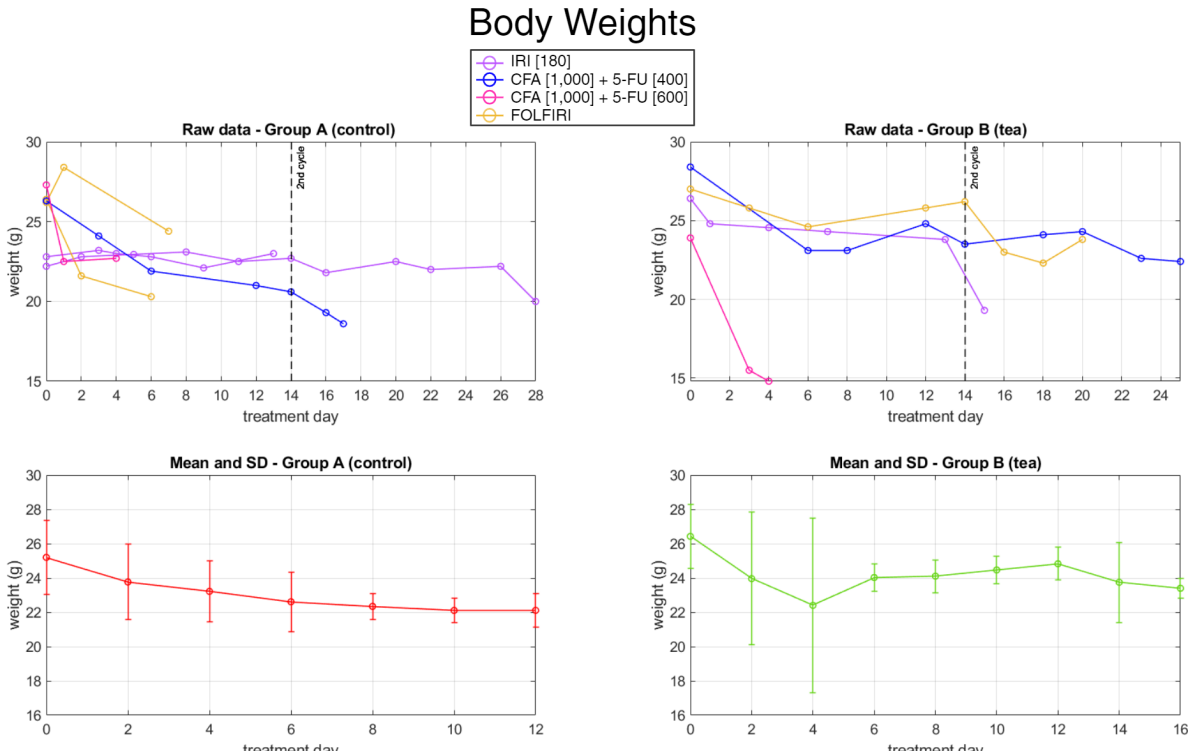

Figure 4.17: Body Weights - raw data are in the upper panels, whereas error bars retrieved from interpolated data are in the lower panels. The concentration of chemopharmaceuticals is expressed in mg/m^2 (generated with MATLAB).

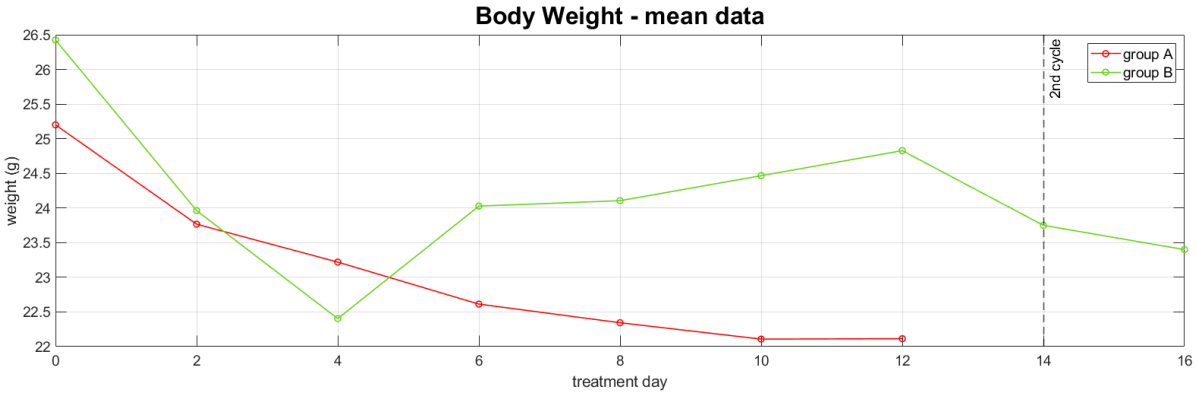

Figure 4.18: Average trend of body weight data (generated with MATLAB).

4.3.1. Tumour volume monitoring

Calliper measurements were sone with the same frequency as weights, *i.e.*, approximately twice a week, or more often if needed due to visible changes in tumour sizes. The collected length

(L) and width (W) tumour measurements were used to calculate the tumour volume through the formula [139]:

$$V = \frac{\pi}{6} \times L \times W^2 \tag{4.4}$$

Corresponding to weight measurement timing, calliper measurements were treated in the same way, and the mean pattern was calculated using interpolation on a t-axis with time points separated by two-day intervals. The results of the aforementioned averaging procedure are shown in **Figures 4.19** and **4.20**. Analysis of the data suggests that there may be no correlation between tumour volume and mouse survival: the slope of the curves near their right end is not evidently increasing in most cases (unlike body weight, which strongly decreased close to death). The two animals surviving the longest showed a common trend: soon after the first chemotherapeutic injection, tumour size increases, then it slightly decreases and starts to increase again after the second treatment cycle. Observing the animal treated with 5-FU $[600\, mg/m^2]$ + CFA, it can be noted that while the control mouse showed rapid tumour growth, the experimental one did not. On the other hand, the FOLFIRI regimen seems to help counteract tumour growth: the experimental animal treated with this cocktail showed both an almost constant tumour size and longer survival time than its control counterpart, suggesting that GTE could have had a synergistic effect with the chemopharmaceutical. The chemotherapy acted against the tumour while avoiding the mouse's health status from decreasing too much.
Overall, none of the tested treatments was able to eliminate the tumour or shrink it until it became not visible to the naked eye: all animals died/were occised showing a well-visible tumour mass. The error bars are still dispersed, especially in the last time points where data become fewer and fewer. The most interesting result can be observed in the mean pattern obtained after interpolation (**Figure 4.20**): once more, GTE seems to have an overall positive effect of slowing down the increase in tumour size, especially 6 days after the first treatment administration. The peak for the **B** group occurs before the peak for the **A** group, being also strongly lower. Then, after this peak, a slight decrease is followed by another increase, which starts becoming faster after the second cycle (this shows the strong influence of the longest survivor on the mean, since they are the only ones contributing to data in the last time period).
Finally, it should be reminded that tumour measurements, even if they were always taken by the same expert operator, are less objective and precise than body weight data, which were measured by a scale. The calliper measurement in this specific study was possible because the tumour remained encapsulated and superficial thanks to the subcutaneous injection. However, as tumour growth was not only superficial but also happened in depth, pressing on the underlying tissue, one portion of it was not visible superficially. This was evident especially for tumours that superficially showed multiple lobes, comproved when they were retrieved (animal necropsy), the actual tumour was a unique mass, all joined below the surface and developing into small 'spheres ,superficially.

However, volumetric data were not the focus of the experiment, since they were used as an aid to the segmentation of PET images, as discussed below.

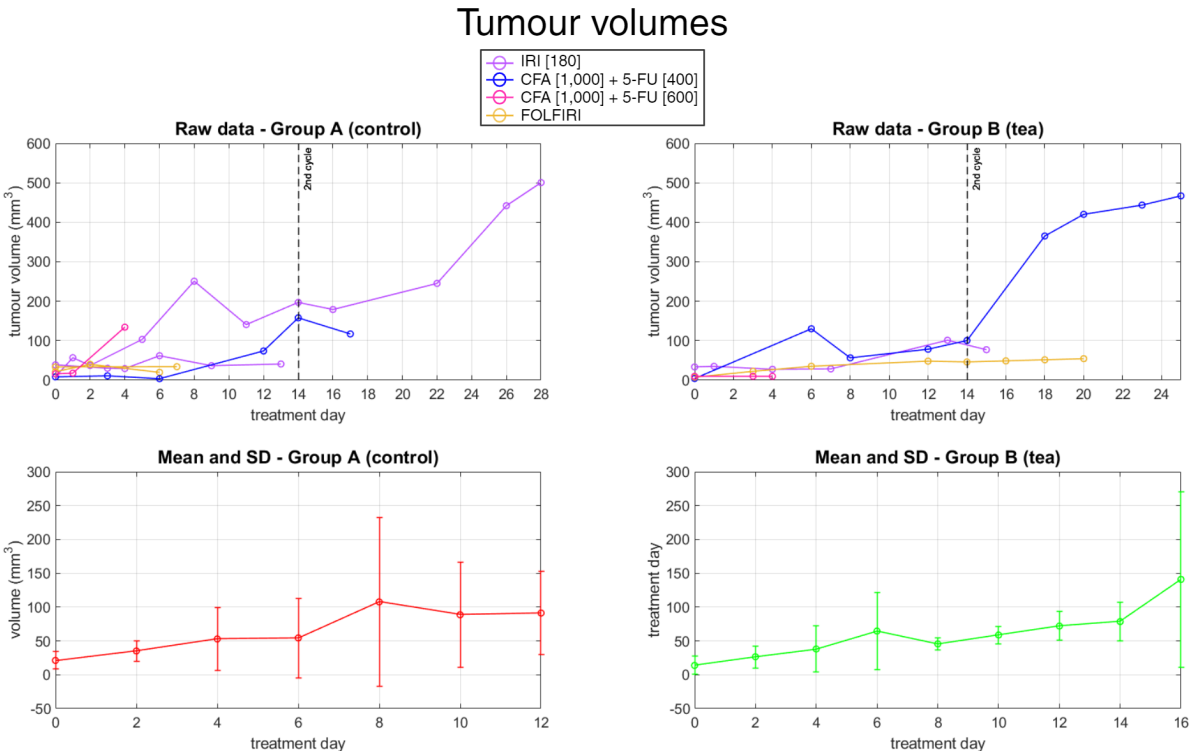

Figure 4.19: Tumour volumes - raw data are in the upper panels, whereas error bars retrieved from interpolated data are in the lower panels. The concentration of chemopharmaceuticals is expressed in mg/m^2 (generated with MATLAB).

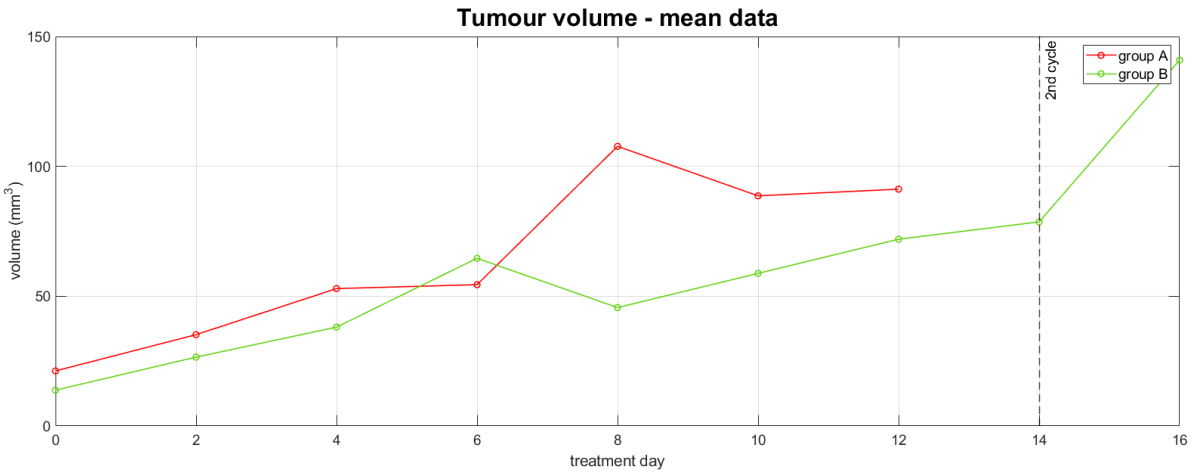

Figure 4.20: Average trend of tumour volume (generated with MATLAB).

4.3.2. Preliminary assessment of scanner's resolution

Before imaging data evaluation, the image obtained with the IQ phantom was analysed, thus demonstrating that the scanner could detect tumour masses as small as those in the animals. To maintain consistency with the studies carried out in the group at this stage, AMIDE was used for visualizing all the PET images. It is a basic tool for assessing quantitative indexes; hence, it was not possible to do the performance assessment suggested by NEMA, as more detailed measurements and data are needed, such as the position of the maximum pixel in the selected ROIs. However, the IQ phantom can be used to mirror the size, radiotracer, and amount of radioactivity injected into the mice. Actually, the phantom shown in **Figure 4.22a** began the scan with an amount of radioactivity of 18.20 MBq, higher than the mean amount of radioactivity with which a mouse usually starts image acquisition (10.35 MBq). Therefore, to do a more reliable comparison, the first 73 minutes of the image acquisition were excluded while reconstructing the image[24]. Now that the phantom and the mouse images match an equal amount of radioactivity, it is possible to take the phantom as a simulation of the animal imaging. The reconstructed image was, therefore, imported into AMIDE, cropped to a size consistent with the phantom size (thus removing the background blur), and properly rotated to be aligned with the axial FoV from each perspective (transverse, coronal, and sagittal - **Figure 4.21**). The obtained image was useful for qualitatively assessing the spatial resolution: the minimum visible capillary in the transverse section of **Figure 4.22b** is the 2 mm one; this means that the smallest distinguishable detail level in a mouse image is 2 mm. This evaluation is consistent with the tumour sizes detected in the present study since 2 mm was the approximate tumour size when the animal started the treatment. This was only a preliminary qualitative evaluation of the PET tomograph uncertainty; therefore, more detailed NEMA measurements should be performed using more sophisticated software (like PMOD) [219].

4.3.3. Animal PET image analysis

After ascertaining the resolution of the easyPET.3D system, animal images acquired throughout the study were analysed to evaluate the tumour metabolic activity in response to the tested treatments.

Images were acquired weekly for mice. The experiment, like many others, encountered deviations from the planned procedures. For instance, not all tracer injections were successful: in some cases, the i.p. injection did not achieve the desired distribution, as the radiotracer was trapped either by the animal's digestive system (deeper i.p. administration due to the usual anatomical position of the *cecum*) or in the fatty tissue of the abdomen (superficial i.p. administration; some males have more fat over the abdomen than others), compromising the resulting image and impairing its analysis (**Figure 4.23**).

Therefore, in this section, neither means nor standard deviations were calculated. The evaluation

[24]The time necessary to achieve this equality was calculated using the radioactive decay law: $N_t = N_0 \times e^{-\lambda t}$, knowing the initial and final desired amounts of radioactivity (N_0 and N_t) and the decay constant of ^{18}F ($\lambda = 1.05 \times 10^{-4}$).

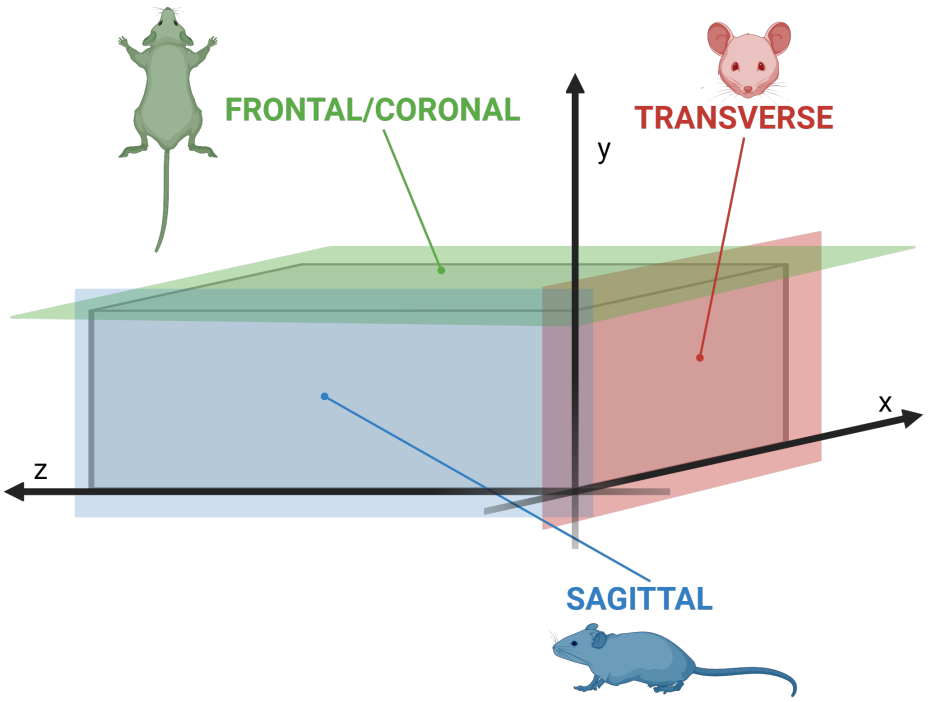

Figure 4.21: Schematization of the anatomical planes considered in the present work: they are arranged according to the mouse body anatomy, being useful for evaluating PET images. The sagittal plane provides a lateral view, dividing the body into right and left portions. The transverse plane divides the body into anterior and posterior portions. The frontal/coronal plane gives a top view of the animal, dividing it into dorsal and ventral portions (adapted from [220]) (created with BioRender.com).

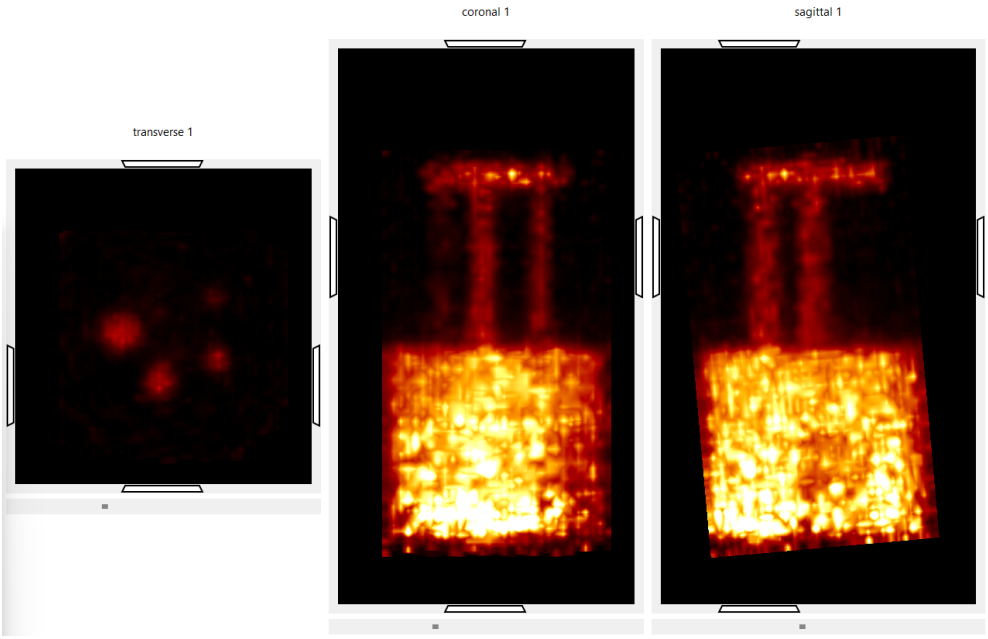

(a)

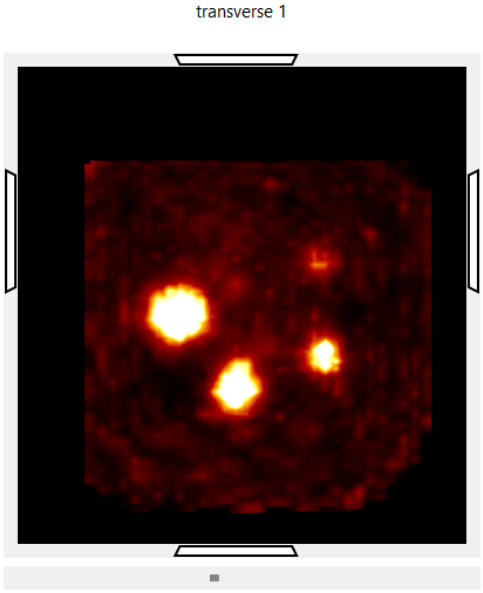

(b)

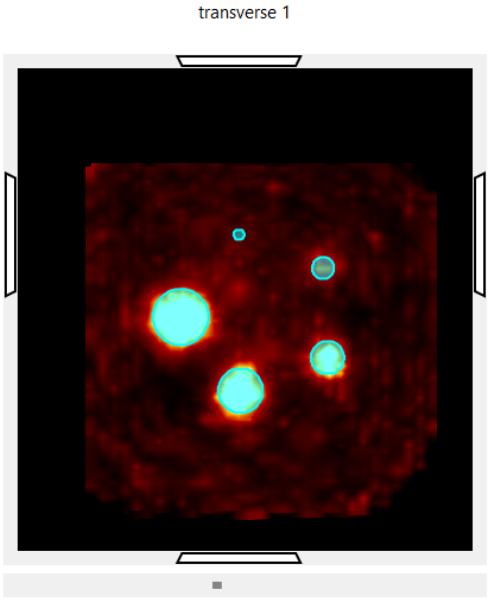

(c) The represented ROIs have diameters equal to the rods' diameters.

Figure 4.22: Images representing the IQ phantom, obtained after applying a global thresholding. Visualized data are referred to $10\,mm$ thick slices, obtained by the trilinear interpolation and mip (maximum intensity projection) rendering method.

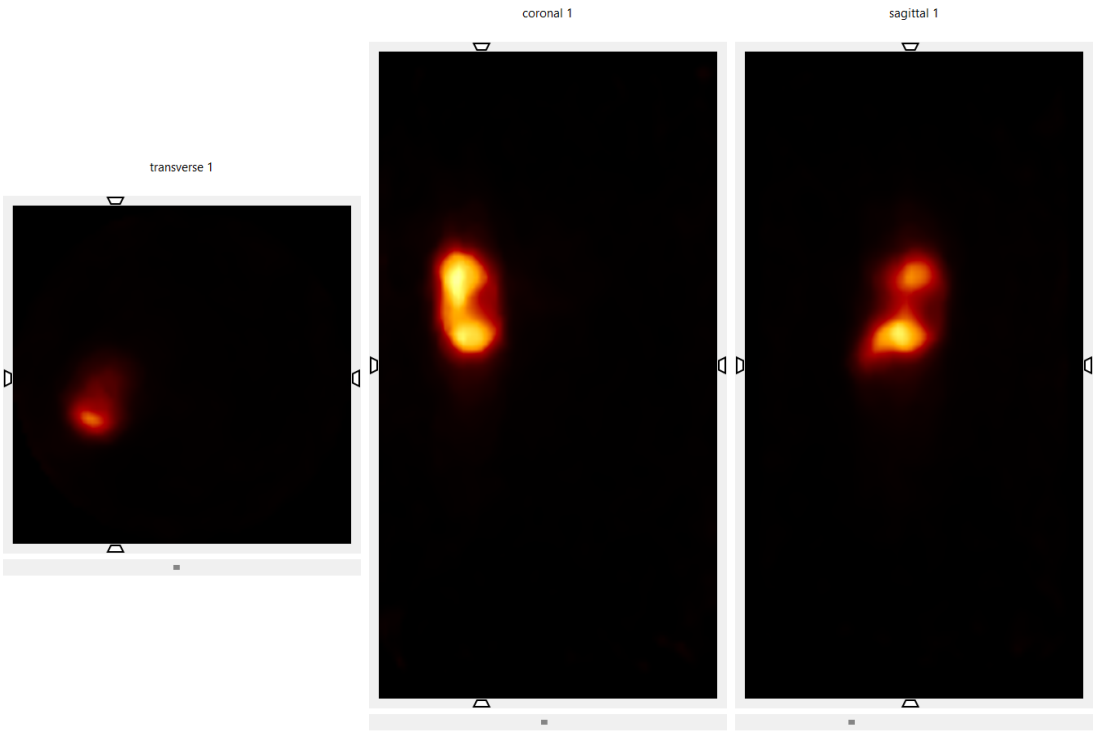

Figure 4.23: An example of unprocessable image, due to the radiotracer uptake by the animal's digestive system.

of results will focus on a qualitative description of data regarding each pair of mice[25] (one from group **A** and one from group **B**) matched according to the chemotherapeutic treatment. After their reconstruction, images were loaded onto AMIDE for processing. They were visualized using the hot metal colour scale. The processing began by drawing an ellipsoidal ROI corresponding to the animal bladder, the site on which the radiotracer uptake was most evident since [^{18}F]-FDG is excreted mainly via the kidneys. This ROI was then masked and removed to overcome this problem and allow an easier identification of the tumour mass (**Figure 4.24**). Then, the image ("without" the bladder) was filtered using a median-3D filter (kernel size = 3) to improve its quality. This filter demonstrates good performance in eliminating speckle noise while preserving edge definition in the image.

Using a global thresholding technique to adjust the intensity and allow visualizing hotter areas more evidently, the tumour mass was identified. Herein, conjugating the view of the image with the corresponding calliper measurement (performed on the same day), the tumour mass was localized, and a ROI was drawn manually to contour all the tumour mass, trying to include all hotter pixels. It should be remarked that the expression ROI is referred to the fact that PET image slices were represented through a 2D visualization on AMIDE, and each drawn ROI corresponds to a 3D volume of interest (VoI) (**Figure 4.25**).

While evaluating the images and looking for the tumour, it was considered that the i.p. injection of [^{18}F]-FDG was made on the left side of the mouse to avoid confusing eventual source of radioactivity in this area with the small tumour mass located on the right. Then, AMIDE evaluated the selected ROI statistics, providing the mean activity of the ROI, its number of

[25] A pair of animals per chosen chemodrug protocol. See future perspectives in **chapter 5**, page 97.

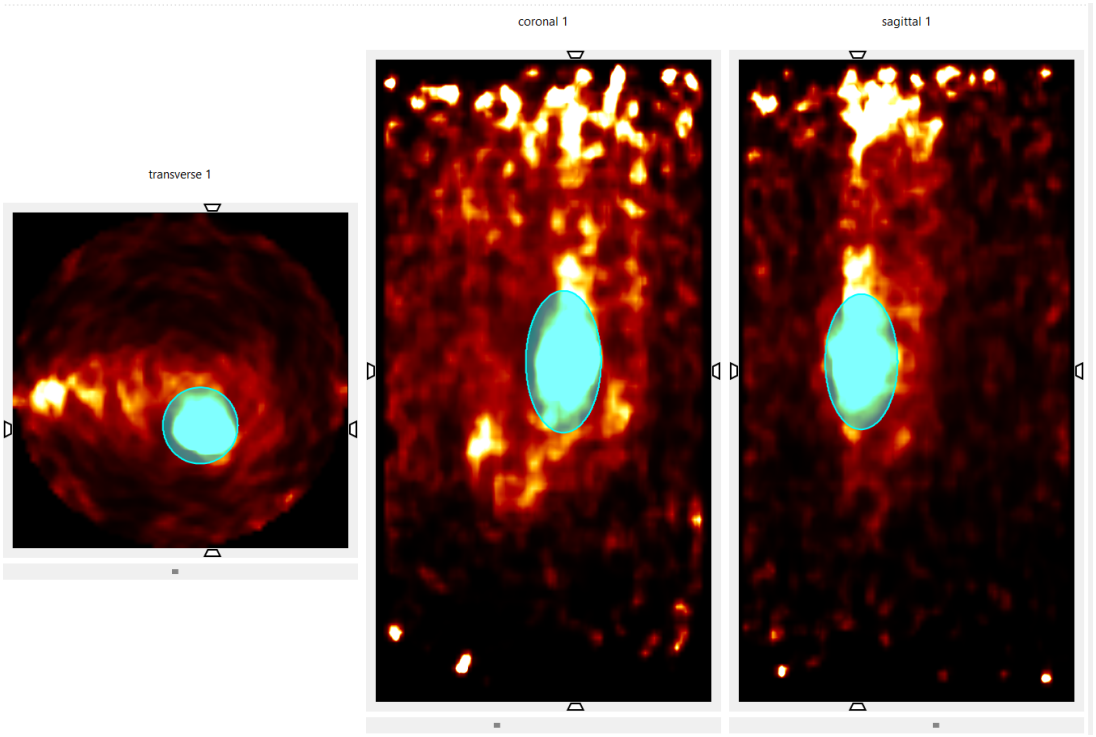

Figure 4.24: Ellipsoidal ROI correspondent to the bladder of the animal: it was masked as it is a hot area that would mislead the image interpretation.

voxels, and the ROI volume. Hence, an Excel spreadsheet was used to consolidate all acquisition times, radioactivity data, and AMIDE data, and **Equation 4.2** (page 75) was used to calculate the corresponding SUV_{mean} for each ROI. The quantitative evaluation was performed considering the SUV_{mean} to maintain consistency and comparability with previous studies carried out by the research group. It should be reminded that a higher SUV is indicative of higher glycolytic activity of the tumour tissue.

All the graphs presented were generated with MATLAB and correlate volume data to SUV_{mean} data. Volume data were obtained by linearly interpolating available volume data on the t axis with time points corresponding to single days (same procedure described in the former paragraph). On the other hand, SUV_{mean} data were visualized against a time axis corresponding to weeks instead of days (since data were collected weekly, as already emphasized[26]). In the upper panels of the graphs, black dots highlight volume data corresponding to the images acquisition days.

4.3.3.1. Protocol: CFA + 5-FU

In the subsequent evaluation, the analysis of the pair of animals administered with CFA $[1,000\ mg/m^2]$ + 5-FU $[600\ mg/m^2]$ will not be considered. Since they survived only 5 and 4 days (group A and B, respectively), these animals underwent only one PET image, and both images failed, resulting in an unprocessable outcome. Herein, **Figure 4.26** only shows the results for the couple of animals treated with the same protocol but with a lower concentration of

[26]Animal image acquisition has been made weekly for each mouse taking into account several facts: to reduce the anaesthetic and radioactive doses - do not forget the animal welfare rules and the possible complications; the number of animals studied for this work and other ones in course simultaneously at the Institute; the availability of [^{18}F]-FDG.

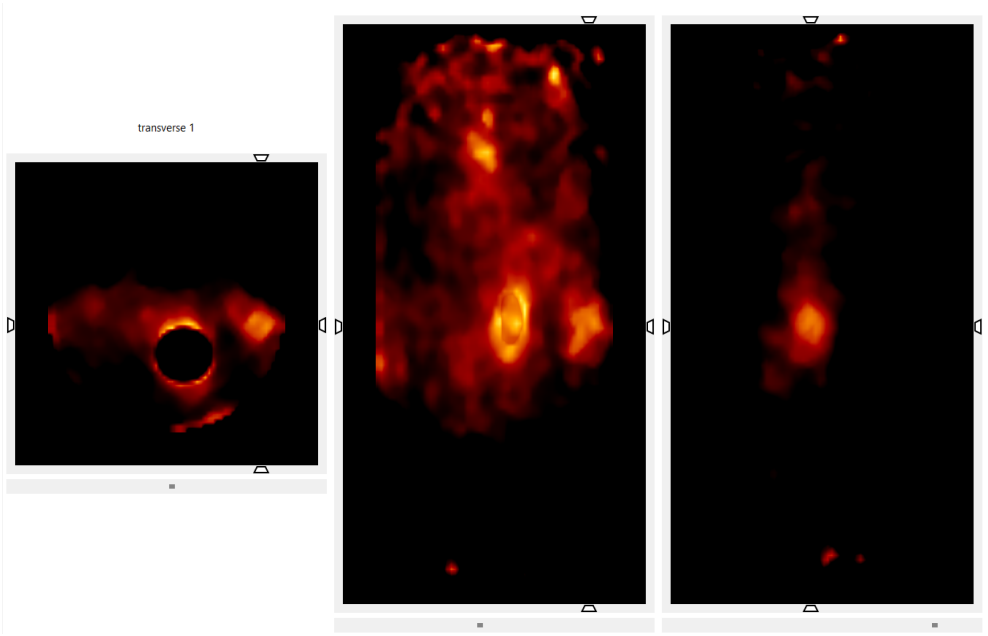

(a)

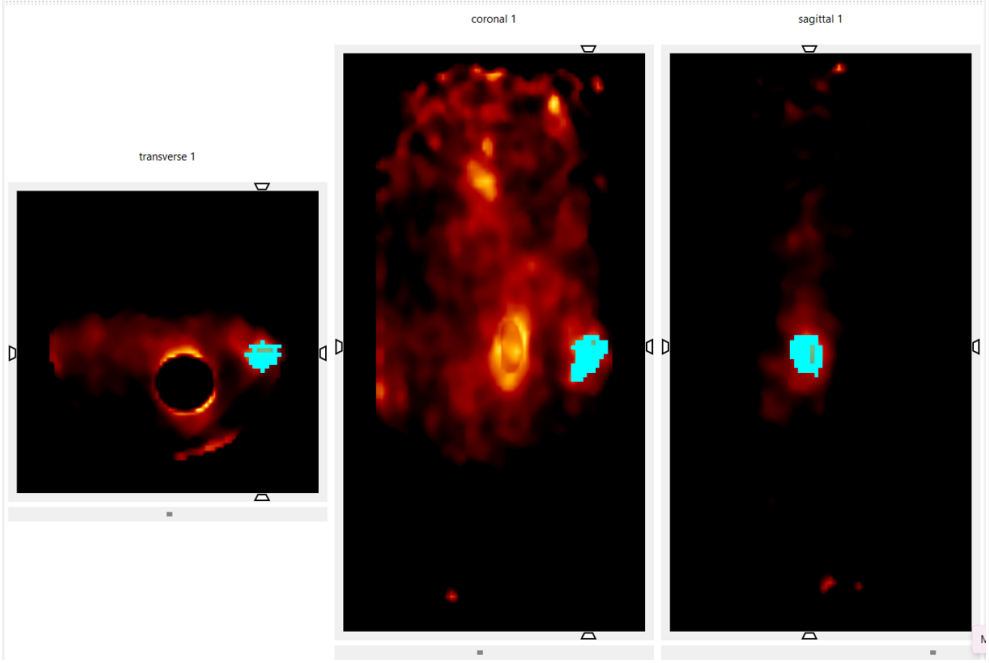

(b)

Figure 4.25: Manually drawn ROIs to segment the tumour.

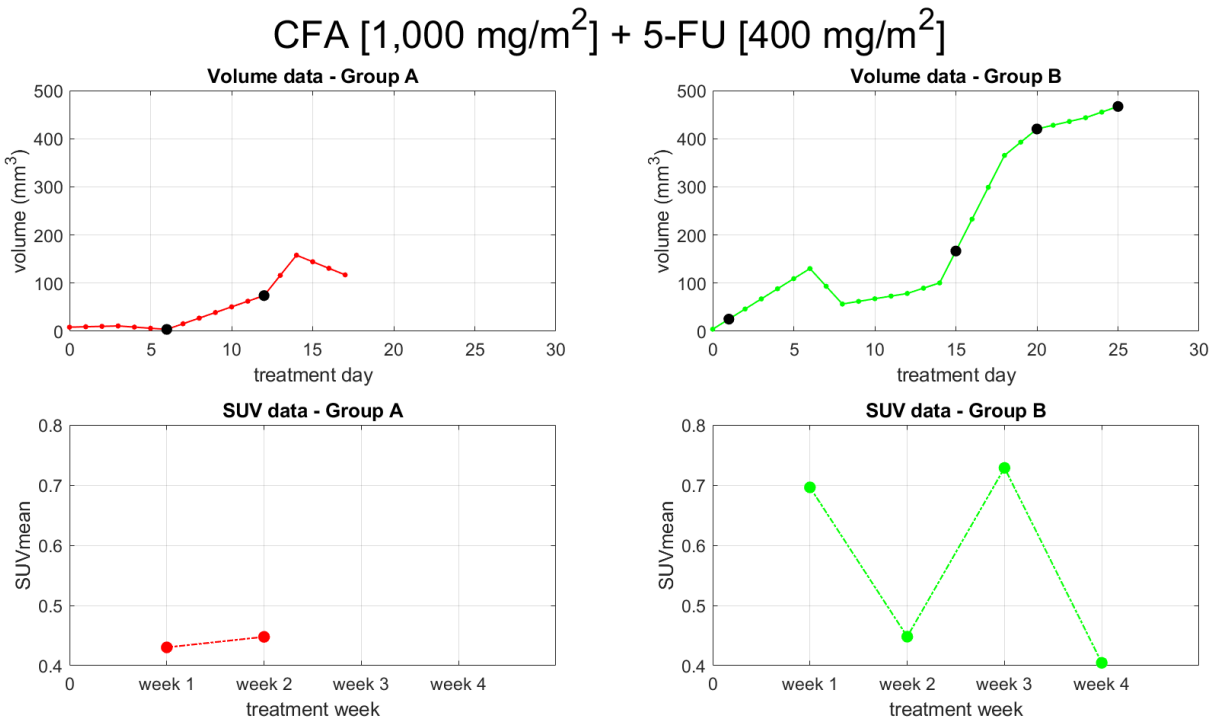

Figure 4.26: CFA $[1{,}000\ mg/m^2]$ + 5-FU $[400\ mg/m^2]$. Results of the quantitative assessment of PET imaging, coupled with volume measurements obtained using a calliper, are presented. The volume graph was created by interpolating available data on a t axis, with time points corresponding to each day. Black dots in the upper panels highlight the imaging days (generated with MATLAB).

5-FU: $[400\ mg/m^2]$. 5-FU has many side effects, as previously reported, and it is also a clinical approach to use a lower dose trying to overcome the situation, while treating the patient with this chemodrug. This will lead to tumour management difficulties (the size of the tumour may not reduce as quickly as expected), but will enable a longer survival. Regarding group **A** (left panel), the SUV seems to follow a trend similar to the volume trend: between the two images, it increases by 4.1%, which corresponds to the volume increasing as well (volume in image **2** is 19.4 times the volume in image **1**). This could indicate that the tumour metabolic activity, despite the treatment, became more intense as the tumour grew in size. This is reasonable since a larger tumour size suggests a higher number of malignant cells. Regarding collateral effects on the animal, this treatment led to skin dryness and weakness, as in humans. As the tumour reached a humane endpoint, occision by anaesthetic overdose was performed.

On the opposite side of the graph, an unexpected trend is observed: even as the tumour increases in size (6 times increase between the first and second image), its SUV and, therefore, its metabolic activity, seems to have considerably decreased by 35.6%. Subsequently, the SUV trend becomes consistent with the volume trend between the second and third images (2.2 times increase in volume and 62.6% increase in SUV mean). Finally, in the last interval, while the tumour continues to grow (by 11.1%), the SUV decreases (by 44.5%). This contrasting behaviour could be a hint to the effect of GTE: it did not help to reduce the size of the tumour, but it may have contributed to reducing the malignancy of cancer cells, counteracting their action. Furthermore, it could be argued that the second image, which shows a low peak of SUV, was

acquired the day after the second cycle of chemotherapy, suggesting that GTE may have acted as an adjuvant to the treatment. This feature will be enlightened by histopathological analysis, which is programmed.

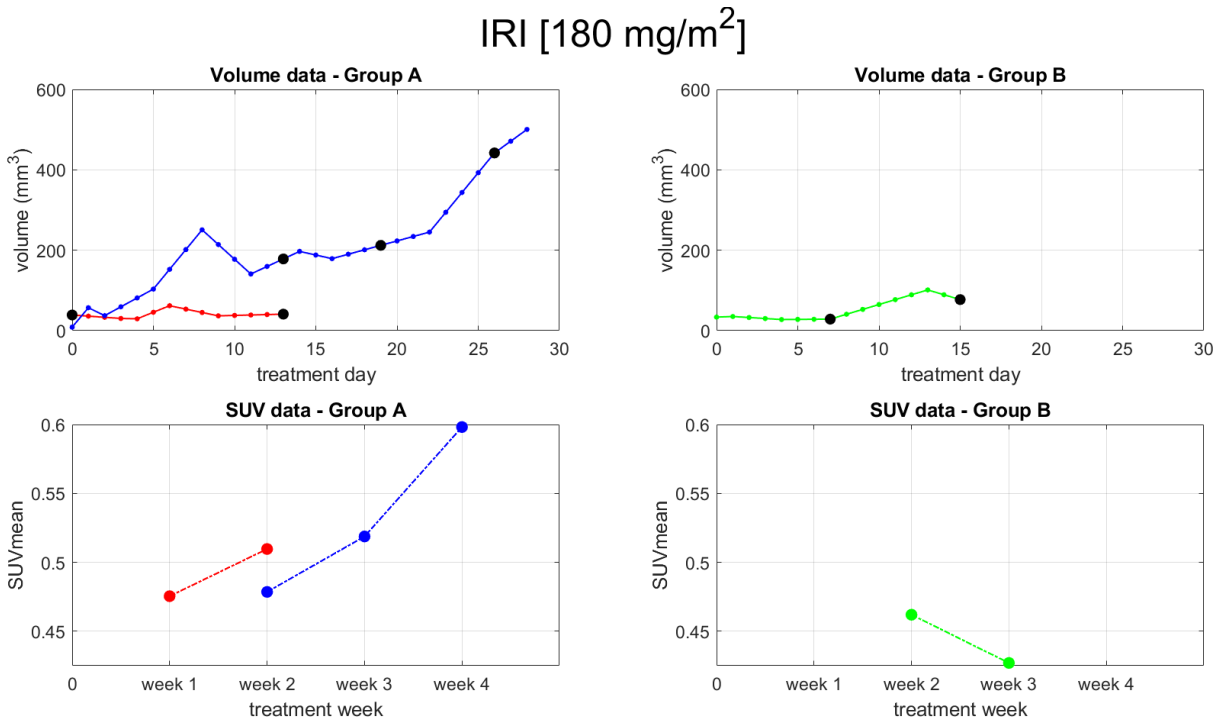

Figure 4.27: IRI $[180\,mg/m^2]$. Results of the quantitative assessment of PET imaging, coupled with volume measurements obtained using a calliper, are presented. The volume graph was created by interpolating available data on a t axis, with time points corresponding to each day. Black dots in the upper panels highlight the imaging days (generated with MATLAB).

4.3.3.2. Protocol: IRI

Data reported in **Figure 4.27** pertain to three animals, as this treatment was tested in three animals: two belonging to the control group (**A**) and one belonging to the experimental group (**B**). Regarding the data of the control group, one animal (blue data) shows an increasing SUV_{mean} between the first two images (+8.41%), consistent with the volume pattern (+18.9%). The same trend is observed between the second and third week: during this interval, the volume doubles and the SUV_{mean} shows an increase of 15.4%. This is consistent not only with the tumour size but also with the fact that the tumour of this animal developed neovascularization (tumour nutritional new vessels), as shown in **Figure 4.28**. The other animal (red data) shows metabolic activity comparable to the previous animal, despite the smaller size of the tumour: between the two images, both the tumour volume and the SUV_{mean} increase (+5.4% and +7.2%, respectively). On the other hand, the tumour volume of the animal belonging to the opposite group almost triplicates between the two acquisitions. This contrasts with the SUV, which experiences a 7.6% decrease. As observed in the previous protocol, this image was acquired one day after the second treatment cycle. It could be hypothesized that the treatment was effective in reducing the metabolic activity, and that GTE could have enhanced this effect. However, this had a strong

Figure 4.28: Mouse treated with IRI on the 27th day of study. The tumour is visibly irrigated by many vessels.

impact on the animal, inducing hypothermia and weakness, and lead to its death soon after the image acquisition. Anaesthesia also induces hypothermia, even using the warming system coupled to the easyPET.3D during image acquisition and warming in post-anaesthesia recovery. All the necessary procedures to image acquisition were strainful, considering the chemodrug own side effects.

4.3.3.3. Protocol: FOLFIRI

Even though the FOLFIRI conjugation was tested on three animals (two belonging to the control group and one belonging to the experimental group), the data in **Figure 4.29** only represent two mice: one control mouse survived only a week after the treatment and underwent a single PET scan, which failed. The represented control animal shows a volume pattern that was unique among all observed data: between the first and the second acquisition, the tumour decreased in size by 7.6%. However, the SUV_{mean} behaves oppositely, almost doubling (98.0% increase) between the first and the second week. This is the first time that the SUV_{mean} increases so remarkably, suggesting very high metabolic activity despite the tumour smaller volume. On the contrary, the experimental animal shows a concordant behaviour of the tumour volume and the PET data between the first two images (30.8% increase in volume and 16.2% increase in SUV_{mean}). However, between the second and fourth week, the two become discordant. As the tumour volume increases by 3.6 times, the SUV_{mean} experiences a 40.3% decrease. This still occurs after the second treatment cycle. A further image taken during week 3 could have given a deeper insight into this behaviour, but unfortunately it was not possible due to the lack

of radiotracer[27]. The histopathological analysis will help to clarify the PET results. From previous experience in other cases, this usually is due to the efficacy of the treatment, leading to fibroadipose tissue replacing tumoural tissue. Connective and adipose cells do not uptake [^{18}F]-FDG as much as the tumour, being much less metabolic active. Further data could prove this hypothesis.

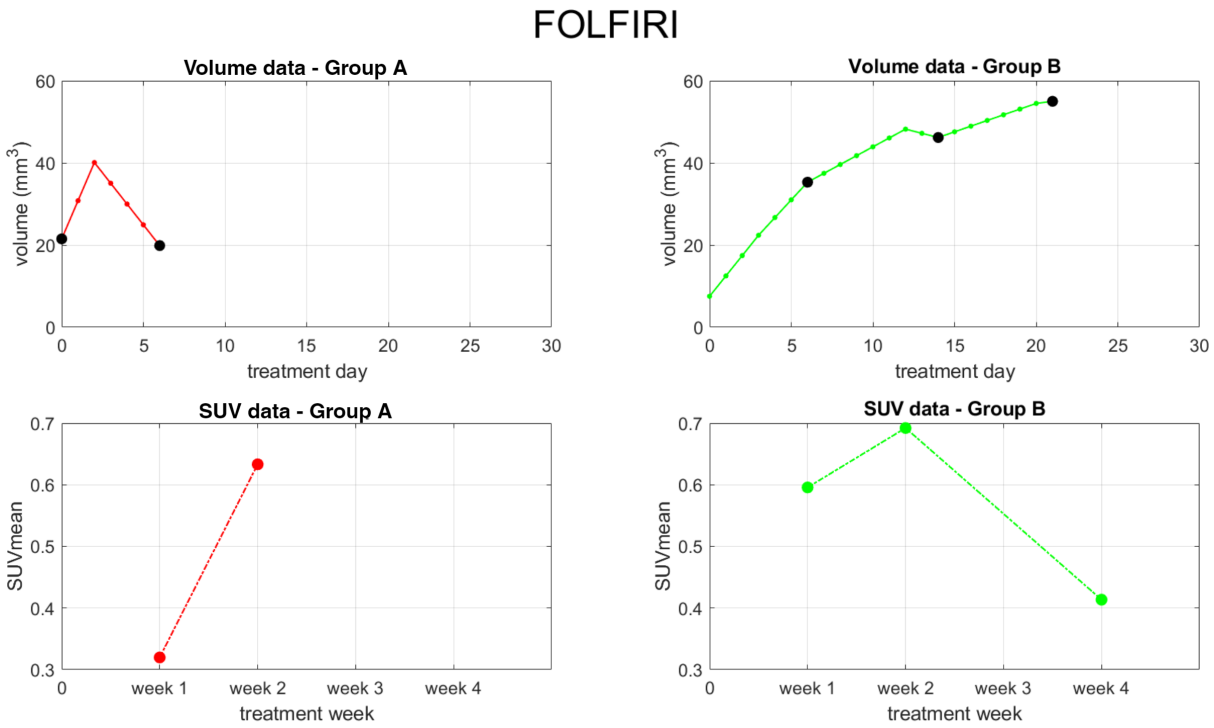

Figure 4.29: FOLFIRI regimen (Irinotecan $[180\,mg/m^2]$ + 5-Fluorouracil $[400\,mg/m^2]$ + Leucovorin $[200\,mg/m^2]$). Results of the quantitative assessment of PET imaging, coupled with volume measurements obtained using a calliper, are presented. The volume graph was created by interpolating available data on a t axis, with time points corresponding to each day. Black dots in the upper panels highlight the imaging days (generated with MATLAB).

4.3.3.4. Final considerations

This was a preliminary animal study following the *in vitro* experiments. Three protocols were chosen: **CFA+5-FU** (higher dosage of 5-FU = 600 mg/m^2), **IRI** and **FOLFIRI**. The study was designed to have three animals per chosen protocol per group pair (**A** and **B**). A first pair per protocol has been started, according to WiDr cells' availability. In what concerns the first protocol, **CFA+5-FU**, a second attempt has been made using a reduced dose of 5-FU (400 mg/m^2) in face of the animals' poor response.

A conjugation of several factors meant that the study design had to consider only one pair of animals per chosen protocol. First, the reduced number of nude male mice, which were possible to be provided by the *Vivarium*, due to colony reproduction problems. Second, the availability of WiDr cells due to a malfunction in the CO_2 supply system to the incubator used, which lead

[27] As previously noted, the radiotracer comes from the hospital after patient's PET exams. On that particular day there was an emergency patient, hence not enough radioactive dose remained for the animal study.

to the interruption of the cell culture. Third, since the chemodrugs are supplied by the hospital (given the existing collaboration agreement with the Biophysics Institute, previously mentioned), there are not always surpluses or patients being treated with these protocols.

Hence PET data had to be cautiously interpreted. Some general observations can be made across the three protocols, particularly within the same groups. The most notable observation is that, while the control group never showed an increasing tumour volume corresponding to a decreasing SUV_{mean}, the experimental group did. This decrease in SUV_{mean} was consistently observed after the second treatment cycle, as well as shortly before mouse death: in two cases, mice did not recover from aneasthesia, while in one case, the animal was occised due to humane endpoint. A competing explanation could be the animal's impending death due to weakness, potentially leading to a more pronounced response to anaesthesia. Interestingly, two out of four control animals succumbed in the same way, without a corresponding increase in SUV_{mean}.

A comprehensive understanding of these findings may be achieved by integrating them with the results of histopathological analysis: the tumours were collected and their histopathology is being finished. If necrosis/fibroadipose tissue replacement of the tumour is observed, it could indicate that, despite its apparent size, the decreased SUV_{mean} could be explained by the necrotic/cell replacement effects of the treatment towards WiDr cells. Additionally, histopathological observations of the control animal treated with FOLFIRI could justify the cellular behaviour leading to a reduced tumour size coupled to an enhanced SUV_{mean}.

Furthermore, the most interesting results were observed in animals that survived the longest, as the second cycle of chemotherapy appeared to become the most effective. Therefore, after evaluating which chemotherapeutical protocols (without/with GTE conjugation) yielded the best results, this study could be repeated trying to ensure longer survival of the animals and a more complete longitudinal dataset.

Increasing the number of animals per group will make the study more robust, enabling a more informed analysis of results.

In summary, the encouraging result of this evaluation in such a short time was the observed decrease in SUV_{mean}, which could potentially become an *in vivo* measure of the metabolic response of the tumour to therapy [156]. Additionally, another positive outcome of the study was the assessment of the easyPET.3D system's ability to detect small 'hot' volumes.

5 Conclusions and future directions

The main goal of the present work was to evaluate GTE as an adjuvant to standard chemotherapy treatment against CRC, both *in vitro* and *in vivo*. All experiments utilized the WiDr cell line, derived from human CRC, known for simulating the tumour growth *in vitro*, and the development in a complex *in vivo* environment like an animal's body. The results of *in vitro* assays generally do not demonstrate the adjuvant effect of GTE po towards chemotherapy, as cytotoxicity did not increase in most cases. Nevertheless, it is crucial to note that GTE did not significantly interfere with the cytotoxicity of the tested chemotherapeutic agents, enabling the cocktails to still kill over 50% of cells. This suggests GTE's potential to improve patients' quality of life if taken regularly, given its multiple beneficial effects. In fact, statistical significance does not necessarily imply no clinical relevance. Additionally, *in vivo* results were promising: animals treated with tea exhibited longer survival, slower tumour growth, and reduced bodyweight loss. However, none of the tumours disappeared due to the treatment. PET data yielded intriguing results: only GTE-treated animals exhibited increased tumour volume, coupled with a decrease in the SUV_{mean}, indicating potentially reduced tumour metabolic activity post-treatment. Planned histopathological studies may clarify this decrease in SUV_{mean}, providing insight into tumour cells behaviour. Lastly, it's worth noting that the preliminary evaluation of easyPET.3D spatial resolution proved beneficial in accurately detecting small tumours of 2 *mm* dimensions.

Certainly, during these experiments, the 3 Rs rule was considered. Tumours were allowed to grow in mice, as the intention was to observe the action of GTE coupled with chemotherapy in these specific, harsh situations.

5.1. In vitro studies

During *in vitro* assays, WiDr cells, seeded in flat-bottom culture plates, were stimulated with several GTE po concentrations to assess its impact on cell viability alongside chemotherapeutic protocols. Control wells contained cells incubated solely in culture medium.

5.1.1. Protocol: CFA + 5-FU

Concerning the CFA + 5-FU protocol, the mechanism of CFA *in vitro* was not expressed, as it was not metabolically activated by hepatic enzymes. However, combining CFA and 5-FU resulted in cytotoxicity, both alone and with GTE po. The concentration of 5-FU is crucial, either for good or bad effects, in this combination. It has been reported, as previously stated, that although 5-FU shows the greatest effectiveness against CRC, its active metabolites, which disrupt DNA and RNA synthesis through the folate pathway, only lead to a 10-15% response rate in advanced cases. As cancer cells develop resistance to 5-FU through several mechanisms, limiting its effectiveness as a single therapy, its combination with other drugs offers a more potent approach.
The worst results in this protocol have been obtained using the highest 5-FU dose of the clinics ($600\ mg/m^2$), usually delivered in a dose-intensive schedule with metastatic or unresectable colorectal carcinoma, suggesting that a higher dose is not always more effective and, above all, could cause important adverse events also in human treatment. In fact, 5-FU is primarily responsible for patient side effects, including diarrhoea, fever, and mucositis.
For other tested 5-FU concentrations (400–$550\ mg/m^2$), despite coupling with GTE po, chemotherapy agents' cytotoxicity was preserved or slightly reduced, still inducing over 50% cell death. No statistically significant differences were found between different GTE po concentrations, favouring lower concentrations for further studies. Another potential strategy could be a further reduction of 5-FU concentration to determine if it maintains its cytotoxic effect when combined with CFA and GTE po. Animal studies used 5-FU concentrations in the range of $[400 - 600\ mg/m^2]$. Despite less success with the highest concentration, further *in vivo* testing, focusing on a dose-intensive regimen, was pursued. Poor results would have led to its exclusion from future research.

5.1.2. Protocol: IRI

Regarding IRI alone, the lowest concentration ($180\ mg/m^2$) was, *in vitro*, once again the best, considering a trade-off between data dispersion and good cytotoxicity; therefore, it was also tested *in vivo*.

5.1.3. Protocol: FOLFIRI

The FOLFIRI protocol revealed that this combination, when coupled with GTE po, slightly decreased cytotoxicity, but it remained below the IC_{50} threshold. Hence, this protocol was the third one tested on animals.

5.2. In vivo studies

The *in vivo* experiments were based upon a non-orthotopic animal model using BALB/c(-) athymic male mice (nude mice) to evaluate combining chemotherapeutic protocols with GTE.

The impact if the treatment on the animals was assessed monitoring their weight, tumour volumes, and PET imaging using easyPET.3D. Cells were inoculated s.c. to mimic a primary tumour. The four aforementioned protocols were tested, but due to limited animal availability, groups were divided only based on GTE intake. Statistical evaluations were restricted to mean and standard deviations because of the small sample size. Overall, GTE showed a mean effect of prolonged survival, slower weight loss, and tumour growth in animals. However, those treated with 5-FU ($600\ mg/m^2$) and CFA ($1,000\ mg/m^2$) survived only a few days, suggesting this treatment should be discarded.

In addition to these measurements, a fundamental aim was the evaluation of the tumour response using PET imaging. Before analysis, a parallel evaluation of the easyPET.3D tomograph itself was conducted. Due to time constraints and the simplicity of the software used (AMIDE) for image processing, NEMA measurements were not feasible. In future studies, more sophisticated software like PMOD could replace AMIDE. Nevertheless, a qualitative evaluation of the scanner's performance was possible using the IQ phantom, which contained a similar radioactive dose as that injected into the mice. It was concluded that the smallest visible detail size is 2 *mm*. Following this evaluation, images were analyzed using the SUV_{mean} metric, calculated with manual segmentation of the tumour. The limited amount of data hindered a comprehensive interpretation; however, it was observed that only animals consuming GTE exhibited in some cases an increase in tumour volume corresponding to a decreased SUV_{mean}. This suggests that the treatment may effectively reduce tumour metabolic activity, particularly after the second treatment cycle. Nonetheless, SUV can be influenced by various biological factors, including blood-glucose level and plasma activity curve. A future task involves concluding efficacy evaluation through optical microscopic observation of histological samples now in stock. If signs of tumour necrosis are found in samples, this could confirm and explain the observed reduction in SUV_{mean}.

5.3. Limitations and future directions

5.3.1. In vitro studies

Regarding future perspectives *in vitro*, testing reductions of the best doses could help to assess the efficacy of lower doses of chemo-agents and their potential positive effects when coupled with GTE. Further assessment of appropriate dosage should be also conducted *in vivo*, where studies on GTE bioavailability can be performed.

The MTT assay was considered appropriate for addressing the research question and was the only tool used to extract quantitative information from *in vitro* studies in these preliminary experiments. However, MTT and its optical density measured at the end are influenced by various factors, including cell growth phase and extracellular reduction of the reagent. To ensure the specificity of the results, complementary tests should be conducted to obtain more detailed information about the type of cell death and the cell cycle phase at the time of death. Cell cytometry assays could be a solution.

Overall, the *in vitro* setting demonstrates intrinsic limitations due to its simplicity and inability to account for all enzymes and complex interactions present naturally in the human body, especially considering the heterogeneity and multifactorial nature of CRC. Nonetheless, this step of the study was fundamental as it allowed for quick screening of multiple protocols, facilitating the selection of those to be tested *in vivo*.

5.3.2. In vivo studies

During the *in vivo* experiments, four protocols were tested in a limited number of animals. Now that some have been excluded (CFA $[1,000\ mg/m^2]$+5-FU $[600\ mg/m^2]$), future research could focus on more promising protocols (IRI, CFA $[1,000\ mg/m^2]$+5-FU $[400\ mg/m^2]$, and FOLFIRI). Increasing the number of tested animals would enhance statistical reliability and allow continued screening to reject unsuccessful protocols. Additionally, more robust data could provide deeper insights into the effects of GTE on chemotherapy and its side effects.

Animal model

The first recommendation is to design more complete experiments by scheduling a PET image approximately 5-6 days after cell inoculation (7.7 days being the mean time to develop a visible tumour) to compare SUV_{mean} values pre- and post-treatment. In fact, all animals underwent PET scans when the tumour was already visible to the naked eye. Hence, thanks to the ability of the easyPET system, even smaller developing tumours, not visible externally, could be detected.
To enhance the number of usable PET scans per animal, using isoflurane anaesthesia instead of the used injectable mixtures could speed up recovery and reduce complications.
The study design could be further strengthened by standardizing initial conditions within each group, ensuring uniform starting tumour sizes and increasing measurement frequency to more than twice a week. Additionally, more precise assessments could be achieved through methods like planar fluorescence imaging instead of manual measurement[1].
Being non-orthotopic, the model could not fully replicate the human tumour environment due to the discrepancy between the tumour location in humans and animals. However, leveraging easyPET.3D technology, it will be possible to ascertain the tumour's onset, progression, and response to therapy over time.
It must be also considered that cancer is highly heterogeneous, even within the same type: WiDr cells may not fully capture the diversity of human CRC. Other CRC cell lines, such as HT-29, offer a more characterized and widely used model. Comparing results obtained with different cell lines regarding chemotherapy protocols and GTE combination could provide valuable insights. Moreover, patient-derived xenografts (PDXs) present a promising model which involve

[1] Fluorescence imaging is a type of optical imaging designed to visualize the spatial distribution of substances that emit fluorescence (fluorochromes). In this technique, the animal is injected with a fluorescent probe that specifically targets the tumour tissue. Subsequently, a light source of appropriate wavelength excites the fluorochromes, and a detection system performs spectral and spatial separation to differentiate and resolve the fluorescence emitted from the fluorescent substances [221].

transplanting tumour tissue from CRC patients into immunodeficient mice. This, genetic and pathological features of the original tumour are preserved, allowing for personalized medicine research.

PET imaging

An aspect to consider is the potential for false-negative findings in [^{18}F]-FDG/PET imaging, which can arise due to factors such as inflammation. During image evaluation, misleading hot regions near the tumour area were observed, underscoring the need to consider this characteristic while analyzing the images.
The main limitation regarding the image analysis performed in this work was the use of PET scans alone: they provided functional information, challenging to be interpreted alone. To achieve a more comprehensive and reliable interpretation, anatomical information is essential. The integration of anatomical data could be achieved by coupling an X-ray source to the easyPET.3D tomograph to perform a Computed Tomography (CT) scan, thus obtaining a multimodal image. In fact, while analysing the PET images, an alike strategy was tried, using a CT mouse (with fur) image from a free atlas online. However, it was difficult to overimpose[2] it to the PET scan, due to differences in mouse dimensions and weight loss of nude induced by chemotherapy.
The easyPET.3D system is undergoing continuous improvement, with ongoing integration of real-time monitoring features such as heart rate, oxygen saturation, and body temperature. These advancements will further enhance the quality and control of PET examinations.
Additionally, only manual segmentation was utilized in this work. Standardized and less time-consuming methods are preferred as they minimize operator dependence and reduce the risk of human error. Therefore, to achieve more consistent, reliable, and standardized results, the development of automatic methods for tumour segmentation is strongly recommended.
To sum up, Nuclear Medicine has confirmed its utilitv not only in human diagnostics, but also in preclinical studies. Moreover, the higher expertise in enhancing microPET systems' cost, sensitivity, resolution, and overall image quality, can be transposed into the clinical context. This development addresses limitations in clinical scanners, ultimately making the diagnostic technique more feasible and reliable for wider application.

5.4. Conclusions

The main conclusions that can be drawn from this preliminary analysis are listed below.

- The easyPET.3D system emerged as a valuable tool for longitudinal monitoring of the animal model, aligning perfectly with the 3Rs principles (Replacement, Reduction, and Refinement). This innovative technology offers high-quality preclinical data at an accessible price point, making it a feasible option for a wider range of research institutions.

[2]The overimposing process is called image co-registration. It is the process of geometrically aligning two or more images in order to integrate corresponding pixels representing the same objects [222].

- By combining *in vitro* and *in vivo* approaches, this preclinical investigation establishes a foundation for understanding GTE's potential therapeutic effects. It addresses the performance of the natural compound in terms of efficacy, *i.e.*, in controlled and ideal circumstances (such as the *in vitro* setting or the animal model). After improving the statistical power of these results with further investigation, the next step would be evaluating the effectiveness in real-world conditions.

Driven by the hope of improved outcomes, some cancer patients, with their oncologists' guidance, have already begun experimenting with combining GTE and chemotherapy. This preclinical study paves the way for a more rigorous investigation of this patient-driven approach. While these initial findings are encouraging, well-designed clinical trials are crucial to validate the safety and effectiveness of this combination therapy. Building on the groundwork laid by studies like this one, robust evidence will be essential to translate this promising strategy into a mainstream cancer treatment option.

References

[1] Luca Falzone, Salvatore Salomone, and Massimo Libra. "Evolution of cancer pharmacological treatments at the turn of the third millennium". In: *Frontiers in pharmacology* 9 (2018), p. 1300. DOI: 10.3389/fphar.2018.01300.

[2] International Agency for Research on Cancer. *Global Cancer Observatory: Cancer Today. Lyon, France: International Agency for Research on Cancer*. 2022. URL: https://gco.iarc.who.int/today/en/fact-sheets-cancers.

[3] Natalia Krasteva and Milena Georgieva. "Promising therapeutic strategies for colorectal cancer treatment based on nanomaterials". In: *Pharmaceutics* 14.6 (2022), p. 1213. DOI: 10.3390/pharmaceutics14061213.

[4] Tianyi Li and David Gal. "Consumers prefer natural medicines more when treating psychological than physical conditions". In: *Journal of Consumer Psychology* (2023). DOI: 10.1002/jcpy.1371.

[5] Erin Kayata. *How the Use of Alternative Medicine Hurts Survival Rates in Patients with Cancer*. 2019. URL: https://www.cancernetwork.com/view/how-use-alternative-medicine-hurts-survival-rates-patients-cancer.

[6] Skyler B Johnson, Henry S Park, Cary P Gross, and James B Yu. "Use of alternative medicine for cancer and its impact on survival". In: *JNCI: Journal of the National Cancer Institute* 110.1 (2018), pp. 121–124. DOI: 10.1093/jnci/djx145.

[7] Aakash Deep, Davinder Kumar, Nitin Bansal, Balasubramanian Narasimhan, Rakesh Kumar Marwaha, and Prabodh Chander Sharma. "Understanding mechanistic aspects and therapeutic potential of natural substances as anticancer agents". In: *Phytomedicine Plus* (2023), p. 100418. DOI: 10.1016/j.phyplu.2023.100418.

[8] Narayan Dolai, Aminul Islam, and Pallab Kanti Haldar. "Antiproliferative activity and apoptosis inducing mechanism of Anthocephalus cadamba on Dalton's lymphoma ascites cells". In: *Iranian Journal of Pharmaceutical Research: IJPR* 15.3 (2016), p. 505.

[9] American Cancer Society®. *American Cancer Society Guideline for Colorectal Cancer Screening*. Jan. 29, 2024. URL: https://www.cancer.org/cancer/types/colon-rectal-cancer/detection-diagnosis-staging/acs-recommendations.html.

[10] Maleesha Jayasinghe, Omesh Prathiraja, Dilushini Caldera, Rahul Jena, James Anwar Coffie-Pierre, Minollie Suzanne Silva, Ozair S Siddiqui, and James Anwar Coffie-Pierre Jr. "Colon Cancer Screening Methods: 2023 Update". In: *Cureus* 15.4 (2023). DOI: 10.7759/cureus.37509.

[11] Sam Al-Sohaily, Andrew Biankin, Rupert Leong, Maija Kohonen-Corish, and Janindra Warusavitarne. "Molecular pathways in colorectal cancer". In: *Journal of gastroenterology and hepatology* 27.9 (2012), pp. 1423–1431. DOI: 10.1111/j.1440-1746.2012.07200.x.

[12] NaNa Keum and Edward Giovannucci. "Global burden of colorectal cancer: emerging trends, risk factors and prevention strategies". In: *Nature reviews Gastroenterology & hepatology* 16.12 (2019), pp. 713–732. DOI: 10.1038/s41575-019-0189-8.

[13] Elena Lecumberri, Yves Marc Dupertuis, Raymond Miralbell, and Claude Pichard. "Green tea polyphenol epigallocatechin-3-gallate (EGCG) as adjuvant in cancer therapy". In: *Clinical nutrition* 32.6 (2013), pp. 894–903. DOI: 10.1016/j.clnu.2013.03.008.

[14] Chung S Yang, Xin Wang, Gang Lu, and Sonia C Picinich. "Cancer prevention by tea: animal studies, molecular mechanisms and human relevance". In: *Nature Reviews Cancer* 9.6 (2009), pp. 429–439. DOI: 10.1038/nrc2641.

[15] María Isabel Cerezo-Guisado, Rafal Zur, María Jesús Lorenzo, Ana Risco, Miguel A Martín-Serrano, Alberto Alvarez-Barrientos, Ana Cuenda, and Francisco Centeno. "Implication of Akt, ERK1/2 and alternative p38MAPK signalling pathways in human colon cancer cell apoptosis induced by green tea EGCG". In: *Food and Chemical Toxicology* 84 (2015), pp. 125–132. DOI: 10.1016/j.fct.2015.08.017.

[16] Bharat B Aggarwal, Yasunari Takada, and Oommen V Oommen. "From chemoprevention to chemotherapy: common targets and common goals". In: *Expert opinion on investigational drugs* 13.10 (2004), pp. 1327–1338. DOI: 10.1517/13543784.13.10.1327.

[17] Kala Nature®. *Camellia Sinensis Extract & Oil (Green Tea)*. 2024. URL: https://www.kala.bg/en-product-details-27.html.

[18] Kaja CG Berg, Peter W Eide, Ina A Eilertsen, Bjarne Johannessen, Jarle Bruun, Stine A Danielsen, Merete Bjørnslett, Leonardo A Meza-Zepeda, Mette Eknæs, Guro E Lind, et al. "Multi-omics of 34 colorectal cancer cell lines-a resource for biomedical studies". In: *Molecular cancer* 16 (2017), pp. 1–16. DOI: 10.1186/s12943-017-0691-y.

[19] Justas Žilinskas, Darius Stukas, Aldona Jasukaitienė, Inga Žievytė, Zbigniev Balion, Jurgita Šapauskienė, Rasa Banienė, Henrikas Paužas, Paulius Lizdenis, Vaidotas Čėsna, et al. "Assessing the Therapeutic Impacts of HAMLET and FOLFOX on BRAF-Mutated Colorectal Cancer: A Study of Cancer Cell Survival and Mitochondrial Dynamics In Vitro and Ex Vivo". In: *Medicina* 60.1 (2024), p. 142. DOI: 10.3390/medicina60010142.

[20] Florian Bürtin, Christina S Mullins, and Michael Linnebacher. "Mouse models of colorectal cancer: Past, present and future perspectives". In: *World journal of gastroenterology* 26.13 (2020), p. 1394. DOI: 10.3748/wjg.v26.i13.1394.

[21] Lda - Radiation Imaging Technologies RI-TE. *intelligent PET scanner*. 2022. URL: https://www.ri-te.pt/ipet/.

[22] Robert C Hubrecht and Elizabeth Carter. "The 3Rs and humane experimental technique: implementing change". In: *Animals* 9.10 (2019), p. 754. DOI: 10.3390/ani9100754.

[23] Claude E Welch, Leslie W Ottinger, John P Welch, Claude E Welch, Leslie W Ottinger, and John P Welch. "Anatomy and physiology of the colon and rectum". In: *Manual of Lower Gastrointestinal Surgery* (1980), pp. 9–18.

[24] IARC (International Agency for Research on Cancer) - Working Group on the Evaluation of Cancer-Preventive Interventions. *Colorectal Cancer Screening*. 2019. Chap. 1. COLORECTAL CANCER. URL: https://www.ncbi.nlm.nih.gov/books/NBK553197/.

[25] Agata Gurba, Przemysław Taciak, Mariusz Sacharczuk, Izabela Młynarczuk-Biały, Magdalena Bujalska-Zadrożny, and Jakub Fichna. "Gold (III) derivatives in colon cancer treatment". In: *International Journal of Molecular Sciences* 23.2 (2022), p. 724. DOI: 10.3390/ijms23020724.

[26] Pedro Farinha, Jacinta O Pinho, Mariana Matias, and M Manuela Gaspar. "Nanomedicines in the treatment of colon cancer: A focus on metallodrugs". In: *Drug Delivery and Translational Research* (2021), pp. 1–18. DOI: 10.1007/s13346-021-00916-7.

[27] N Hugen, CJH Van de Velde, JHW De Wilt, and ID Nagtegaal. "Metastatic pattern in colorectal cancer is strongly influenced by histological subtype". In: *Annals of oncology* 25.3 (2014), pp. 651–657. DOI: 10.1093/annonc/mdt591.

[28] Vincenza Conteduca, Domenico Sansonno, Sabino Russi, and Franco Dammacco. "Precancerous colorectal lesions". In: *International journal of oncology* 43.4 (2013), pp. 973–984. DOI: 10.3892/ijo.2013.2041.

[29] Mark Schmitt and Florian R Greten. "The inflammatory pathogenesis of colorectal cancer". In: *Nature Reviews Immunology* 21.10 (2021), pp. 653–667. DOI: 10.1038/s41577-021-00534-x.

[30] Céline Hervieu, Niki Christou, Serge Battu, and Muriel Mathonnet. "The role of cancer stem cells in colorectal cancer: from the basics to novel clinical trials". In: *Cancers* 13.5 (2021), p. 1092. DOI: 10.3390/cancers13051092.

[31] Basanti Brar, Koushlesh Ranjan, Ankur Palria, Rajesh Kumar, Mayukh Ghosh, Sweety Sihag, and Prasad Minakshi. "Nanotechnology in colorectal cancer for precision diagnosis and therapy". In: *Frontiers in Nanotechnology* 3 (2021), p. 699266. DOI: doi.org/10.3389/fnano.2021.699266.

[32] Anna Lewandowska, Grzegorz Rudzki, Tomasz Lewandowski, Aleksandra Stryjkowska-Gora, and Sławomir Rudzki. "Risk factors for the diagnosis of colorectal cancer". In: *Cancer Control* 29 (2022), p. 10732748211056692. DOI: 10.1177/10732748211056692.

[33] Xiaoliang Wang, Kelli O'Connell, Jihyoun Jeon, Mingyang Song, David Hunter, Michael Hoffmeister, Yi Lin, Sonja Berndt, Hermann Brenner, Andrew T Chan, et al. "Combined effect of modifiable and non-modifiable risk factors for colorectal cancer risk in a pooled analysis of 11 population-based studies". In: *BMJ open gastroenterology* 6.1 (2019), e000339. DOI: 10.1136/bmjgast-2019-000339.

[34] Bao Tran, GBD 2017 Colorectal Cancer Collaborators, et al. "The global, regional, and national burden of colorectal cancer and its attributable risk factors in 195 countries and territories, 1990–2017: a systematic analysis for the Global Burden of Disease Study 2017". In: (2019). DOI: 10.1016/S2468-1253(19)30345-0.

[35] Raelene D Kennedy, D Dean Potter, Christopher R Moir, and Mounif El-Youssef. "The natural history of familial adenomatous polyposis syndrome: a 24 year review of a single center experience in screening, diagnosis, and outcomes". In: *Journal of pediatric surgery* 49.1 (2014), pp. 82–86. DOI: 10.1016/j.jpedsurg.2013.09.033.

[36] Kory W Jasperson, Thérèse M Tuohy, Deborah W Neklason, and Randall W Burt. "Hereditary and familial colon cancer". In: *Gastroenterology* 138.6 (2010), pp. 2044–2058. DOI: 10.1053/j.gastro.2010.01.054.

[37] V Fedirko, I Tramacere, V Bagnardi, M Rota, L Scotti, F Islami, E Negri, K Straif, I Romieu, C La Vecchia, et al. "Alcohol drinking and colorectal cancer risk: an overall and dose–response meta-analysis of published studies". In: *Annals of oncology* 22.9 (2011), pp. 1958–1972. DOI: 10.1093/annonc/mdq653.

[38] Chen Zhang, Yunjiu Cheng, Dongling Luo, Jinghua Wang, Jianhua Liu, Yujun Luo, Weijie Zhou, Zewei Zhuo, Kehang Guo, Ruijie Zeng, et al. "Association between cardiovascular risk factors and colorectal cancer: a systematic review and meta-analysis of prospective cohort studies". In: *EClinicalMedicine* 34 (2021). DOI: 10.1016/j.eclinm.2021.100794.

[39] DP Pozuelo-Carrascosa, C Alvarez-Bueno, I Cavero-Redondo, S Morais, IM Lee, and V Martinez-Vizcaino. "Cardiorespiratory fitness and site-specific risk of cancer in men: A systematic review and meta-analysis". In: *European Journal of Cancer* 113 (2019), pp. 58–68. DOI: 10.1016/j.ejca.2019.03.008.

[40] World Health Organisation. *Colorectal cancer - Key facts*. July 11, 2023. URL: https://www.who.int/news-room/fact-sheets/detail/colorectal-cancer.

[41] Jiexi Li, Zhengdao Lan, Wenting Liao, James W Horner, Xueping Xu, Jielin Liu, Yohei Yoshihama, Shan Jiang, Hong Seok Shim, Max Slotnik, et al. "Histone demethylase KDM5D upregulation drives sex differences in colon cancer". In: *Nature* (2023), pp. 1–8. DOI: 10.1038/s41586-023-06254-7.

[42] Anil Kumar, Vipasha Gautam, Arushi Sandhu, Kajal Rawat, Antika Sharma, and Lekha Saha. "Current and emerging therapeutic approaches for colorectal cancer: A comprehensive review". In: *World Journal of Gastrointestinal Surgery* 15.4 (2023), p. 495. DOI: 10.4240/wjgs.v15.i4.495.

[43] Yuan-Hong Xie, Ying-Xuan Chen, and Jing-Yuan Fang. "Comprehensive review of targeted therapy for colorectal cancer". In: *Signal transduction and targeted therapy* 5.1 (2020), p. 22. DOI: 10.1038/s41392-020-0116-z.

[44] Karuna Ganesh, Zsofia K Stadler, Andrea Cercek, Robin B Mendelsohn, Jinru Shia, Neil H Segal, and Luis A Diaz Jr. "Immunotherapy in colorectal cancer: rationale, challenges and potential". In: *Nature reviews Gastroenterology & hepatology* 16.6 (2019), pp. 361–375. DOI: https://doi.org/10.1038/s41575-019-0126-x.

[45] Leah H Biller and Deborah Schrag. "Diagnosis and treatment of metastatic colorectal cancer: a review". In: *Jama* 325.7 (2021), pp. 669–685. DOI: 10.1001/jama.2021.0106.

[46] Muhammad T Amjad, Anusha Chidharla, and Anup Kasi. "Cancer chemotherapy". In: (2020).

[47] Francine C Cadoná, Rafael Ferreira Dantas, Gabriela Haas de Mello, and Floriano Paes Silva-Jr. "Natural products targeting into cancer hallmarks: An update on caffeine, theobromine, and (+)-catechin". In: *Critical Reviews in Food Science and Nutrition* 62.26 (2022), pp. 7222–7241. DOI: 10.1080/10408398.2021.1913091.

[48] Elena Dickens and Samreen Ahmed. "Principles of cancer treatment by chemotherapy". In: *Surgery (Oxford)* 36.3 (2018), pp. 134–138. DOI: https://doi.org/10.1016/j.mpsur.2017.12.002.

[49] M Shields. "Chemotherapeutics". In: *Pharmacognosy*. Elsevier, 2017, pp. 295–313.

[50] Insaf Altun and Alper Sonkaya. "The most common side effects experienced by patients were receiving first cycle of chemotherapy". In: *Iranian journal of public health* 47.8 (2018), pp. 1218–1219.

[51] Shangui Liu, Abdur Rauf Khan, Xiaoye Yang, Bo Dong, Jianbo Ji, and Guangxi Zhai. "The reversal of chemotherapy-induced multidrug resistance by nanomedicine for cancer therapy". In: *Journal of Controlled Release* 335 (2021), pp. 1–20. DOI: 10.1016/j.jconrel.2021.05.012.

[52] Abid Naeem, Pengyi Hu, Ming Yang, Jing Zhang, Yali Liu, Weifeng Zhu, and Qin Zheng. "Natural products as anticancer agents: Current status and future perspectives". In: *Molecules* 27.23 (2022), p. 8367. DOI: 10.3390/molecules27238367.

[53] Nihal Ahmad and Hasan Mukhtar. "Green tea polyphenols and cancer: biologic mechanisms and practical implications". In: *Nutrition reviews* 57.3 (1999), pp. 78–83. DOI: 10.1111/j.1753-4887.1999.tb06927.x.

[54] Melanie Esselen and Stephan W Barth. "Food-borne topoisomerase inhibitors: risk or benefit". In: *Advances in molecular toxicology*. Vol. 8. Elsevier, 2014, pp. 123–171. DOI: https://doi.org/10.1016/B978-0-444-63406-1.00004-0.

[55] Ana R Nunes, Marco G Alves, Paula I Moreira, Pedro F Oliveira, and Branca M Silva. "Impact of green tea (Camellia sinensis L.) consumption in diabetes mellitus-induced neurodegeneration". In: *Green Tea and Health: Antioxidant Properties, Consumption and Role in Disease Prevention; Powell, N., Ed* (2015), pp. 1–33.

[56] Megha Bansal, Neha Singh, Saurabh Pal, Indra Dev, and Kausar Mahmood Ansari. "Chemopreventive role of dietary phytochemicals in colorectal cancer". In: *Advances in molecular toxicology* 12 (2018), pp. 69–121. DOI: 10.1016/j.biotechadv.2018.11.011.

[57] Hoyee Leong, Priya S Mathur, and Geoffrey L Greene. "Green tea catechins inhibit angiogenesis through suppression of STAT3 activation". In: *Breast cancer research and treatment* 117 (2009), pp. 505–515. DOI: 10.1007/s10549-008-0196-x.

[58] Jae-Wook Oh, Manikandan Muthu, Suraj Shiv Charan Pushparaj, and Judy Gopal. "Anticancer Therapeutic Effects of Green Tea Catechins (GTCs) When Integrated with Antioxidant Natural Components". In: *Molecules* 28.5 (2023), p. 2151. DOI: 10.3390/molecules28052151.

[59] Vondina R Moseley, Jay Morris, Rebecca W Knackstedt, and Michael J Wargovich. "Green tea polyphenol epigallocatechin 3-gallate, contributes to the degradation of DNMT3A and HDAC3 in HCT 116 human colon cancer cells". In: *Anticancer research* 33.12 (2013), pp. 5325–5333.

[60] Yue Chen, Xiao-Qian Wang, Qi Zhang, Jian-Yun Zhu, Yuan Li, Chun-Feng Xie, Xiao-Ting Li, Jie-Shu Wu, Shan-Shan Geng, Cai-Yun Zhong, et al. "(-)-Epigallocatechin-3-gallate inhibits colorectal cancer stem cells by suppressing Wnt/β-catenin pathway". In: *Nutrients* 9.6 (2017), p. 572. DOI: 10.3390/nu9060572.

[61] Heiying Jin, Wei Gong, Chunxia Zhang, and Shuiming Wang. "Epigallocatechin gallate inhibits the proliferation of colorectal cancer cells by regulating Notch signaling". In: *OncoTargets and therapy* (2013), pp. 145–153. DOI: 10.2147/OTT.S40914.

[62] Sumio Hayakawa, Tomokazu Ohishi, Noriyuki Miyoshi, Yumiko Oishi, Yoriyuki Nakamura, and Mamoru Isemura. "Anti-cancer effects of green tea epigallocatchin-3-gallate and coffee chlorogenic acid". In: *Molecules* 25.19 (2020), p. 4553. DOI: 10.3390/molecules25194553.

[63] Masahito Shimizu, Yohei Shirakami, Hiroyasu Sakai, Yoichi Yasuda, Masaya Kubota, Seiji Adachi, Hisashi Tsurumi, Yukihiko Hara, and Hisataka Moriwaki. "(-)-Epigallocatechin gallate inhibits growth and activation of the VEGF/VEGFR axis in human colorectal cancer cells". In: *Chemico-biological interactions* 185.3 (2010), pp. 247–252. DOI: 10.1016/j.cbi.2010.03.036.

[64] Joana Carina Lopes Freire. "Breast cancer and natural extracts: a theranostic approach supported by microPET images". Master Thesis. University of Coimbra, Dec. 14, 2021. URL: https://hdl.handle.net/10316/98158.

[65] Takehito Maruyama, Soichiro Murata, Ken Nakayama, Naoki Sano, Koichi Ogawa, Takeshi Nowatari, Takafumi Tamura, Reiji Nozaki, Kiyoshi Fukunaga, and Nobuhiro Ohkohchi. "(-)-Epigallocatechin-3-gallate suppresses liver metastasis of human colorectal cancer". In: *Oncology reports* 31.2 (2014), pp. 625–633. DOI: 10.3892/or.2013.2925.

[66] Kengo Ogawa, Takeshi Hara, Masahito Shimizu, Junji Nagano, Tomohiko Ohno, Masato Hoshi, Hiroyasu Ito, Hisashi Tsurumi, Kuniaki Saito, Mitsuru Seishima, et al. "(-)-Epigallocatechin gallate inhibits the expression of indoleamine 2, 3-dioxygenase in human colorectal cancer cells". In: *Oncology letters* 4.3 (2012), pp. 546–550. DOI: 10.3892/ol.2012.761.

[67] Min Huang, Jin-Jian Lu, and Jian Ding. "Natural products in cancer therapy: Past, present and future". In: *Natural products and bioprospecting* 11 (2021), pp. 5–13. DOI: 10.1007/s13659-020-00293-7.

[68] Yohei Shirakami and Masahito Shimizu. "Possible mechanisms of green tea and its constituents against cancer". In: *Molecules* 23.9 (2018), p. 2284. DOI: 10.3390/molecules23092284.

[69] Sarai Martinez-Pacheco and Lorraine O'Driscoll. "Pre-clinical in vitro models used in cancer research: Results of a worldwide survey". In: *Cancers* 13.23 (2021), p. 6033. DOI: 10.3390/cancers13236033.

[70] *WiDr CCL-218 ™ product sheet*. Dec. 4, 2022. URL: https://www.atcc.org/products/ccl-218.

[71] Alexandra Boussommier-Calleja. "In vitro models of cancer". In: *Bioengineering Innovative Solutions for Cancer*. Elsevier, 2020, pp. 273–325.

[72] P Noguchi, R Wallace, J Johnson, EM Earley, S O'brien, S Ferrone, MA Pellegrino, J Milstien, C Needy, W Browne, et al. "Characterization of WiDr: a human colon carcinoma cell line". In: *In vitro* 15 (1979), pp. 401–408. DOI: 10.1007/BF02618407.

[73] Fleming Mathew and Amandeep Goyal. "Ethanol". In: (2020).

[74] Meenakshi Arora. "Cell culture media: a review". In: *Mater methods* 3.175 (2013), p. 24.

[75] Nienke Vriezen, Bastiaan Romein, Karel Ch AM Luyben, and Johannes P van Dijken. "Effects of glutamine supply on growth and metabolism of mammalian cells in chemostat culture". In: *Biotechnology and bioengineering* 54.3 (1997), pp. 272–286. DOI: 10.1002/(SICI)1097-0290(19970505)54:3<272::AID-BIT8>3.0.CO;2-C.

[76] *Eagle's Minimum Essential Medium (EMEM) 30-2003 ™ product sheet*. May 13, 2023. URL: https://www.atcc.org/products/30-2003.

[77] Allison Hubel. *Preservation of cells: a practical manual*. John Wiley & Sons, 2018.

[78] Daniel Kaiser, Natalie Maureen Otto, Oliver McCallion, Henrike Hoffmann, Ghazaleh Zarrinrad, Maik Stein, Carola Beier, Isabell Matz, Marleen Herschel, Joanna Hester, et al. "Freezing medium containing 5% DMSO enhances the cell viability and recovery rate after cryopreservation of regulatory T cell products ex vivo and in vivo". In: *Frontiers in Cell and Developmental Biology* 9 (2021), p. 750286. DOI: 10.3389/fcell.2021.750286.

[79] John R Masters and Glyn N Stacey. "Changing medium and passaging cell lines". In: *Nature protocols* 2.9 (2007), pp. 2276–2284. DOI: 10.1038/nprot.2007.319.

[80] Ting-Yu Lai, Jerry Cao, Pu Ou-Yang, Ching-Yi Tsai, Chih-Wen Lin, Chien-Chia Chen, Meng-Kun Tsai, and Chih-Yuan Lee. "Different methods of detaching adherent cells and their effects on the cell surface expression of Fas receptor and Fas ligand". In: *Scientific reports* 12.1 (2022), p. 5713. DOI: 10.1038/s41598-022-09605-y.

[81] Thermo Fisher Scientific. *TrypLE Select Enzyme: a temperature-stable replacement for animal trypsin in cell dissociation applications*. 2020. URL: https://www.thermofisher.com/it/en/home/life-science/cell-culture/mammalian-cell-culture/reagents/tryple-reagents.html.

[82] Jessica J Alm, Hong Qian, and Katarina Le Blanc. "Clinical grade production of mesenchymal stromal cells". In: *Tissue Engineering*. Elsevier, 2014, pp. 427–469. DOI: 10.1016/B978-0-12-420145-3.00013-4.

[83] Logos Biosystems. *TrypLE Select Enzyme: a temperature-stable replacement for animal trypsin in cell dissociation applications*. 2020. URL: How%20to%20Count%20Cells%20-%20An%20Overview%20of%20Cell%20Counting%20Methods.

[84] Minghao Zhang, Lingui Gu, Peihua Zheng, Zhixin Chen, Xinqi Dou, Qizhong Qin, and Xiaozhong Cai. "Improvement of cell counting method for Neubauer counting chamber". In: *Journal of clinical laboratory analysis* 34.1 (2020), e23024. DOI: 10.1002/jcla.23024.

[85] Marienfeld Superior. *Counting chambers*. 2024. URL: https://www.marienfeld-superior.com/counting-chambers-2817.html.

[86] Jayme Garcia Arnal Barbedo. "Automatic Object Counting In Neubauer Chambers". In: *XXXI Brazilian telecommunication symposium*. Ed. by Jayme Garcia Arnal Barbedo. 2013.

[87] Warren Strober. "Trypan blue exclusion test of cell viability". In: *Current protocols in immunology* 111.1 (2015), A3–B. DOI: 10.1002/0471142735.ima03bs21.

[88] Maria Carolina da Costa Roseiro Janeiro. "Green tea extract in breast cancer - from cromatography analysis to the in models in vitro, in vivo and PET imaging". Master Thesis. University of Coimbra, Feb. 28, 2023. URL: https://hdl.handle.net/10316/107839.

[89] Michael J Lopez and Carrie A Hall. "Physiology, osmosis". In: (2020).

[90] Glória de Fátima da Silva Figueiredo. "Effect of a green tea extract in breast cancer: study in vitro and in animal model". Master Thesis. Aveiro University, Dec. 2, 2022. URL: http://hdl.handle.net/10773/38516.

[91] Henrique Andrade Proenca da Cunha. "Green tea's epigallocatechin-3-gallate (EGCG) - A natural agent in the fight against colorectal cancer". Master Thesis. University of Coimbra, May 30, 2017. URL: https://hdl.handle.net/10316/82074.

[92] Daniel B Longley, D Paul Harkin, and Patrick G Johnston. "5-fluorouracil: mechanisms of action and clinical strategies". In: *Nature reviews cancer* 3.5 (2003), pp. 330–338. DOI: 10.1038/nrc1074.

[93] Chinmayee Sethy and Chanakya Nath Kundu. "5-Fluorouracil (5-FU) resistance and the new strategy to enhance the sensitivity against cancer: Implication of DNA repair inhibition". In: *Biomedicine & Pharmacotherapy* 137 (2021), p. 111285. DOI: 10.1016/j.biopha.2021.111285.

[94] Sona Vodenkova, Tomas Buchler, Klara Cervena, Veronika Veskrnova, Pavel Vodicka, and Veronika Vymetalkova. "5-fluorouracil and other fluoropyrimidines in colorectal cancer: Past, present and future". In: *Pharmacology & therapeutics* 206 (2020), p. 107447. DOI: 10.1016/j.pharmthera.2019.107447.

[95] Edward Chu and Carmen J Allegra. "The role of thymidylate synthase in cellular regulation". In: *Advances in Enzyme Regulation* 36 (1996), pp. 143–163. DOI: 10.1002/bies.950180306.

[96] Daniel Sargent, Alberto Sobrero, Axel Grothey, Michael J O'Connell, Marc Buyse, Thierry Andre, Yan Zheng, Erin Green, Roberto Labianca, Chris O'Callaghan, et al. "Evidence for cure by adjuvant therapy in colon cancer: observations based on individual patient data from 20,898 patients on 18 randomized trials". In: *Journal of Clinical Oncology* 27.6 (2009), p. 872. DOI: 10.1200/JCO.2008.19.5362.

[97] CJH Gerrits, MJA De Jonge, JHM Schellens, G Stoter, and J Verweij. "Topoisomerase I inhibitors: the relevance of prolonged exposure for present clinical development". In: *British journal of cancer* 76.7 (1997), pp. 952–962. DOI: 10.1038/bjc.1997.491.

[98] Anish Thomas and Yves Pommier. "Targeting topoisomerase I in the era of precision medicine". In: *Clinical Cancer Research* 25.22 (2019), pp. 6581–6589. DOI: 10.1158/1078-0432.CCR-19-1089.

[99] Tauqeer Hussain Mallhi, Muhammad Hammad Butt, Abrar Ahmad, Shahzadi Misbah, Muhammad Salman, Amjad Khan, Ahsan Aftab Raja, and Yusra Habib Khan. "Drug-metabolizing enzymes and fate of prodrugs: From function to regulation". In: *Biochemistry of Drug Metabolizing Enzymes*. Elsevier, 2022, pp. 125–139. DOI: 10.1016/B978-0-323-95120-3.00005-1.

[100] Diane T Takahashi, Danièle Gadelle, Keli Agama, Evgeny Kiselev, Hongliang Zhang, Emilie Yab, Stephanie Petrella, Patrick Forterre, Yves Pommier, and Claudine Mayer. "Topoisomerase I (TOP1) dynamics: conformational transition from open to closed states". In: *Nature communications* 13.1 (2022), p. 59. DOI: 10.1038/s41467-021-27686-7.

[101] Yun Chai, Jing-Li Liu, Shuo Zhang, Na Li, Ding-Qiao Xu, Rui-Jia Fu, and Yu-Ping Tang. "The effective combination therapies with irinotecan for colorectal cancer". In: *Frontiers in Pharmacology* 15 (2024), p. 1356708. DOI: 10.3389/fphar.2024.1356708.

[102] Mateusz Kciuk, Beata Marciniak, and Renata Kontek. "Irinotecan—still an important player in cancer chemotherapy: a comprehensive overview". In: *International journal of molecular sciences* 21.14 (2020), p. 4919. DOI: 10.3390/ijms21144919.

[103] Agenzia Italiana del Farmaco (AIFA). *Foglio Illustrativo: Irinotecan Accord 20 mg/ml concentrato per soluzione per infusione*. 2019. URL: https://farmaci.agenziafarmaco.gov.it/bancadatifarmaci/farmaco?farmaco=044241.

[104] MedChemExpress®. *Cyclophosphamide*. 2024. URL: https://www.medchemexpress.com/Cyclophosphamide.html.

[105] MedChemExpress®. *Phosphoramide mustard*. 2024. URL: https://www.medchemexpress.com/phosphoramide-mustard.html.

[106] Eslam Dabbish, Stefano Scoditti, Mohammed NI Shehata, Ida Ritacco, Mahmoud AA Ibrahim, Tamer Shoeib, and Emilia Sicilia. "Insights on cyclophosphamide metabolism and anticancer mechanism of action: A computational study". In: *Journal of Computational Chemistry* (2023). DOI: 10.1002/jcc.27280.

[107] Milly E De Jonge, Alwin DR Huitema, Sjoerd Rodenhuis, and Jos H Beijnen. "Clinical pharmacokinetics of cyclophosphamide". In: *Clinical pharmacokinetics* 44.11 (2005), pp. 1135–1164. DOI: 10.2165/00003088-200544110-00003.

[108] Alwin DR Huitema, Matthijs M Tibben, Thomas Kerbusch, J Jantien Kettenes-Van Den Bosch, Sjoerd Rodenhuis, and Jos H Beijnen. "Simple and selective determination of the cyclophosphamide metabolite phosphoramide mustard in human plasma using high-performance liquid chromatography". In: *Journal of Chromatography B: Biomedical Sciences and Applications* 745.2 (2000), pp. 345–355. DOI: 10.1016/s0378-4347(00)00295-4.

[109] Mari H Ogino and Prasanna Tadi. "Cyclophosphamide". In: (2020).

[110] Mariana Domingues Marques. "Colon cancer and green tea extract - in vitro and in vivo models to evaluate their efficacy using imaging techniques". Master Thesis. University of Coimbra, Sept. 30, 2022. URL: https://hdl.handle.net/10316/103166.

[111] Christie Berenice Alves da Graça Monteiro. "EGCG of Green Tea - a natural agent against breast cancer". Master Thesis. University of Coimbra, Sept. 24, 2018. URL: https://hdl.handle.net/10316/86237.

[112] Jane A Plumb. "Cell sensitivity assays: the MTT assay". In: *Cancer cell culture: methods and protocols* (2004), pp. 165–169. DOI: 10.1385/1-59259-406-9:165.

[113] Philip Wachsmann and Alf Lamprecht. "Polymeric nanoparticles for the selective therapy of inflammatory bowel disease". In: *Methods in Enzymology* 508 (2012), pp. 377–397. DOI: 10.1016/B978-0-12-391860-4.00019-7.

[114] Michael V Berridge, Patries M Herst, and An S Tan. "Tetrazolium dyes as tools in cell biology: new insights into their cellular reduction". In: *Biotechnology annual review* 11 (2005), pp. 127–152. DOI: 10.1016/S1387-2656(05)11004-7.

[115] Mahshid Ghasemi, Tyron Turnbull, Sonia Sebastian, and Ivan Kempson. "The MTT assay: utility, limitations, pitfalls, and interpretation in bulk and single-cell analysis". In: *International journal of molecular sciences* 22.23 (2021), p. 12827. DOI: 10.3390/ijms222312827.

[116] Johan Van Meerloo, Gertjan JL Kaspers, and Jacqueline Cloos. "Cell sensitivity assays: the MTT assay". In: *Cancer cell culture: methods and protocols* (2011), pp. 237–245. DOI: 10.1007/978-1-61779-080-5_20.

[117] Carl W Mize, Kenneth J Koehler, and Michael E Compton. "Statistical considerations for in vitro research: II—Data to presentation". In: *In Vitro Cellular & Developmental Biology-Plant* 35 (1999), pp. 122–126. DOI: 10.1007/s11627-999-0021-1.

[118] Francis Sahngun Nahm. "Nonparametric statistical tests for the continuous data: the basic concept and the practical use". In: *Korean journal of anesthesiology* 69.1 (2016), p. 8. DOI: 10.4097/kjae.2016.69.1.8.

[119] Elliot McClenaghan. *The Kruskal–Wallis Test*. Ed. by Technology Network - Informatics. Feb. 8, 2023. URL: https://www.technologynetworks.com/informatics/articles/the-kruskal-wallis-test-370025.

[120] Alan S Bellack and Michel Hersen. "Comprehensive clinical psychology". In: (1998).

[121] P Larsson, H Engqvist, J Biermann, EW Ronnerman, E Forssell-Aronsson, A Kovacs, P Karlsson, K Helou, and TZ Parris. *Optimization of cell viability assays to improve replicability and reproducibility of cancer drug sensitivity screens. Sci Rep 10 (1): 5798.* 2020. DOI: 10.1038/s41598-020-62848-5.

[122] Altogen Labs. *Pharmacology and Toxicology Testing: IC50 for Tumor Cell Lines*. Ed. by Copyright © 2024 Altogen Labs. 2024. URL: https://altogenlabs.com/preclinical-research-services/pharmacology-and-toxicology-testing-ic50-for-tumor-cell-lines/.

[123] HO Douglass Jr, PT Lavin, Judith Woll, James F Conroy, and Paul Carbone. "Chemotherapy of advanced measurable colon and rectal carcinoma with oral 5-fluorouracil, alone or in combination with cyclophosphamide or 6-thioguanine, with intravenous 5-fluorouracil or beta-2'-deoxythioguanosine or with oral 3 (4-methyl-cyclohexyl)-1 (2-chlorethyl)-1-nitrosourea. A phase II-III study of the eastern cooperative oncology group (EST 4273)". In: *Cancer* 42.6 (1978), pp. 2538–2545. DOI: 10.1002/1097-0142(197812)42:6<2538::aid-cncr2820420606>3.0.co;2-a.

[124] Jarett Casale and Preeti Patel. "Fluorouracil". In: *StatPearls [Internet]*. StatPearls Publishing, 2022.

[125] Maurizio Meregalli, Giancarlo Martignoni, Luciano Frontini, Sabrina Zonato, Gianfranco Pavia, and Giovanni Beretta. "Increasing doses of 5-fluorouracil and high-dose folinic acid in the treatment of metastatic colorectal cancer". In: *Tumori Journal* 84.6 (1998), pp. 662–665. DOI: 10.1177/030089169808400609.

[126] Charles Fuchs, Edith P Mitchell, and Paulo M Hoff. "Irinotecan in the treatment of colorectal cancer". In: *Cancer treatment reviews* 32.7 (2006), pp. 491–503. DOI: 10.1016/j.ctrv.2006.07.001.

[127] Megan Li, Eric L Seiser, R Michael Baldwin, Jacqueline Ramirez, Mark J Ratain, Federico Innocenti, and Deanna L Kroetz. "ABC transporter polymorphisms are associated with irinotecan pharmacokinetics and neutropenia". In: *The pharmacogenomics journal* 18.1 (2018), pp. 35–42. DOI: 10.1038/tpj.2016.75.

[128] Shamin Azwar, Heng Fong Seow, Maha Abdullah, Mohd Faisal Jabar, and Norhafizah Mohtarrudin. "Recent updates on mechanisms of resistance to 5-fluorouracil and reversal strategies in colon cancer treatment". In: *Biology* 10.9 (2021), p. 854. DOI: 10.3390/biology10090854.

[129] D Cunningham, S Falk, and D Jackson. "Clinical and economic benefits of irinotecan in combination with 5-fluorouracil and folinic acid as first line treatment of metastatic colorectal cancer". In: *British journal of cancer* 86.11 (2002), pp. 1677–1683. DOI: 10.1038/sj.bjc.6600204.

[130] Dong-Joo Cheon and Sandra Orsulic. "Mouse models of cancer". In: *Annual Review of Pathology: Mechanisms of Disease* 6 (2011), pp. 95–119. DOI: 10.1146/annurev.pathol.3.121806.154244.

[131] Jonathan Dornell. "In vivo vs in vitro: Definition, pros and cons". In: *Drug Discovery from Technology Networks. www. technologynetworks. com/drug-discovery/articles/in-vivo-vs-in-vitro-definition-pros-and-cons-350415* (2022).

[132] Len A Pennacchio. "Insights from human/mouse genome comparisons". In: *Mammalian genome* 14 (2003), pp. 429–436. DOI: 10.1007/s00335-002-4001-1.

[133] European Bioinformatics Institute. "Initial sequencing and comparative analysis of the mouse genome". In: *Nature* 420.6915 (2002), pp. 520–562. DOI: 10.1038/nature01262.

[134] *EU regulations on animal research*. 2023. URL: https://www.eara.eu/animal-research-law?lang=it.

[135] Stanley Maloy and Kelly Hughes. *Brenner's encyclopedia of genetics*. Academic Press, 2013, pp. 141–143.

[136] Kailey Remien and Arif Jan. "Anatomy, head and neck, thymus". In: (2019).

[137] Lars Mecklenburg, Birte Tychsen, and Ralf Paus. "Learning from nudity: lessons from the nude phenotype". In: *Experimental dermatology* 14.11 (2005), pp. 797–810. DOI: 10.1111/j.1600-0625.2005.00362.x.

[138] Wanglong Qiu and Gloria H Su. "Development of orthotopic pancreatic tumor mouse models". In: *Pancreatic Cancer: Methods and Protocols* (2013), pp. 215–223. DOI: 10.1007/978-1-62703-287-2_11.

[139] Ivan Szadvári, O Krizanova, and Petr Babula. "Athymic nude mice as an experimental model for cancer treatment." In: *Physiological research* 65 (2016). DOI: 10.33549/physiolres.933526.

[140] Erica Yada, Satoshi Wada, Shintaro Yoshida, and Tetsuro Sasada. *Use of patient-derived xenograft mouse models in cancer research and treatment*. 2017. DOI: 10.4155/fsoa-2017-0136.

[141] Jorgen Fogh, Thomas Orfeo, John Tiso, Francis E Sharkey, Jens M Fogh, and Walter P Daniels. "Twenty-three new human tumor lines established in nude mice". In: *Pathobiology* 48.3 (1980), pp. 229–239. DOI: 10.1159/000162990.

[142] Svenja Nolting, Alessio Giubellino, Yasin Tayem, Karen Young, Michael Lauseker, Petra Bullova, Jan Schovanek, Miriam Anver, Stephanie Fliedner, Marta Korbonits, et al. "Combination of 13-Cis retinoic acid and lovastatin: marked antitumor potential in vivo in a pheochromocytoma allograft model in female athymic nude mice". In: *Endocrinology* 155.7 (2014), pp. 2377–2390. DOI: 10.1210/en.2014-1027.

[143] P Workman, EO Aboagye, F Balkwill, A Balmain, Gail Bruder, DJ Chaplin, JA Double, J Everitt, DAH Farningham, MJ Glennie, et al. "Guidelines for the welfare and use of animals in cancer research". In: *British journal of cancer* 102.11 (2010), pp. 1555–1577. DOI: 10.1038/sj.bjc.6605642.

[144] Wanshui Yang, Yanan Ma, Stephanie Smith-Warner, Mingyang Song, Kana Wu, Molin Wang, Andrew T Chan, Shuji Ogino, Charles S Fuchs, Vitaliy Poylin, et al. "Calcium intake and survival after colorectal cancer diagnosis". In: *Clinical Cancer Research* 25.6 (2019), pp. 1980–1988. DOI: 10.1158/1078-0432.CCR-18-2965.

[145] Evertine Wesselink, Renate M Winkels, Harm Van Baar, Anne JMR Geijsen, Moniek Van Zutphen, Henk K Van Halteren, Bibi ME Hansson, Sandra A Radema, Johannes HW De Wilt, Ellen Kampman, et al. "Dietary intake of magnesium or calcium and chemotherapy-induced peripheral neuropathy in colorectal cancer patients". In: *Nutrients* 10.4 (2018), p. 398. DOI: 10.3390/nu10040398.

[146] Sylvia Christakos, Puneet Dhawan, Angela Porta, Leila J Mady, and Tanya Seth. "Vitamin D and intestinal calcium absorption". In: *Molecular and cellular endocrinology* 347.1-2 (2011), pp. 25–29. DOI: 10.1016/j.mce.2011.05.038.

[147] *Product information - Irinotecan medac 20 mg/mL, concentrate for solution for infusion.* Oct. 2022. URL: https://www.medac.eu/fileadmin/user_upload/medac-eu/SPCs/common_SPCs/Irinotecan-spc-common.pdf.

[148] Haruna Hatahira, Kazuhiro Iguchi, Sayaka Sasaoka, Yumi Motooka, Shiori Hasegawa, Misa Naganuma, Akiho Fukuda, Tomofumi Ohmori, Tatsuhiko Yoshida, Kaoru Mogushi, et al. "Body surface area formulas for the calculation of the chemotherapy dosage". In: *Gan to Kagaku ryoho. Cancer & Chemotherapy* 44.11 (2017), pp. 1011–1015.

[149] Michael C Cheung, Paul B Spalding, Juan C Gutierrez, Wayne Balkan, Nicholas Namias, Leonidas G Koniaris, and Teresa A Zimmers. "Body surface area prediction in normal, hypermuscular, and obese mice". In: *Journal of Surgical Research* 153.2 (2009), pp. 326–331. DOI: 10.1016/j.jss.2008.05.002.

[150] Abdullah Al Shoyaib, Sabrina Rahman Archie, and Vardan T Karamyan. "Intraperitoneal route of drug administration: should it be used in experimental animal studies?" In: *Pharmaceutical research* 37.1 (2020), p. 12. DOI: 10.1007/s11095-019-2745-x.

[151] Francisca Sousa Pereira. “Green Tea EGCG - a natural agent against colorectal and breast cancer”. Master Thesis. University of Coimbra, Sept. 26, 2017. URL: https://hdl.handle.net/10316/83335.

[152] National Institute of Biomedical Imaging and Bioengineering. *Nuclear Medicine: Fact Sheet*. Ed. by Department of Health and Human Services - USA.gov. Apr. 2022. URL: https://www.nibib.nih.gov/science-education/science-topics/nuclear-medicine.

[153] Timothy G Turkington. “Introduction to PET instrumentation”. In: *Journal of nuclear medicine technology* 29.1 (2001), pp. 4–11.

[154] Gary D Hutchins, Michael A Miller, Victor C Soon, and Timothy Receveur. “Small animal PET imaging”. In: *ILAR journal* 49.1 (2008), pp. 54–65. DOI: 10.1093/ilar.49.1.54.

[155] Veerle Kersemans, Bart Cornelissen, Philip D Allen, John S Beech, and Sean C Smart. “Subcutaneous tumor volume measurement in the awake, manually restrained mouse using MRI”. In: *Journal of Magnetic Resonance Imaging* 37.6 (2013), pp. 1499–1504. DOI: 10.1002/jmri.23829.

[156] Debing Shi, Guoxiang Cai, Junjie Peng, Dawei Li, Xinxiang Li, Ye Xu, and Sanjun Cai. “The preoperative SUVmax for 18 F-FDG uptake predicts survival in patients with colorectal cancer”. In: *BMC cancer* 15 (2015), pp. 1–8. DOI: 10.1186/s12885-015-1991-5.

[157] Wellington K Hsu, Mandeep S Virk, Brian T Feeley, David B Stout, Arion F Chatzioannou, and Jay R Lieberman. “Characterization of osteolytic, osteoblastic, and mixed lesions in a prostate cancer mouse model using 18F-FDG and 18F-fluoride PET/CT”. In: *Journal of Nuclear Medicine* 49.3 (2008), pp. 414–421. DOI: 10.2967/jnumed.107.045666.

[158] Christophe M Deroose, Abhijit De, Andreas M Loening, Patrick L Chow, Pritha Ray, Arion F Chatziioannou, and Sanjiv S Gambhir. “Multimodality imaging of tumor xenografts and metastases in mice with combined small-animal PET, small-animal CT, and bioluminescence imaging”. In: *Journal of Nuclear Medicine* 48.2 (2007), pp. 295–303.

[159] Martin Uffmann and Cornelia Schaefer-Prokop. “Digital radiography: the balance between image quality and required radiation dose”. In: *European journal of radiology* 72.2 (2009), pp. 202–208. DOI: 10.1016/j.ejrad.2009.05.060.

[160] Pyong Eun Park, Jung Min Park, Joo Eun Kang, Jae Hun Cho, Suk Ju Cho, Jae Hun Kim, Woo Seog Sim, and Yong Chul Kim. “Radiation safety and education in the applicants of the final test for the expert of pain medicine”. In: *The Korean journal of pain* 25.1 (2012), p. 16. DOI: 10.3344/kjp.2012.25.1.16.

[161] Centers for Disease Control and Prevention. *ALARA – As Low As Reasonably Achievable*. May 17, 2022. URL: https://www.cdc.gov/nceh/radiation/alara.html.

[162] Jae Hun Kim. “Three principles for radiation safety: time, distance, and shielding”. In: *The Korean journal of pain* 31.3 (2018), p. 145. DOI: 10.3344/kjp.2018.31.3.145.

[163] Kenji Kawada, Masayoshi Iwamoto, and Yoshiharu Sakai. “Mechanisms underlying 18F-fluorodeoxyglucose accumulation in colorectal cancer”. In: *World journal of radiology* 8.11 (2016), p. 880. DOI: 10.4329/wjr.v8.i11.880.

[164] Erica A Melkonian and Mark P Schury. “Biochemistry, anaerobic glycolysis”. In: (2019).

[165] James R Ballinger. “18F-Fluorodeoxyglucose (FDG)”. In: *PET Radiopharmaceuticals: Chemical, Biological, and Clinical Data*. Springer, 2022, pp. 2–3.

[166] Ashwin Singh Parihar, Farrokh Dehdashti, and Richard L Wahl. "FDG PET/CT–based Response Assessment in Malignancies". In: *Radiographics* 43.4 (2023), e220122. DOI: 10.1148/rg.220122.

[167] Didier Le Bars. "Fluorine-18 and medical imaging: Radiopharmaceuticals for positron emission tomography". In: *Journal of fluorine chemistry* 127.11 (2006), pp. 1488–1493. DOI: 10.1016/j.jfluchem.2006.09.015.

[168] Bionity.com. *Dose calibrator*. 2024. URL: https://www.bionity.com/en/encyclopedia/Dose_calibrator.html.

[169] FM Ribeiro, PMM Correia, AC Santos, and JFCA Veloso. "A guideline proposal for mice preparation and care in 18F-FDG PET imaging". In: *EJNMMI research* 12.1 (2022), p. 49. DOI: 10.1186/s13550-022-00921-y.

[170] Barbara J Fueger, Johannes Czernin, Isabel Hildebrandt, Chris Tran, Benjamin S Halpern, David Stout, Michael E Phelps, and Wolfgang A Weber. "Impact of animal handling on the results of 18F-FDG PET studies in mice". In: *Journal of Nuclear Medicine* 47.6 (2006), pp. 999–1006.

[171] SABRY M ABDEL, ABDEL EL MOTAL, and GEOFFREY WG SHARP. "Inhibition of glucose-induced insulin release by xylazine". In: *Endocrinology* 116.6 (1985), pp. 2337–2340. DOI: 10.1210/endo-116-6-2337.

[172] CJ Green, J Knight, S Precious, and S Simpkin. "Ketamine alone and combined with diazepam or xylazine in laboratory animals: a 10 year experience". In: *Laboratory animals* 15.2 (1981), pp. 163–170. DOI: 10.1258/002367781780959107.

[173] Sara Gargiulo, Adelaide Greco, Matteo Gramanzini, Silvia Esposito, Andrea Affuso, Arturo Brunetti, and Giancarlo Vesce. "Mice anesthesia, analgesia, and care, Part I: anesthetic considerations in preclinical research". In: *ILAR journal* 53.1 (2012), E55–E69. DOI: 10.1093/ilar.53.1.55.

[174] Benjamin E Jewett and Bicky Thapa. "Physiology, NMDA receptor". In: *StatPearls [Internet]*. StatPearls Publishing, 2022.

[175] Kyung-Han Lee, Bong-Ho Ko, Jin-Young Paik, Kyung-Ho Jung, Yearn Seong Choe, Yong Choi, and Byung-Tae Kim. "Effects of anesthetic agents and fasting duration on 18F-FDG biodistribution and insulin levels in tumor-bearing mice". In: *Journal of Nuclear Medicine* 46.9 (2005), pp. 1531–1536.

[176] Simon R Cherry, Terry Jones, Joel S Karp, Jinyi Qi, William W Moses, and Ramsey D Badawi. "Total-body PET: maximizing sensitivity to create new opportunities for clinical research and patient care". In: *Journal of Nuclear Medicine* 59.1 (2018), pp. 3–12. DOI: 10.2967/jnumed.116.184028.

[177] Ramsey D Badawi, Hongcheng Shi, Pengcheng Hu, Shuguang Chen, Tianyi Xu, Patricia M Price, Yu Ding, Benjamin A Spencer, Lorenzo Nardo, Weiping Liu, et al. "First human imaging studies with the EXPLORER total-body PET scanner". In: *Journal of Nuclear Medicine* 60.3 (2019), pp. 299–303. DOI: 10.2967/jnumed.119.226498.

[178] Stefaan Vandenberghe, Pawel Moskal, and Joel S Karp. "State of the art in total body PET". In: *EJNMMI physics* 7 (2020), pp. 1–33. DOI: 10.1186/s40658-020-00290-2.

[179] Junwei Du and Terry Jones. "Technical opportunities and challenges in developing total-body PET scanners for mice and rats". In: *EJNMMI physics* 10.1 (2023), p. 2. DOI: 10.1186/s40658-022-00523-6.

[180] Charles L Melcher. "Scintillation crystals for PET". In: *Journal of Nuclear Medicine* 41.6 (2000), pp. 1051–1055.

[181] Radiology Key - Fastest Radiology Insight Engin. *PET Physics and Instrumentation*. 2024. URL: https://radiologykey.com/pet-physics-and-instrumentation/#CR36.

[182] Anders Brahme. *Comprehensive biomedical physics*. Newnes, 2014.

[183] Rutao Yao, Roger Lecomte, and Elpida S Crawford. "Small-animal PET: what is it, and why do we need it?" In: *Journal of nuclear medicine technology* 40.3 (2012), pp. 157–165. DOI: 10.2967/jnmt.111.098632.

[184] Valentina Arosio, Massimo Caccia, IF Castro, PMM Correia, Cristina Mattone, LM Moutinho, Romualdo Santoro, ALM Silva, and JFCA Veloso. "easyPET: a novel concept for an affordable tomographic system". In: *Nuclear Instruments and Methods in Physics Research Section A: Accelerators, Spectrometers, Detectors and Associated Equipment* 845 (2017), pp. 644–647. DOI: 10.1109/NSSMIC.2016.8069360.

[185] Emilie Roncali and Simon R Cherry. "Application of silicon photomultipliers to positron emission tomography". In: *Annals of biomedical engineering* 39 (2011), pp. 1358–1377. DOI: 10.1007/s10439-011-0266-9.

[186] Andrew L Goertzen, Qinan Bao, Mélanie Bergeron, Eric Blankemeyer, Stephan Blinder, Mario Cañadas, Arion F Chatziioannou, Katherine Dinelle, Esmat Elhami, Hans-Sonke Jans, et al. "NEMA NU 4-2008 comparison of preclinical PET imaging systems". In: *Journal of nuclear medicine* 53.8 (2012), pp. 1300–1309. DOI: 10.2967/jnumed.111.099382.

[187] Camilla Nicolucci, Mariana Lapo Pais, AC Santos, Fabiana M Ribeiro, Pedro MCC Encarnação, Ana LM Silva, IF Castro, Pedro MM Correia, João FCA Veloso, Julie Reis, et al. "Single low dose of cocaine–structural brain injury without metabolic and behavioral changes". In: *Frontiers in Neuroscience* 14 (2021), p. 589897. DOI: 10.3389/fnins.2020.589897.

[188] Regina G Oliveira, Pedro MM Correia, Ana LM Silva, Pedro MCC Encarnação, Fabiana M Ribeiro, Ismael F Castro, and João FCA Veloso. "Development of a new integrated system for vital sign monitoring in small animals". In: *Sensors* 22.11 (2022), p. 4264. DOI: 10.3390/s22114264.

[189] Robert M Lewitt and Samuel Matej. "Overview of methods for image reconstruction from projections in emission computed tomography". In: *Proceedings of the IEEE* 91.10 (2003), pp. 1588–1611. DOI: 10.1109/JPROC.2003.817882.

[190] Shan Tong, Adam M Alessio, and Paul E Kinahan. "Image reconstruction for PET/CT scanners: past achievements and future challenges". In: *Imaging in medicine* 2.5 (2010), p. 529. DOI: 10.2217/iim.10.49.

[191] Simon R Cherry, Magnus Dahlbom, Simon R Cherry, and Magnus Dahlbom. *PET: physics, instrumentation, and scanners*. Springer, 2006.

[192] Stefaan Vandenberghe, Steven Staelens, Rik Van de Walle, Rudi Dierckx, and Ignace Lemahieu. "Compression and reconstruction of sorted PET listmode data". In: *Nuclear medicine communications* 26.9 (2005), pp. 819–825. DOI: 10.1097/01.mnm.0000175789.50294.56.

[193] Lawrence A Shepp and Yehuda Vardi. "Maximum likelihood reconstruction for emission tomography". In: *IEEE transactions on medical imaging* 1.2 (1982), pp. 113–122. DOI: 10.1109/TMI.1982.4307558.

[194] Ana Iriarte, Roberto Marabini, Samuel Matej, Carlos Oscar Sánchez Sorzano, and Robert M Lewitt. "System models for PET statistical iterative reconstruction: A review". In: *Computerized Medical Imaging and Graphics* 48 (2016), pp. 30–48.

[195] Luca Caucci, William CJ Hunter, Lars R Furenlid, and Harrison H Barrett. "List-mode MLEM image reconstruction from 3D ML position estimates". In: *IEEE Nuclear Science Symposuim & Medical Imaging Conference*. IEEE. 2010, pp. 2643–2647. DOI: 10.1109/NSSMIC.2010.5874269.

[196] Bruce Caplan, John DeLuca, and Jeffrey S Kreutzer. *Encyclopedia of clinical neuropsychology*. Springer, 2010.

[197] Angel Alberich-Bayarri, Ana Jiménez-Pastor, and Irene Mayorga-Ruiz. "Imaging Biomarkers and Their Meaning for Molecular Imaging". In: *Artificial Intelligence/Machine Learning in Nuclear Medicine and Hybrid Imaging*. Springer, 2022, pp. 83–86. DOI: 10.1007/978-3-031-00119-2_6.

[198] Noémie Moreau, Caroline Rousseau, Constance Fourcade, Gianmarco Santini, Aislinn Brennan, Ludovic Ferrer, Marie Lacombe, Camille Guillerminet, Mathilde Colombié, Pascal Jézéquel, et al. "Automatic segmentation of metastatic breast cancer lesions on 18F-FDG PET/CT longitudinal acquisitions for treatment response assessment". In: *Cancers* 14.1 (2021), p. 101. DOI: 10.3390/cancers14010101.

[199] Joseph A Thie. "Understanding the standardized uptake value, its methods, and implications for usage". In: *Journal of Nuclear Medicine* 45.9 (2004), pp. 1431–1434.

[200] Gopal B Saha and B Gopal. *Basics of PET imaging: physics, chemistry, and regulations*. Springer, 2005.

[201] Eric Laffon, Henri de Clermont, and Roger Marthan. "A method of adjusting SUV for injection-acquisition time differences in 18 F-FDG PET Imaging". In: *European radiology* 21 (2011), pp. 2417–2424. DOI: 10.1007/s00330-011-2204-5.

[202] Sandip Basu, Habib Zaidi, Soren Holm, and Abass Alavi. "Quantitative techniques in PET-CT imaging". In: *Current Medical Imaging* 7.3 (2011), pp. 216–233. DOI: 10.2174/157340511796411186.

[203] Ingfrid S Haldorsen, Mihaela Popa, Tina Fonnes, Njål Brekke, Reidun Kopperud, Nicole C Visser, Cecilie B Rygh, Tina Pavlin, Helga B Salvesen, Emmet McCormack, et al. "Multimodal imaging of orthotopic mouse model of endometrial carcinoma". In: *PLoS One* 10.8 (2015), e0135220. DOI: 10.1371/journal.pone.0135220.

[204] S Fardin, S Gholami, TJ Werner, AH Rook, and A Alavi. "Imaging evaluation of cutaneous lymphoma using functional and structural imaging". In: *Imaging in Dermatology*. Elsevier, 2016, pp. 485–490.

[205] Gary A Ulaner. *Fundamentals of oncologic PET/CT*. Elsevier Health Sciences, 2018.

[206] David Stout, Stuart S Berr, Amy LeBlanc, Joseph D Kalen, Dustin Osborne, Julie Price, Wynne Schiffer, Claudia Kuntner, and Jonathan Wall. "Guidance for methods descriptions used in preclinical imaging papers". In: *Molecular imaging* 12.7 (2013), pp. 7290–2013.

[207] Christian Vanhove, Jens P Bankstahl, Stefanie D Krämer, Eric Visser, Nicola Belcari, and Stefaan Vandenberghe. "Accurate molecular imaging of small animals taking into account animal models, handling, anaesthesia, quality control and imaging system performance". In: *EJNMMI physics* 2 (2015), pp. 1–25. DOI: 10.1186/s40658-015-0135-y.

[208] Reda Hallab et al. "The Quality Assurance for the PET/CT in Nuclear Medicine-Evaluation of the Daily Quality Control of the Positron Emission Tomography". In: *Biomedical and Pharmacology Journal* 15.3 (2022), pp. 1589–1595. DOI: 10.13005/bpj/2497.

[209] Jamie Bartram and Gareth Rees. *Monitoring bathing waters: a practical guide to the design and implementation of assessments and monitoring programmes*. CRC Press, 1999.

[210] Wendy A McDougald and Julia G Mannheim. "Understanding the importance of quality control and quality assurance in preclinical PET/CT imaging". In: *EJNMMI physics* 9.1 (2022), p. 77. DOI: 10.1186/s40658-022-00503-w.

[211] *NU 4-2008 Performance measurements of Small Animal Positron Emission Tomographs*. 2008.

[212] Daniel Gillett, Daniel Marsden, Safia Ballout, Bala Attili, Nick Bird, Sarah Heard, Mark Gurnell, Iosif A Mendichovszky, and Luigi Aloj. "3D printing 18F radioactive phantoms for PET imaging". In: *EJNMMI physics* 8.1 (2021), p. 38. DOI: 10.1186/s40658-021-00383-6.

[213] Francis Bouchet, Lilli Geworski, Bernd O Knoop, Ludovic Ferrer, Alina Barriolo-Riedinger, Corinne Millardet, Marjolaine Fourcade, Antoine Martineau, Anne Belly-Poinsignon, Francis Djoumessi, et al. "Calibration test of PET scanners in a multi-centre clinical trial on breast cancer therapy monitoring using 18F-FLT". In: *PLoS One* 8.3 (2013), e58152. DOI: 10.1371/journal.pone.0058152.

[214] Jakob W Kist, Manfred van der Vlies, Otto S Hoekstra, Henri NJM Greuter, Bart de Keizer, Marcel PM Stokkel, Wouter V Vogel, Marc C Huisman, and Arthur van Lingen. "Calibration of PET/CT scanners for multicenter studies on differentiated thyroid cancer with 124 I". In: *EJNMMI research* 6 (2016), pp. 1–8. DOI: 10.1186/s13550-016-0191-x.

[215] Dustin R Osborne, Claudia Kuntner, Stuart Berr, and David Stout. "Guidance for efficient small animal imaging quality control". In: *Molecular imaging and biology* 19 (2017), pp. 485–498. DOI: 10.1016/j.compmedimag.2015.12.003.

[216] Rodrigo Modesto Gadelha Gontijo, Andréa Vidal Ferreira, Juliana Batista Silva, and Marcelo Henrique Mamede. "Image quality assessment using NEMA NU 4/2008 standards in small animal PET scanner". In: *Brazilian Journal of Radiation Sciences* 7.2A (Suppl.) (2019). DOI: 10.15392/bjrs.v7i2A.580.

[217] Colorectal Cancer Alliance. *Side effects of colorectal cancer treatment*. 2024. URL: https://colorectalcancer.org/treatment/types-treatment/side-effects.

[218] Zineb Aoullay, Meriem Slaoui, Rachid Razine, Abdelouahed Er-Raki, Bouchra Meddah, and Yahia Cherrah. "Therapeutic characteristics, chemotherapy-related toxicities and survivorship in colorectal cancer patients". In: *Ethiopian journal of health sciences* 30.1 (2020). DOI: 10.4314/ejhs.v30i1.9.

[219] Rodrigo Modesto Gadelha, Andréa Vidal Ferreira, Guilherme Albuquerque Cavalcante Souza, Juliana Batista Silva, and Marcelo Mamede. "Image quality evaluation for two different positron emitters in a preclinical PET scanner". In: *Brazilian Journal of Radiation Sciences* 8.3 (2020). DOI: 10.15392/bjrs.v8i3.1299.

[220] Maryam Shahrokni, Qingan Zhu, Jie Liu, Wolfram Tetzlaff, and Thomas R Oxland. "Design and biomechanical evaluation of a rodent spinal fixation device". In: *Spinal cord* 50.7 (2012), pp. 543–547. DOI: 10.1038/sc.2011.185.

[221] Jessica P Miller, Christopher Egbulefu, Julie L Prior, Mingzhou Zhou, and Samuel Achilefu. "Gradient-based algorithm for determining tumor volumes in small animals using planar fluorescence imaging platform". In: *Tomography* 2.1 (2016), pp. 17–25. DOI: 10.18383/j.tom.2016.00100.

[222] Hannu Huhdanpaa, Darryl H Hwang, Gregory G Gasparian, Michael T Booker, Yong Cen, Alexander Lerner, Orest B Boyko, John L Go, Paul E Kim, Anandh Rajamohan, et al. “Image coregistration: quantitative processing framework for the assessment of brain lesions”. In: *Journal of digital imaging* 27 (2014), pp. 369–379. DOI: 10.1007/s10278-013-9655-y.

Ringraziamenti

Quando leggo le tesi degli altri, dopo averle sfogliate con finto interesse e spesso non capendo niente di ciò che c'è scritto, mi fermo sempre alla pagina dei ringraziamenti, perché penso costituiscano le vere conclusioni, non tanto della tesi, ma di un'esperienza di vita che si chiude, e apre dopo di sé molte riflessioni.
Al termine di questo percorso, vorrei ringraziare il mio relatore, Mattia Veronese, che con professionalità e tenacia, ha saputo indirizzare il mio studio sin dall'inizio della magistrale.
Um 'muito obrigada' também à incansável professora Ana Cristina Santos, que foi sempre muito presente e disponível a qualquer hora do dia. Obrigada a Portugal, à plenitude e às dificuldades que estes seis meses me trouxeram e, acima de tudo, às pessoas que me acolheram e me fizeram sentir em casa.
Stare in Portogallo, a fare ricerca sul Cancro al Colon, è stato per me come passare la mano su una cicatrice: prima di partire, ho scelto il primo progetto che mi è capitato tra le mani visto che, da lontano, era difficile contattare i professori. Però, mi è capitato proprio un argomento che risuonava nella storia della mia famiglia: un polipo al colon che, in pochi anni, ci ha cambiato la vita.
Ricordo che, quando ho iniziato l'Università, avevo un desiderio di riscatto, di sapere cosa succede quando si ha un tumore, e di cercare di trovarci una soluzione: insieme ai professori del liceo che mi dicevano "Hai una mente scientifica", la mia scelta di Ingegneria Biomedica è stata anche guidata dal desiderio di riscatto di una Benedetta diciottenne. In questi anni di studio, però, grazie al confronto, ho potuto capire che, a volte, vogliamo dimostrarci forti andando a toccare quei pezzi del nostro vissuto che ci hanno provocato più dolore, proprio come passare una mano su una cicatrice. È la stessa cosa di pensare: "Sono a dieta, ma, per dimostrare che sono forte, entro in una pasticceria e non prendo nemmeno un dolcetto". Se però avessi vissuto questi anni e i sei mesi in Portogallo lasciandomi guidare da questo peso, non sarebbe stato un bel periodo. Quindi, sono contenta, perché ho capito che ciò che voglio che guidi le mie scelte, da Bioingegnere e da giovane che inizia a scrivere un nuovo capitolo della Vita: non il desiderio di una rivincita, ma il desiderio di trovare la mia strada e ciò che mi appassiona.
Ho avuto la grazia di incontrare professori appassionati, che mi hanno fatto apprezzare materie che mai avrei pensato e mi hanno fatto capire che il dono più grande che possiamo farci è scegliere ciò che ci piace e ci fa stare bene. Durante la ricerca per la tesi, ho visto che questo mestiere richiede tempo, pazienza, passione e motivazione (mia sorella ne sa qualcosa): stare in laboratorio, è un po' come cimentarsi nel cucinare una ricetta complicata. Servono ingredienti selezionati, una bilancia per pesare le quantità precise, gli strumenti giusti.
Non so se in futuro sarò in una cucina, in un laboratorio, davanti a un computer o in qualunque altro posto: un passo alla volta, chissà dove mi porterà la Vita.
Se fosse stato per il solo studio, molto probabilmente, Tu non staresti leggendo questi ringraziamenti, perché, anche se sei un amico o amica dell'Università, ci siamo conosciuti tra una pausa e l'altra, condividendo appunti, frammenti di vita e viaggi in treno e in auto.
Se sei di Grestyle, o addirittura uno Stoico, sei stato l'ossigeno del fine settimana: insieme a te e

a questo gruppo pazzesco, sto scoprendo lati di me che non immaginavo.
Se condividi con me esperienze di Azione Cattolica, sei una persona che mi fa sentire a casa, accolta con un sorriso e tanto altro. Se mi stai accompagnando spiritualmente, grazie: mi hai permesso di dare voce a tanti pensieri e a vedere Dio nella mia Vita.
Se hai studiato "gentilmente" con me negli ultimi tempi, grazie per le sane e grasse risate, i Sette caffè e i cestelli alla frutta, ma anche per le condivisioni profonde che sono nate.
Se sei un amico "di vecchia data" e sei ancora qui, la cosa bella è che tu sia ancora qui.
Se ti mando dei video stupidi e sopporti le mie battute, grazie per la tua pazienza: vuol dire che il nostro rapporto ormai è consolidato.
Se sei parte della famiglia (anche acquisita e allargata), sei parte della mia storia a cui sono tanto grata.
Se mi hai accolto nella tua cucina, grazie per le cene, i pranzi e le prelibatezze che mi hai fatto trovare pronte in tavola.
Se sei un fratello o una sorella, un cognato o una cognata, mi hai fatto vivere molte emozioni con i grandi annunci e il fermento degli eventi degli ultimi anni: che figata!
Se sei una persona che mi vuole tanto bene e a cui io ne voglio tanto, mi stai aiutando a vedere la Vita e il mio corpo con occhi nuovi e, quotidianamente, sei capace di spronarmi e sorprendermi.
Se sei la mamma, sopporti le mie frequenti critiche e dici "tanto sbaglio sempre". In realtà, nelle cose importanti non hai mai sbagliato. Non ti sei mai imposta sulle nostre scelte, ci hai sempre permesso di sbagliare e ci hai lasciato crescere, osservando con umiltà, gioia e orgoglio i grandi passi che stiamo facendo. Se sei un Angelo che veglia sempre su di me, doni un tocco speciale alla mia Vita.
Vorrei benedire tutti voi, che festeggiate con me questo traguardo. Ho appurato che il tè verde ha numerosi effetti benefici, ma le belle persone ne hanno molti di più.